Landslides as geological hotspots of CO_2 to the atmosphere: clues from the instrumented Séchilienne landslide, Western European Alps.

Pierre Nevers[1], Julien Bouchez[2], Jérome Gaillardet[2, 4], Christophe Thomazo[3], Delphine Charpentier[1], Laeticia Faure[2] and Catherine Bertrand[1]

[1]UMR Chrono-Environnement 16 route de Gray, 25000 Besançon, France
[2]Université de Paris, Institut de physique du globe de Paris, CNRS, F-75005 Paris, France
[3]UMR CNRS/uB6282 Biogéosciences 6 Boulevard Gabriel, 21000 Dijon, France
[4]Institut Universitaire de France, 75231 Paris, France

Correspondence to: Pierre Nevers (*pierre.nevers@univ-fcomte.fr*)

Abstract. This study makes use of a highly instrumented active landslide observatory (9 years of data) in the French Alps, the Séchilienne slope. Here we use a combination of major element chemistry and isotopes ratios ($^{87}Sr/^{86}Sr$, $\delta^{34}S$) measured in different water types of the stable and unstable part of the Séchilienne instability to assess the contribution of the different lithologies of the slope and the chemical weathering mechanisms. Chemical and isotopic ratios appear useful to characterize weathering processes and the origin of waters and their flowpaths through the massif. A mixing model allows us to allocate the different major elements to different sources, to identify secondary carbonate formation as a major process affecting solutes in the subsurface waters of the instability, and to quantify the involvement sulfuric and carbonic acids as a source of protons. As a consequence of the model, we are able to show that the instability creates favorable and sustained conditions within the failure, through the opening of new fractures bringing fresh and reactive surfaces allowing for the production of sulfuric acid by pyrite oxidation. We clearly identify the contribution of each mineral phase dissolution in the chemistry of the waters. The contribution of remote gypsum dissolution to the sulfate budget in the waters is evidenced. We are also able to refine the pre-existing hydrogeological views on the local water circulation and water flow paths in the instability by showing the hydrological connectivity of the different zones. Overall, our results show that the Séchilienne landslide, despite its role in accelerating rock chemical and physical weathering, acts, at a geological time scale (i.e. at timescales longer that carbonate precipitation in the ocean) as a source of CO_2 to the atmosphere. If generalizable to other large landslide complexes in mountain ranges, this study illustrates the complex coupling between physical and chemical erosion and their impact on the carbon cycle and global climate. The study also highlights the importance of deciphering between sulfite oxidation and gypsum dissolution as a source of sulfate ions to rivers, particularly in mountain ranges.

1 Introduction

The weathering of rocks plays a key role in the chemical and climatic evolution of the Earth surface and is one of the geological processes that impacts atmospheric CO_2 concentration. When carbonic acid is the proton supplier, silicate weathering removes carbon dioxide from the atmosphere (Lerman et al., 2007, Berner and Berner, 2012). However, the oxidative dissolution of sulfides (*e.g.* pyrite FeS_2) produces sulfuric acid that can act as an alternative proton supplier to chemical weathering reactions. Although not directly influencing atmospheric CO_2, silicate weathering by sulfuric acid does reduce the potential of rock weathering for CO_2 sequestration by "removing" silicates from the Earth surface and thus limiting their weathering by carbonic acid. When sulfuric acid reacts with carbonate minerals, dissolved inorganic carbon is added to ambient waters which leads on the long term to CO_2 release towards the atmosphere (Lerman et al., 2007, Calmels et al., 2007, S.-L. Li et al., 2008, Torres et al., 2014). The relevance of this process for the global carbon cycle is two-fold. First, even though carbonate rocks do not constitute the major fraction of the rock types exposed at the Earth surface, the dissolved products of carbonate dissolution dominate global weathering fluxes (Gaillardet et al., 1999) as carbonate minerals dissolve several orders of magnitude faster than silicates (Lasaga 1984). Second, because weathering by sulfuric acid is limited by the supply of sulfide minerals to the Earth surface, it is particularly prominent in active mountain belts characterized by high erosion rates (Calmels et al., 2007; Torres et al., 2016; Blattmann et al., 2019). Within these tectonically active environments, landslides are likely to be hotspots of sulfuric acid production, carbonate weathering, and CO_2 release (Emberson et al., 2015, 2018). Indeed, slope instability leads to sustained grain comminution and fractures opening, thereby providing a continuous supply of contact surfaces between water, air, and minerals that can in particular allow for sulfuric acid production and carbonate mineral weathering (Binet et al., 2009; Bertrand et al., 2014).

Here we explore the hypothesis that slope instability can constitute a mechanism promoting coupled sulfide oxidation and carbonate weathering, in a contribution to the study of the role active mountain ranges play on the global carbon cycle (Raymo and Ruddiman 1992). We focus on the Séchilienne slope instability located in the French Alps. This site of active, slow landsliding serves as an observatory for landslide processes and has been the subject of previous hydrogeological and geophysical investigation (Vengeon, 1998; Guglielmi et al., 2002; Meric et al., 2005; LeRoux et al., 2011; Vallet et al., 2015; Lajaunie et al., 2019). The Séchilienne site offers the opportunity to study the role of erosion on sulfide oxidation and carbonate weathering under climatic conditions that differ from those of previous studies (such as Taiwan, the Himalayas, or the Andes), and thus to improve the knowledge on the global impact of landsliding on atmospheric CO_2 and climate. We combine measurements of the concentration of major elements and of the isotope composition of strontium and sulfur ($^{87}Sr/^{86}Sr$, $\delta^{34}S$) dissolved in groundwater and springs to estimate the contribution of different rock types to the dissolved species produced by weathering reactions in the landslide. In particular, we estimate the relative role of different acid types (carbonic *vs*. sulfuric) and of two rock types (silicates *vs*. carbonates), and evaluate the role played by secondary carbonate formation on the solute budget of percolating waters. Besides shedding light on the global impact of landsliding on atmospheric CO_2, Sr and S isotopes coupled to water chemistry allow for a quantitative analysis of the sources of solutes in natural waters and of the chemical

evolution of natural waters, which in turn opens the possibility to improve existing hydrogeological model in complex environments such as landslides.

2 Study area

2.1 Geological setting

The "Séchilienne" site hosts a highly-instrumented, continuously-monitored landslide, part of the French National Landslide Observatory (OMIV, http://www.ano-omiv.cnrs.fr/). The Séchilienne massif is located at the SW border of the Paleozoic crystalline Belledonne mountain range in the French Alps, 20 km southeast of Grenoble (Isère, France; Fig. 1). The active zone of the site is a gravitational instability affecting 60.10^6 m^3 of material, with a maximum depth of about 150 m, located on a south-facing slope of the massif (Le Roux et al. 2011). The most active part of the landslide, referred to as “les Ruines”, is located on the eastern border of the unstable zone. Long-term monitoring (extensometers, geodetic measurements, tacheometers and microwave radar) shows that the displacement velocity is around 300 cm y^{-1}, while the less active parts of the site are moving at a mean of 10 cm y^{-1} (Le Roux et al. 2011; Dubois et al. 2014).

Geological and structural information are provided by the geological map and by two boreholes drilled in 2010 in the unstable area at depths down to 150 m. Baudement et al. (2013) has integrated these information in a GOCAD® 3D model, recently used by Lajaunie et al. (2019) to propose a new vision of the Séchilienne slope based on a 3D resistivity model. The basement of the massif is mainly composed of micaschists showing a N-S trending sub-vertical foliation. Stratigraphically discordant deposits dating from the Carboniferous to the Liassic periods cover the micaschists on the top north – northeast of the massif (Mont Sec) and along the Sabot Fault (Fig. 1). The slope is locally covered by Quaternary (Würm) glacio-fluvial deposits made of material reworked from the surrounding formations (Vengeon 1998, Vallet 2014). The micaschists consist primarily of quartz, biotite, phengite, and chlorite with occurrence of carbonate veins and pyrite in fractures. Carboniferous deposits are made of black shales, sandstones, and conglomerates with quartz and serpentine pebbles. Triassic rocks correspond to sandstone, quartzite, dolomite and locally of black shales, argilites, and gypsum. Liassic deposits are limestones with intercalation of layers rich in breccia consisting of micaschist, dolomite, and coal (Barféty et al. 1972, Vengeon 1998, Vallet 2014). Strong local heterogeneities exist in terms of lithology and fracturation and are induced by the gravitational deformation (Lajaunie et al. 2019).

The part of the slope affected by the landslide extends from 400 m to 1100 m above sea level (a.s.l.; Le Roux et al. 2011; Fig. 1d). Above the elevation of 1100 m a.s.l. the morphology of the Mont Sec corresponds to a plateau of glacial origin underlain by moraine deposits concentrated in small topographic depressions. The landslide is delimited at its northern border by a major head scarp of about 10 meters high and several hundreds of meters wide, which separates the glacial plateau of Mont Sec from the unstable zone. Eastward, N-S faults scarps limit the landslide whereas the western and southern parts are not well defined by geomorphological evidences. The motion of the landslide consists in a deeply-rooted, toppling movement with N50-70 slabs toward the valley, coupled with the sagging of the upper zone of the slope near the Mont Sec (Vengeon 1998). The

Séchilienne instability is assumed to originate from the decompression of the basement rocks after the Romanche glacier retreated at the last glaciation (15 kyr ago). Decompression caused the opening of fractures and then the collapse of the summit of the Mont Sec (Montjuvent and Winistorfer 1980, Vengeon et al. 1999, Potherat and Alfonsi, 2001,). The Séchilienne slope is thus affected by a dense network of near-vertical, open fractures trending N70 and N110/120, controlling the deformation of the Séchilienne landslide which is characterized by a deep progressive deformation (about 100-150 m) and the absence of a well-defined basal sliding surface. Two N20 major fractures are also crossing the Séchilienne massif, the Sabot and the Séchilienne faults. Open fractures are locally filled with detrital material resulting from the erosion of the massif (Vallet et al. 2015a).

Borehole logs available within the instability (Lajaunie et al. 2019) show that the rock formations below the slope are relatively unstructured, and that pyrite is heterogeneously distributed therein. Rock samples along the boreholes seem to have been subjected to oxidizing conditions, albeit with no clear sulfide reaction front at the scale of the instability. In addition, petrological observations on thin sections from these boreholes, combined with mineralogical analyses obtained from X-ray diffraction (XRD; Supplementary Material) show that pyrite is disseminated within the rocks, with no particular association with calcite. Gypsum was not detected from XRD analyses in the sampled rocks, consistent with results from inverse modeling by Vallet et al. (2015) suggesting that sulphates in waters from the unstable zone (UZ) originate essentially from pyrite oxidative weathering.

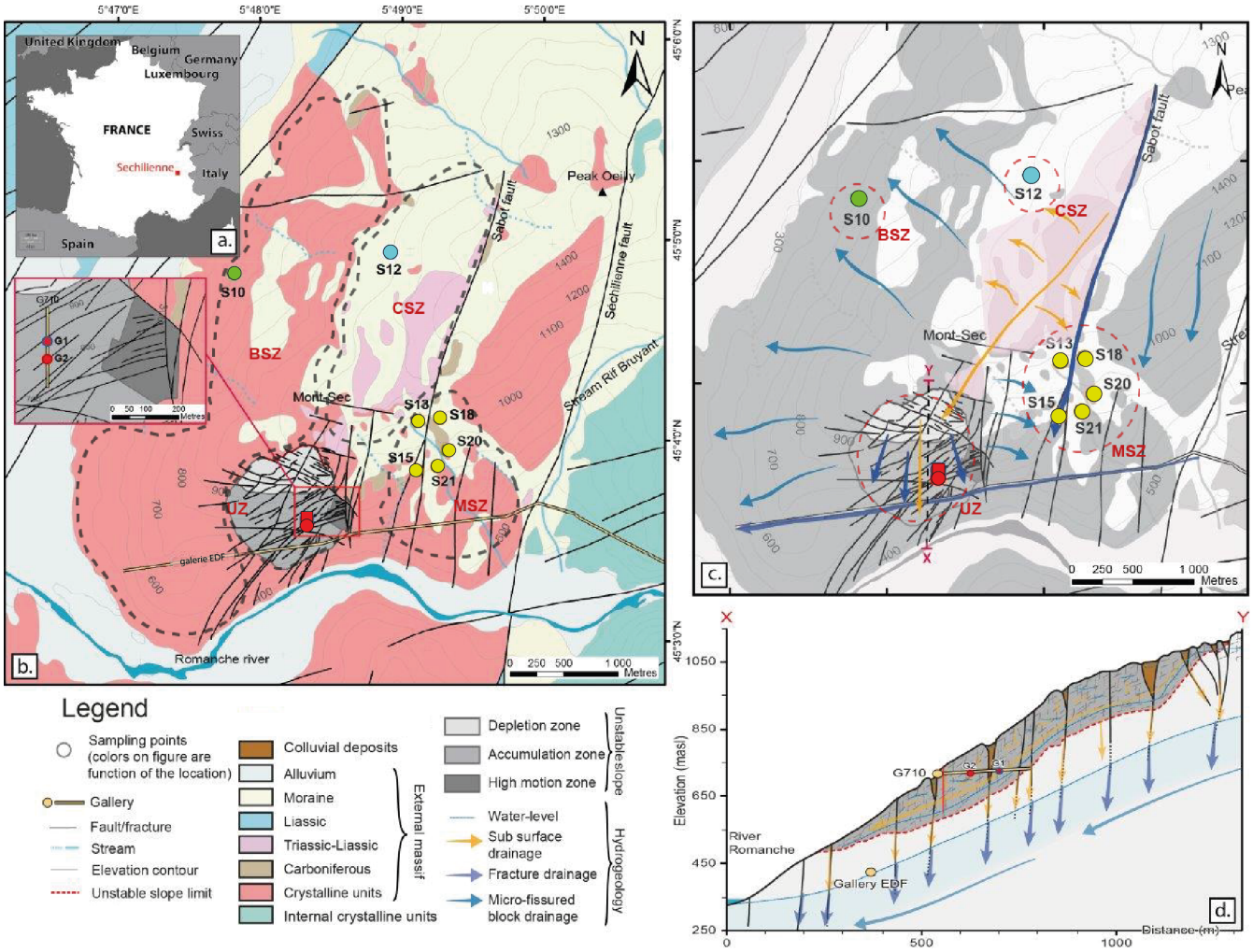

Figure 1: Map of the Séchilienne site a. Location of the Séchilienne massif in the French Alps, b. Simplified geological map of the Séchilienne massif and sampling locations, c. schematic hydrogeological model of the Séchilienne massif, d. hydrogeological cross-section of the instability, modified after Vallet et al. (2015).

2.2 Hydrogeological setting

The high degree of fracturation and heterogeneity of the Séchilienne massif leads to distinct and complex patterns of hydrological flow paths. At Séchilienne, water pathways are characterized by different transit times related to a dual permeability behavior that is typical of fractured rock aquifers where conductive fractures play a major role in the drainage (Fig 1.c): rapid transit of infiltration waters through fractures reflects the functioning of a so-called "reactive" hydrological component, whereas slower transit of water through the micro-fissured, less permeable rock matrix, resulting in a smeared response of flow rate to rainfall typifies an "inertial" circulation (Maréchal 1998, Cappa et al. 2004, Vallet et al. 2015a). In

particular, the Sabot and Séchilienne faults play an important role on fluid flow through the massif by draining waters from the sedimentary cover at a fast rate (0.7 km day^{-1}), and bypassing the less pervious and more inertial micro-fissured matrix characterized by lower flow velocity (0.08 km day^{-1}) (Mudry et Etievant 2007; Vallet et al. 2015a). Local perched aquifers develop during high-flow periods and discharge downwards to the main aquifer, due to the contrast of permeability between the decompressed zone at the surface and the unaltered rock (Lajaunie et al., 2019). An underground tunnel for the production of electricity in a local hydropower plant, named "Galerie EDF", built by Electricité de France (EDF) and located at the base of the slope, acts as a major westward drain for groundwater (Vallet et al. 2015a).

Difference in hydraulic conductivity between the highly fractured unstable zone (thickness about 150-200 m, Le Roux et al. 2011) and the basement situated under the landslide (Fig 1.d) led to the build-up of a two-layer aquifer system. Those two layers are connected to one another through major fractures (Vengeon 1998, Meric et al. 2005; Le Roux et al. 2011, Guglielmi et al. 2002, Vallet et al. 2015a). A temporary and discontinuous shallow perched aquifer is present in the landslide with extension and connectivity varying according to short-term recharge variations. This aquifer is almost dry during the low flow periods, with numerous disconnected saturated pockets (such as open fractures filled by colluvial deposit and altered material) linked to the heterogeneity of the landslide (Guglielmi 2002, Cappa et al. 2004, Vallet et al. 2015a). The recharge of this aquifer is mainly local (through trenches and counterscarps, limiting the runoff) with a contribution of remote groundwater through near-surface drainage at high-flow periods from the sedimentary cover above the landslide (near the Mont Sec summit) (Guglielmi 2002, Vallet et al. 2015a). The deep aquifer, which extends all over the massif (altitude around 550 m asl), corresponds to a saturated layer hosted by the fractured metamorphic bedrock and to an overlying, 100-m thick vadose layer (Vallet et al. 2015a). The deep aquifer level is controlled by the constant water heads of the Romanche alluvium in the valley, and of the Galerie EDF (425 m a.s.l.).

3. Samples and analytical methods

Nine outflows draining the whole massif were investigated for physico-chemical parameters and dissolved load chemistry (Fig 1.a). Two of these outflows (G1 and G2) are located within the Unstable Zone (UZ) and correspond to seep water collected in a tunnel excavated to monitor the landslide at 710 m a.s.l. (G710). The remaining outflows (S10, S12, S13, S15, S18, S20, S21) correspond to springs draining the Stable Zone (Fig 1.a). These outflows can be differentiated regarding the dominant local lithology: S10 is located in the Bedrock Stable Zone (BSZ), S12 in the Carbonate Stable Zone (CSZ), and S13, S15, S18, S20, and S21 are located in an area of the Stable Zone characterized by mixed lithology (Mixed Stable Zone, MSZ). Samples were collected every three months over the period 2010-2019. Between 2014 and 2017, waters were sampled once a year for Sr isotopes, while samples for S isotope were collected in 2019. In total, 360 water samples were collected and analyzed for this study. Four local rocks samples were taken, reflecting the main lithological types encountered at Séchilienne: basement micaschist, carbonate (both calcite-rich and dolomite-rich) from the sedimentary cover, and a recrystallized vein in micaschist.

Field measurements of water temperature, pH, and electrical conductivity (EC) were made with a WTW pH/Cond 340i (Xylem Inc.) sensor, with a precision of 0.1 unit and 0.1 µS cm^{-1} for pH and EC, respectively. Water samples were collected in polyethylene bottles and filtered with a 0.45 µm pore diameter nylon filter, before being preserved in cold conditions for measurements of major element concentration and Sr and S isotopes. Analyses of dissolved major elements were all carried out at the research laboratory Chrono-Environnement at the University of Franche-Comté. Dissolved major cation concentrations were measured by atomic absorption spectrometry (AA 100 Perkin-Elmer) with detection limits of 0.5, 0.1, 0.01, and 0.1 mg L^{-1} for Ca^{2+}, Mg^{2+}, Na^{+} and K^{+}, respectively. Dissolved anion concentrations were determined using high-pressure ion chromatography (Dionex DX 100) with detection limits of 0.1, 0.1, and 0.05 mg L^{-1} for Cl^{-}, SO_4^{2-} and NO_3^{-}, respectively. The concentration of HCO_3^{-} was measured by acid titration (N/50 H_2SO_4) within 48 hours after sampling, with 1% accuracy. Dissolved silica concentration was analyzed with a spectrophotometer (Spectroquant, Pharo 300, Merck) using a silica-test kit (Merck) with 3% accuracy. Only analyses with a charge balance better than 10% were taken into account.

Strontium isotope analyses were carried out at the High-Resolution Analytical Platform (PARI) of the Institut de Physique du Globe de Paris (IPGP). For water samples, dissolved Sr was first isolated from the water sample matrix by automated ion chromatography following the method of Meynadier et al. (2006). For rocks, in addition to bulk samples analysis after digestion in concentrated HF and HNO_3. a three-step sequential leaches were conducted using H_2O, 1M acetic acid, and 1M HCl. The first step is designed to recover the exchangeable fraction adsorbed onto the solid surface; step 2 was for extracting Sr from carbonates, amorphous hydroxides, and phosphate minerals (Tessier et al., 1979); step 3 was to dissolve any high-order Fe–Mn oxide/oxyhydroxide phases that might be present after HCl leaching (Tessier et al., 1979). The leachate solutions and residual samples were measured for major and trace elements by Quadrupole ICP-MS (Agilent 7900) with a precision better than 5% and processed for $^{87}Sr/^{86}Sr$ ratio analysis following the same procedure used for bulk samples. To that effect, 3M HNO_3 aliquots of digestion solutions were loaded on columns loaded with 0.2 mL of Sr-SPEC resin (Eichrom). Then, 3M HNO_3 was used to elute the sample matrix before Sr was eluted in H_2O. Strontium isotope ratios were then measured using a Multi-Collector Inductively Coupled Plasma Mass Spectrometer (MC-ICP-MS; Thermo-Fisher Neptune) in low resolution mode (Hajj et al., 2017). Purified Sr solutions were introduced using an APEX desolvation unit and a PFA nebulizer at a rate of 50 to 100 µL min^{-1} depending on the measurement session, and at Sr concentrations between 50 and 150 ppb. The accuracy and reproducibility of the $^{87}Sr/^{86}Sr$ analysis was assessed using repeated measurements of the international isotope Sr carbonate standard (SRM987, NIST). The obtained values for SRM987 standard NIST was 0.710249 ± 0.000025.

Sulfur isotopes measurements were performed at the Biogéosciences Laboratory, University of Bourgogne, Dijon, France on both sulfates from water samples (Table A1) and sulfides from basement micaschist (Table B2). Nine samples were treated with an excess of 250 g l^{-1} $BaCl_2$ solution to precipitate $BaSO_4$. After centrifugation, the $BaSO_4$ precipitate was washed several times with deionized distilled water and dried at 60°C for 24 hours in an oven. Five hundred micrograms of purified barite samples were poured into tin capsules and homogeneously mixed with 1/3 of vanadium pentoxide before isotopic measurements (^{34}S, ^{32}S) using a Vario PYRO cube (Elementar GmbH) connected online *via* an open-split device to an IsoPrime IRMS system (Isoprime, Manchester, UK). Sulfur isotope data are expressed in delta notation and reported in units per mille

(‰). The $\delta^{34}S$ data are reported with respect to the international standard Vienna Cañon Diablo Troilite (VCDT). Analytical errors are ±0.3‰ (1σ) based on replicate analyses of the international barite standard NBS-127, which was used for data correction assuming a $\delta^{34}S$ value of +20.3 on the VCDT scale

Sulfur contained in sulfides was extracted from eight rock samples of the basement micaschist formation on aliquots of 3 grams (4 sub-samples on each of two rock samples, including unaltered pyrite and iron oxides; Table B2) following the method described by Canfield et al. (1986). Dried and rinsed Ag_2S precipitates recovered after wet chemistry sulfides extraction are weighted for gravimetric quantification of sample sulfur content. Five hundred micrograms of silver sulfides precipitates were then mixed with an equivalent weight of tungsten trioxide in tin capsules before combustion in a Vario pyro cube (Elementar GmbH™). Sulfur isotope compositions ($\delta^{34}S$) were measured using an IsoPrime IRMS device (Isoprime, Manchester, UK). International standards (IAEA-S-1, IAEA-S-2, IAEA-S-3) were used for calibration and results are reported in the δ-notation relative to the Vienna Canyon Diablo Troilite (VCDT) standard. Reproducibility (1σ) is better than 0.2‰ based on duplicate analyses of standard materials and samples.

4. Results

The concentration of major and trace elements, as well as Sr and S isotope composition are given in Table A1 and A2. The concentration of major elements, EC, pH, temperature, and Sr and S isotope composition of water samples are given in Table B1.

4.1 Major elements

Rock samples

The two limestone samples show distinctive response to the leaching procedure, with most of the Ca of the "Laffrey" limestone located in the acetic acid leachate (67%) and the rest in the HCl fraction (11%), which is indicative of the calcitic nature of this rock sample (Table A1). By contrast, most of the Ca of the "Lias" sample is hosted in the residue, while a significant fraction (37%) is HCl-soluble, suggesting that the sample is dolomitic. The "micaschist" and "vein" samples have higher bulk Sr/Ca, Mg/Ca, Al/Ca and Na/Ca ratios than the two limestone samples, confirming that they are mostly made of silicate minerals.

Spring water samples

The chemical composition of waters sampled on the Séchilienne site is very diverse, reflecting heterogeneity in rock types and the existence of various groundwater flow paths. Water pH at Séchilienne is relatively high and varies from 6.5 to 9.4 with a mean value of 7.9. Electrical conductivity range between 79 µS cm^{-1} and 1114 µS cm^{-1} (Table B1). From the major ion perspective, samples can be grouped into 4 main water types (Fig. 2). These water types correspond to those identified

previously by Vallet et al. (2015a). Type 1 corresponds to Ca-HCO_3 waters, typical of water draining carbonate formations, typified by the S12 spring draining the carbonate cover at the top of the Séchilienne slope (CSZ). S12 has low EC values ranging from 79 µS cm^{-1} to 147 µS cm^{-1} with a mean of 117 µS cm^{-1}. The second group corresponds to Mg-Ca-HCO_3 rich waters, which have circulated through the sedimentary cover (carbonate and dolomite) and the micaschists bedrock and is represented by the S10 spring (BSZ). All S10 samples have higher electrical conductivities ranging from to 308 µS cm^{-1} to 509 µS cm^{-1} with a mean of 443 µS cm^{-1}. Waters sampled in the unstable part of the slope (UZ), include the underground outflows G1 and G2 and show a chemical composition that vary from Mg-Ca-HCO_3-SO_4 waters to Mg-Ca-SO_4 waters and constitute the third hydrogeochemical group. The highest EC values of this study are observed for the G1 outflow with electrical resistivities ranging from 613 µS cm^{-1} to 1114 µS cm^{-1} with a mean value of 824 µS cm^{-1}. The other outflow of the unstable zone (outflow G2), in contrast to the previous one, shows a mean electrical conductivity value around 391 µS cm^{-1}, with a minimum value of 313 µS cm^{-1} (and a maximum value of 470 µS cm^{-1}). The fourth and last type of waters include the S13, S15, S18, S20, S21 outflows, sampled in the stable part of the slope (MSZ) along the Sabot fault, and show Ca-Mg-HCO_3-SO_4 type waters. The MSZ group exhibits EC values ranging from 357 µS cm^{-1} to 567 µS cm^{-1}, with a mean of 479 µS cm^{-1}. Waters of the Unstable Zone group (G1,G2) are characterized by the highest concentrations in SO_4^{2-} (from 1.32 to 3.90 mmol L^{-1}) compared to the other outflows sampled which have values ranging from 0.57 to 1.34 mmol L^{-1} for the MSZ outflows (S13, S15, S18, S20, S21) and from 0.48 to 0.67 for the S10 (BSZ) outflow (Fig. 2; Tab. B1). Fig. 2 clearly shows that SO_4^{2-} ions are significantly contributing to the electrical balance of the analyzed waters. Dissolved Cl^- concentrations are lower than 50 µmol L^{-1} in springs S10, S12, S13, S18, but can reach values above 100 µmol L^{-1} in springs S15, S20, and S21. Dissolved NO_3^- concentrations are typically below 20 µmol L-1 in springs G1, G2, and S10, but are higher in springs S12, S13, S18, S15, S20, and S21, with concentrations above 100 µmol L^{-1} observed in the latter (Tab. B1).

Rainwater samples (Tab. B1) show very low EC values with a mean of 26 µS cm^{-1} and low concentrations for all elements analyzed. In particular, chloride concentrations range from 3.3 µmol L^{-1} to 20.3 µmol L^{-1}.

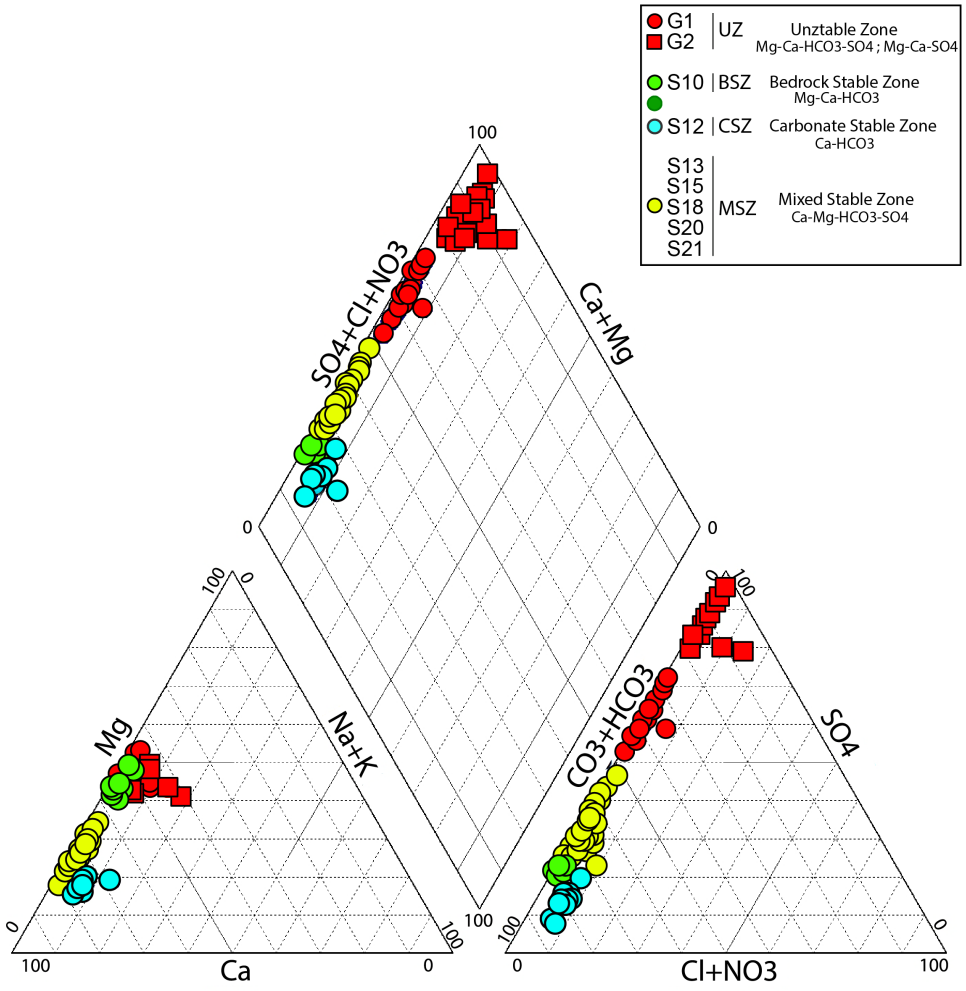

245 Figure 2: Piper diagram representing the major water types samples in the outflows of the Séchilienne massif

4.2 Strontium isotopes

Rock samples

The two carbonate rock samples have the lowest Sr isotopic ratios (Table A1), with the lowest value being 0.7095 slightly
250 higher than the Sr isotopic composition of lower Jurassic seawater (from 0.7065 to 0.7076; Koepnick et al., 1990). The acetic-acid and HCl^- soluble fractions of the limestone samples, as well as the bulk analysis of the dolomitic "Lias" sample and its H_2O leachate, are characterized $^{87}Sr/^{86}Sr$ ratios of ~ 0.7105. The $^{87}Sr/^{86}Sr$ ratio of all the leachates of the calcitic "Laffrey" sample, as well as of the bulk sample, show a wider range of variation, in the range 0.7104-0.7179. By contrast, the highest

$^{87}Sr/^{86}Sr$ ratios were found in the micaschists samples with a value of 0.7351 (Table A1), typical of silicate rocks (0.73±0.01; Négrel et al., 1993). The veins contained in the micaschists also show high Sr isotopic ratios (0.7277). Such high $^{87}Sr/^{86}Sr$ ratios are particularly encountered in the residues and bulk samples.

Spring water samples

The Sr isotope ratios measured in the spring samples in and around the Séchilienne instability range from 0.7093 to 0.7231 (Table B1). The four main groups of waters have contrasted $^{87}Sr/^{86}Sr$ isotopic ratios. The highest $^{87}Sr/^{86}Sr$ values are found in the UZ underground outflows samples (G1, G2) with an average of 0.7210 ± 0.0006 (one standard deviation). The lowest $^{87}Sr/^{86}Sr$ values correspond to the waters of the MSZ (springs S13, S15, S18, S20, and S21), and average at 0.7095 ± 0.00012, *i.e.* at the value measured in the carbonate rock. The S12 outflow (CSZ) is characterized by $^{87}Sr/^{86}Sr$ ratios of around 0.7095 ± 0.00005, *i.e.* close to those of the MSZ group. Intermediate values of Sr isotopic ratios are found for the samples of the BSZ group (S10), with an average of 0.7148 ± 0.00019.

4.3 Sulfur isotopes

Rock samples

Sulfur isotope composition of unaltered rock samples range from -7.9‰ to 17.8‰ with an average value of 1.23‰ ± 11.82‰, whereas weathered micaschists exhibit $\delta^{34}S$ values ranging from -13.1 to 9.9‰ and an average of -1.42‰ ± 9.55‰; Table A2). These numbers show the extremely large range of possible sulfur isotope signals co-existing in the various rock types present in the landslide.

Spring water samples

Waters show a much narrower range of $\delta^{34}S$ values, ranging from -5.5‰ to 6.5‰ (mean 0.43‰ ± 5.12‰). The highest $\delta^{34}S$ values are observed for water of the MSZ group (outflows S13, S15, S20, S21) with an average of 6.28‰ ± 0.34‰. Samples of the S12 outflow (CZS group) also exhibits a high $\delta^{34}S$ value of 6.03‰. The G1 and G2 outflows (UZ group) exhibit negative $\delta^{34}S$ values with an average of -3.74 ‰ ± 1.75‰), with lower $\delta^{34}S$ values for G2, (averaging at -5.33‰ ± 0.22‰) than for G1 (2.2‰ ± 0.06‰). The BSZ group (outflow S10) is characterized by $\delta^{34}S$ values that are intermediate between those of the MSZ and UZ groups (2.4‰).

5. Discussion

5.1 Identification of sources to dissolved species

5.1.1 Atmospheric and anthropogenic sources

Rainwater is potentially a significant source of elements to the water sampled in the different springs at Séchilienne. To assess the importance of atmospheric inputs, we use Cl^- concentrations. Chloride is not significantly involved in chemical reactions at the Earth surface and its presence in waters has three main origins: rainwater (through the dissolution of seasalt aerosols), dissolution of saline rocks or inclusions, and anthropogenic inputs. On the other hand, at Séchilienne, NO_3^- is most likely to be derived from human activity, through fertilizer input and/or domestic waste. Therefore, the correlation between Cl^- and NO_3^- concentrations in springs S15, S20, and S21 ($R^2 = 0.65$; Fig. C1) suggests that beyond rainwater, anthropogenic inputs are a significant Cl^- source to these springs. This inference is consistent with the presence of villages upslope from these springs. High Cl^- concentrations (> 100 µmol L^{-1}) are also found in some samples from underground outflows G1 and G2 (Table B1). However, in the case of these two springs such high Cl^- concentrations are not accompanied with high NO_3^- concentrations but correlate to some extent with dissolved Na^+ and K^+ concentrations (Fig. C1). This observation could be indicative of the dissolution of salts (NaCl and KCl) as a significant process delivering Cl^- and cations to the springs. Although the origin of these salts is unclear, we note that Zn-Pb ore deposits are reported discovered in the bedrock of Séchilienne landslide exploitation (Barnes, 1997). The presence of fluid inclusions containing alkali elements and Cl in such ores is likely, and leaching of such fluid inclusions could have occurred because of the exposure of new mineral surface during ore. To summarize, the excess of Cl in Séchilienne springs is most probably due to a combination of human activity (road salts and agriculture) and to dissolution of fluid inclusions of hydrothermal origin.

The expected concentration of Cl^- derived from precipitation in spring waters (hereafter called $[Cl]_{crit}$ for "critical chloride", Stallard et al., 1983) of the Séchilienne massif can be estimated by multiplying the mean Cl^- concentration found in rainwater by the mean evapotranspiration factor (P/ETP: 4.02 with P: precipitation, ETP: evapotranspiration calculated from temperature and latitude of the study site, according to Oudin et al. 2005). Alternatively, $[Cl]_{crit}$ can be estimated as being equal to the lowest Cl^- concentrations in the sample set (S10, S12 and S21 springs). Both methods concur to fix the atmospheric contribution of Cl^- to the Séchilienne waters at a maximum of 30 µmol l^{-1}. Above this concentration, additional sources must be involved. Once $[Cl]_{crit}$ is known, it is possible to correct all cation concentrations from the atmospheric seasalt input by using:

$$[X]^* = [X] - [Cl]_{crit} \times \left(\frac{X}{Cl}\right)_{seawater} \quad (1)$$

In this equation, [*X*]* denotes the concentration of an element X in the water sample, corrected from the atmospheric input, and $(X/Cl)_{seawater}$ is the seawater elemental ratio. This correction is only significant for Na^+, due to the relatively high concentrations found in the Séchilienne waters.

As explained above, significant excess of Cl^- ($[Cl] > [Cl]_{crit}$) is found for the S15, S20, and S21 springs where this excess is the highest (about 30 to 60 µmol l^{-1}) and due to domestic and/or agricultural activity; and in the G1 and G2 underground outflows (between 15-20 µmol l^{-1} of excess), where this excess can be attributed to salt dissolution. For the first group of springs, it is most likely that input of Cl^- is associated with input of K^+, through the use of fertilizers. For the second group of springs each mole of Cl^- released by salt dissolution can be associated with one mole of K^+ or one mole of Na^+. Because of the challenge associated to assessing the exact cause for the observed Cl^- excess in these springs, in the quantitative source apportionment (section 5.1.4) we use a stochastic approach to reflect the uncertainty linked to the nature of the cations delivered to the springs by these Cl^- sources. However, we emphasize that for the springs where silicate weathering is the most prominent process in terms of cation production (G1 and G2; see section 5.1.2 below), the correction for the solute sources causing the Cl^- excess (human activity and salt dissolution) is relatively negligible.

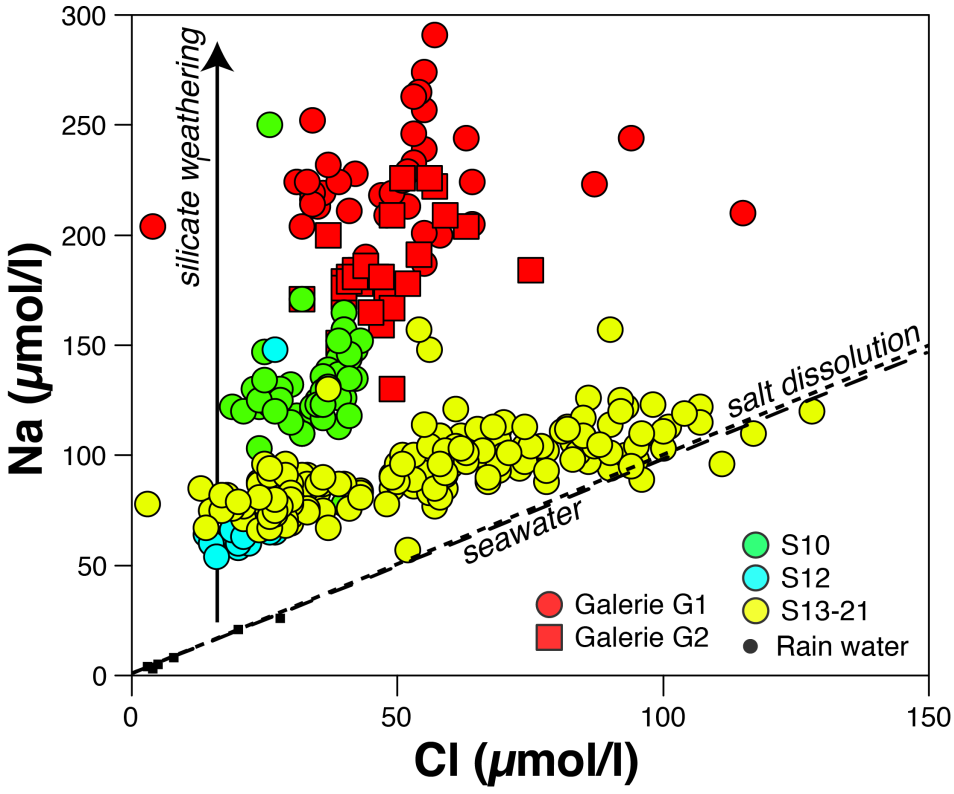

Figure 3: Na vs Cl concentrations measured in the different groups of water outflow from the Séchilienne massif. Rainwater data points are aligned along the seawater composition (seasalts). Na* is defined as the difference Na-Cl_{crit} were Cl_{crit} = 30 µmol/l (see text) where Cl_{crit} is the concentration of chloride only derived from rainwater and concentrated by evapotranspiration.

5.1.2 The importance of silicate weathering

The concentration of Na^+, once corrected from atmospheric and anthropogenic inputs, can be used as a proxy of silicate weathering reactions, if the dissolution of silicate minerals is a dominant source of Na to surface waters compared to salt dissolution and human activity. The underground outflows G1 and G2 have the highest Na* concentrations (mean values 200±30 µmol L^{-1} and 158±21 µmol L^{-1} for G1 and G2, respectively) (Fig. 3). This observation suggests the importance of silicate weathering reactions in the Unstable Zone, made of fractured micaschists. Although as explained above the source of excess chloride could also be contributing Na (were this additional source NaCl inclusions), the Na* concentrations remain the highest found in the Séchilienne landslide area assuming that all Cl^- release to waters is associated to an equivalent Na^+ release (in moles). Despite their excess of Cl^-, the MSZ outflows chemistry also reveals that silicate weathering reactions are releasing Na^+ to those waters (Fig. 3). However, the Na* concentrations of the Mixed Stable Zone (60 µmol L^{-1} on average) are equal to around half of those encountered in the Unstable Zone. This contrast between the stable (MSZ) and unstable zone (UZ) illustrates that the importance of silicate weathering is linked to the fracturation degree at Séchilienne. Finally, the low Na* concentration in the S12 outflow (Fig. 3) can be attributed to the fact that it mainly drains the carbonate cover. The most plausible explanation for the non-zero Na* concentration in S12 is the release of Na from silicate material disseminated in the carbonate rocks.

5.1.3 Identifying sources to solutes in the springs of the Séchilienne massif

In the following we use dissolved elemental and isotopic ratios to quantitatively constrain the contribution of various rock sources (silicates, carbonates, and gypsum) for solutes in the Séchilienne springs. As shown above, strong contrasts exist in $^{87}Sr/^{86}Sr$ ratios between the sedimentary carbonate cover and the crystalline rocks of the basement. The isotopic ratio of dissolved Sr released by water-rock interaction reflects that of the minerals undergoing dissolution and is not affected by the reincorporation of Sr in secondary minerals (*e.g.* Negrel et al. 1993). Sr isotopes can thus be used to trace the provenance of dissolved Sr, and by extension of the different cations, in the waters of Séchilienne. By contrast, elemental ratios such as Ca/Sr and Mg/Sr may be affected by the precipitation of secondary minerals and in particular by the formation of secondary carbonates (Bickle et al., 2015) and should be used more carefully to identify the provenance of cations.

A series of plots using $^{87}Sr/^{86}Sr$ as a common Y-axis are shown in Fig. 4. In $^{87}Sr/^{86}Sr$ *vs*. Ca/Sr or Na/Sr plots (Fig. 4a and 4b) conservative mixing between reservoirs is indicated by straight lines joining the end members. In this preliminary analysis, the Ca/Sr ratios for the carbonate, silicate, and evaporite end members are taken from Négrel et al. (1993) and Gaillardet et al. (1997). The corresponding Sr isotopic ratios are those measured in the rock samples from the Séchilienne massif (Table B1). The position of the data points corresponding to springs S13, S15, S18, S20, S21 (MSZ group) in Fig. 4a and 4b shows that their relatively low Sr isotopic composition cannot only be derived from the dissolution of carbonates. Another unradiogenic end member with low Ca/Sr and Na/Sr ratios needs to be invoked. As indicated by Fig. 4c this end member is enriched in sulfate as shown by its high SO_4/Na ratio. Although gypsum outcrops are not visible at Séchilienne, gypsum is known to exist

in the local Triassic formations present in the upper part of the slope as indicated by the regional geological map (Fig.1). More generally, the presence of gypsum is well documented in the Triassic strata of the the "external Alps" where it plays a major role in large-scale deformation and thrusting (Barféty et al. 1972). The occurrence of gypsum and carbonate dissolution inferred from the chemistry of the Séchilienne springs indicates that the Sabot Fault, which lies at the North-East of the MSZ outflows (Barféty et al. 1972), plays a major role in draining aquifers hosted by sedimentary rocks to the MSZ and BSZ outflows. The Sr and S isotope composition of Triassic seawater (between 0.7075 and 0.708 and 15±3 ‰, respectively; Burke et al. 1982, Fanlo and Aroya 1998, Kampschutte and Strauss 2004) and the typical Ca/Sr ratio of waters draining gypsum (Gaillardet et al., 1997; Meybeck et al., 1986) are entirely consistent with the contribution of gypsum dissolution. Fig. 4 also shows first that the S12 spring, reported by Vallet et al. (2015a) to be supplied by rapid flowpaths through the sedimentary cover, in addition to being solute-poor compared to springs of the MSZ group, is not influenced by gypsum dissolution despite its geographical position on the sedimentary part of the slope. The relatively high Na/Sr ratios observed in the S12 spring is probably due to anthropogenic influence, as revealed by the high nitrate concentrations measured in this spring (section 5.1.1 and Fig. C1c). By contrast, $^{87}Sr/^{86}Sr$ and chemical ratios of waters from the UZ outflows (G1, G2) are clearly influenced by a silicate end member. However, their Sr isotopic signature is lower than those of the local micaschist, indicating the additional contribution of Sr from a carbonate and / or evaporitic source to the G1 and G2 spring (Fig. 4a). The $^{87}Sr/^{86}Sr$ ratios of waters of the S10 outflow also exhibit intermediate values between the silicate and carbonate-gypsum mixing line, but with $^{87}Sr/^{86}Sr$ ratio lower than those of the UZ outflows, supporting the idea that water-silicate interaction in the BSZ were less intense than in the UZ. These inferences based on Sr isotopes are in full agreement with those made above based on Na* concentrations and can be interpreted as reflecting the lesser degree of fracturation of the stable zone compared to the unstable zone. Fig. 4c and Fig. 4d show that the higher $^{87}Sr/^{86}Sr$ ratios observed in springs of the UZ (G1, G2), and to a lesser extent of the BSZ (S10) are associated with sulfate enrichment. However, unlike for samples of the MSZ (S13-S21), dissolved sulfate in UZ and BSZ samples has a relatively low S isotope composition (Fig. 4d). This observation is compatible with a significant influence of sulfide oxidation, despite the very wide range of $\delta^{34}S$ values measured in the bedrock micaschists (between -13,14‰ and 17,77‰, average -0,10‰, S.D: 10,05; Table B2). The presence of pyrite has been reported in the unstable zone of Séchilienne (Bertrand et al. 2014, Vallet et al. 2015a). The concomitant increase in SO_4^{2-} and radiogenic Sr (Fig. 4c), combined with the decrease in $\delta^{34}S$ (Fig. 4d) suggests a coupling in the unstable zone between sulfide oxidation and silicate weathering. Indeed, the oxidative weathering of pyrite, possibly by O_2 or water, leads to the release of sulfate to waters (e.g. Spence and Telmer, 2005):

$$2FeS_2 + \frac{15}{2}O_2 + 7H_2O \rightarrow 2Fe(OH)_3 + 4H_2SO_4 \quad (2)$$

$$FeS_2 + 14Fe^{3+} + 8H_2O \rightarrow 15Fe^{2+} + 2SO_4^{2-} + 16H^+ \quad (3)$$

The oxidation of sulfide to intermediate sulfur species or to sulfate appears to produce only small isotope effects (Fry et al., 1986, 1988; Zerkle et al., 2009; Balci et al., 2012). The significance of these reactions in the unstable zone of Séchilienne can be related to the role of fracturation and grain comminution in favoring the contact between water, air, and minerals, which is the rate-limiting factor for a fast chemical reaction such as pyrite oxidation.

Altogether, our analyses shows that the composition of the water outflows from the Séchilienne site can be interpreted by a variable contribution of waters having interacted with micaschists and sedimentary rocks, and by a dual origin (sulfide oxidation and gypsum dissolution) of sulfate ions. The chemical and isotopic characteristics of the MSZ and UZ waters show that they have percolated through the sedimentary cover before reaching their outlet in the massif through the Sabot fault.

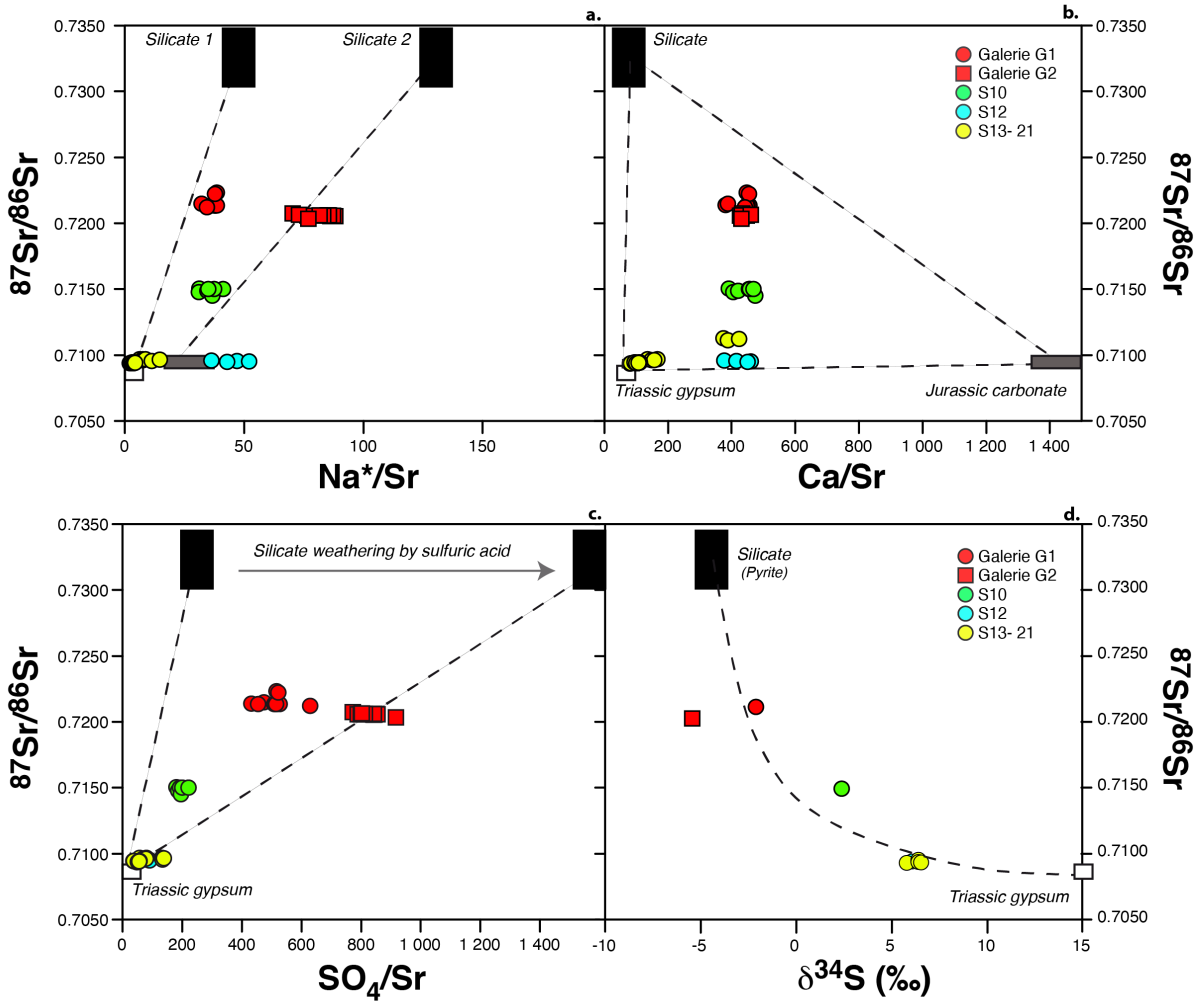

Figure 4: Sr isotopic composition of the different groups of water outflows from the Séchilienne massif as a function of Sr-normalized ratios (a, b and c) and S isotopic composition (d). Mixing end members are discussed in the text (Table C1). Straight lines indicate a mixing process

in Fig. 4a, 4b and 4c. In Fig. 4c, the dashed line is a mixing hyperbola calculated based on the composition of the end members ($^{87}Sr/^{86}Sr$, $\delta^{34}S$, and SO_4/Sr ratios of the silicate and carbonate end members).

5.1.4 Quantitative apportionment

Spring dissolved Sr isotopes and major element chemistry make it possible to estimate the relative contribution of each identified end member to the different cations. The details of these calculations are given in Appendix D. Following the above discussion, mixing equations can be written for the conservative trace element Sr:

$$\left(\frac{^{87}Sr}{^{86}Sr}\right)_{mix} = X_{sil}^{Sr}.\left(\frac{^{87}Sr}{^{86}Sr}\right)_{sil} + X_{carb}^{Sr}.\left(\frac{^{87}Sr}{^{86}Sr}\right)_{carb} + X_{gyps}^{Sr}.\left(\frac{^{87}Sr}{^{86}Sr}\right)_{gyps} \quad (4)$$

$$\left(\frac{Na}{Sr}\right)_{mix} = X_{sil}^{Sr}.\left(\frac{Na}{Sr}\right)_{sil} + X_{carb}^{Sr}.\left(\frac{Na}{Sr}\right)_{carb} + X_{gyps}^{Sr}.\left(\frac{Na}{Sr}\right)_{gyps} \quad (5)$$

$$1 = X_{sil}^{Sr} + X_{carb}^{Sr} + X_{gyps}^{Sr} \quad (6)$$

Where the subscripts *mix*, *sil*, *carb*, and *gyps* denote the mixture (water), the silicate, carbonate, and gypsum end members respectively. Proportions of Sr derived from each of those end members *i* are denoted X_i^{Sr}. All ratios are corrected from atmospheric and salt inputs according to the above method. Because the carbonate and gypsum end member add relatively few Na compared to Na* (Na from silicates), equation 5 simplifies into:

$$\left(\frac{Na}{Sr}\right)_{mix} = X_{sil}^{Sr}.\left(\frac{Na}{Sr}\right)_{sil} \quad (7)$$

This assumption is supported by the positions of the different springs in Fig. 4a, which indicates that the low-$^{87}Sr/^{86}Sr$ component of the springs - encompassing both carbonate and gypsum weathering - has a negligible Na content. The proportions of Sr in the different mixing reservoirs can then be estimated and the contribution of each of these end members to the load of the dissolved major species SO_4^{2-} and Mg^{2+} then calculated following:

$$X_i^E = X_i^{Sr}\left(\frac{E}{Sr}\right)_i / \left(\frac{E}{Sr}\right)_{spring} \quad (8)$$

with *i* = *sil*, *carb*, or *gyp*, and *E* = SO_4, or Mg (corrected from rain inputs). Full discussion is given in Appendix D on the choice of the $(Na/Sr)_{sil}$ (eq. 7) and more generally of the $(E/Sr)_i$ ratios (eq. 8), based on regression of the spring hydrochemical data and independent constraints from our geochemical analyses of the rock samples.

In carbonate-rich contexts like that of Séchilienne, dissolved Ca^{2+} concentrations can be affected by precipitation of secondary carbonates which tend to scavenge significant amounts of dissolved Ca relative to Mg and Sr (Bickle et al., 2015). For this reason, in principle eq. 8 cannot be applied for E = Ca and i = *carb*. The relatively high Mg/Ca ratios (around 0.9 mol/mol in springs G1, G2, and S10; and 0.2-0.4 mol/mol in springs S10 to S21; Table B1) and Sr/Ca ratios (around 2 mmol/mol in springs G1, G2, S10, S12, and S18; and above 6 mmol/mol for springs S13, S15, S20, and S21) compared to the estimated Mg/Ca and Sr/Ca ratios of the calcite end member at Séchilienne (below 0.1 mol/mol and 1 mmol/mol, respectively) determined from our geochemical analyses of rock samples (Table A1) are suggestive of a significant role of secondary carbonate formation. We quantify the role of secondary carbonate formation using the method proposed by Bickle et al. (2015), which is based on the comparison (in the Sr-Ca-Mg-Na compositional space) of the measurements in springs and the composition predicted from conservative mixing between the rock end members (Appendix D). In this analysis we contend that secondary carbonate formation affected waters containing solutes derived from the three rock end members identified for the Séchilienne springs (silicates, carbonates, and gypsum). We estimate that along the water flowpath secondary carbonate formation scavenges around 60% of the Ca initially released to solution by the combined dissolution of silicates, carbonates, and gypsum for springs G1, G2, and S10, whereas the effect of secondary carbonate precipitation is negligible for the other springs (Appendix D). These results highlight the potential role of lithological diversity, a characteristic of the bedrock material drained by springs G1, G2, and S10 in the UZ and BSZ (compared to other springs mostly influenced by the carbonate cover), in promoting secondary carbonate formation through mixing of compositionally different waters.

Another challenge in using eq. 8 at Séchilienne is the fact that both calcite and dolomite are reported to occur as carbonate minerals at Séchilienne - as confirmed by our own chemical analyses of rock samples (Tab. A1). Therefore, we take into account the presence of dolomite in our quantitative source apportionment, in particular regarding the $(Mg/Sr)_{carb}$ ratio used in eq. (8) (Appendix D). Based on arguments linked to the extent of secondary carbonate precipitation needed to explain the spring data (see above), we estimate that the contribution of dolomite dissolution to the overall Ca released by carbonate weathering at Séchilienne is about 10 to 20% (Appendix D).

In order to quantify the uncertainty associated to our mixing model, a Monte Carlo approach was used with 10,000 simulations. Results are given in Tab. D2 and represented in Fig. 5 as a stacked bar plot. In the following text, results on mixing proportions X_i^E are reported as $D_{50}{}^{+D_{84}}_{-D_{16}}$ (D_n is the n^{th} percentile of the output distribution over the 10,000 simulations; D_{50} is thus the median).

Carbonate dissolution appears as the major contributor to dissolved Ca, and to about half of dissolved Mg in all the springs sampled on the different parts of the studied zone (UZ, BSZ, MSZ), making this process a major supplier of cationic charges to waters at Séchilienne (Tab. D2; Fig. 5). In the most active part of the landslide (G1, G2), despite the silicate-dominated lithology, carbonate contribution is significant (about 40%), indicating the waters percolating though the unstable zone acquired part of their chemical and isotopic composition from above the hillslope. Calculations of the proportions of sulfate derived from the different end members show a minor but non negligible contribution of gypsum dissolution (reaching 88% of the total sulfate in spring S15) and a very clear contribution of pyrite oxidative weathering particularly important in the

fractured zone. In the G1-G2-S10 group of springs, most of the anionic charge (> 80%) is provided by the oxidative weathering of pyrite. Springs from the BSZ exhibit a lower proportion from silicate end member with a median of $0.48^{0.76}_{0.24}$ against $0.61^{0.84}_{0.38}$, $0.56^{0.81}_{0.31}$ for G1 and G2 (UZ), respectively. This contrast can be attributed to the unstable context of G1 and G2 compared to that of the stable part of the slope at the BSZ outflow.

In waters of the MSZ (S13-S21), significant contribution of gypsum is evidenced in the results of the mixing equations with values ranging between $0.20^{0.30}_{0.15}$ and $0.36^{0.48}_{0.29}$. These values are consistent with the mixing relationship presented in Fig. 4d. Therefore, and although significant uncertainty exists regarding the S isotope composition of the pyrite endmember, S isotope data lend support to our inference from the mixing model that waters are derived essentially from pyrite oxidation in the unstable zone, and from gypsum dissolution the MSZ waters (S13, S15, S18, S20, S21). The relative contribution of carbonates is also significant in MSZ waters with proportions ranging from $0.32^{0.58}_{0.09}$ for S18 to $0.33^{0.56}_{0.13}$ for S15.

Based on results of the mixing model, we can estimate a value for $\delta^{34}S$ of the pyrite endmember. Indeed, a significant linear negative relationship (R^2 = 0.8) exists between the $\delta^{34}S$ measured in springs across the Séchilienne massif and the modal estimates of their X_{sil}^{SO4} (Fig. D5). The intercept of this relationship at X_{sil}^{SO4} = 1 (equivalently at X_{gyp}^{SO4} = 0) gives an estimate for $\delta^{34}S_{sulfur}$ of -3.1‰. Such estimates are consistent with the range of measurements of solid sulfur reported in this study (ranging between -13.1‰ to 17.8‰) and reflect to an average value of the S isotope composition of sulfides for the Séchilienne unstable zone.

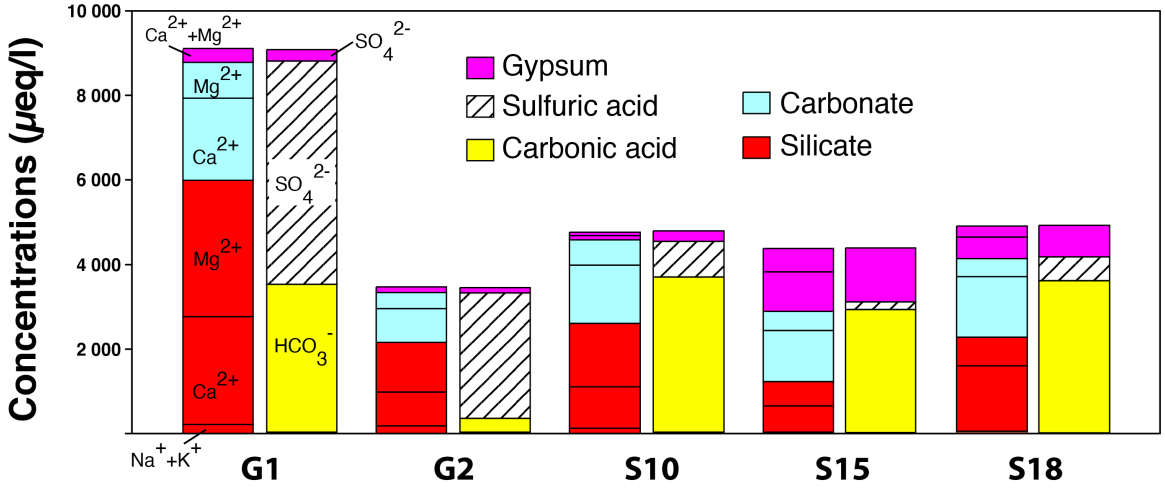

Figure 5: Concentration (in charge equivalents) calculated for major dissolved species and for each end member from the mixing model presented in the text and in the Appendix (Table D2). Silicates contribute for Na+K+Ca+Mg (Na+K not indicated), carbonates for Ca+Mg, gypsum dissolution for Ca+Mg (not distinguished). Note that ultimately the hydrogenocarbonate ion originates from respiration in soils. Sulfuric acid is generated by the oxidation of sulphide minerals, a process that occurs preferentially in the fractured zone. Relative contributions of different end members were obtained by solving a set of mixing equations using a Monte Carlo approach. Note that the relative contribution of each rock end member to the Ca^{2+} load here refers to that calculated for the Ca "initially" released into solution, that is before secondary carbonate precipitation (Appendix D).

5.2 Implications for hydrogeological processes at the Séchilienne site

Water plays an important role in the dynamics of slope instabilities, first as a physical (hydrogeological) process that can lead to aggravation of the instability. Secondly, water is a geochemical agent, which weather rocks and makes them less cohesive (Rutqvist and Stephansson, 2003; Binet, 2006; Cappa et al., 2004). These two categories of processes interact with each other in time as weathering leads to modifications in subsurface permeability and porosity, and thus in water flowpaths through the massif. Hydrological triggering is the most usual mechanism of initiation and reactivation of landslides but water flows in the subsurface have also been shown to have a major impact on the destabilization of a slope (de Montety et al. 2007; Guglielmi et al. 2002, Vallet et al. 2015b). However, landslides constitute very heterogeneous media due to their intense fracturation, which makes hydrogeological investigation complicated. The use of hydrochemistry and isotopic investigation is a good substitute to classical investigation. For example, groundwater dissolved $^{87}Sr/^{86}Sr$ ratios have proven to be useful in determining the sources of solutes in natural waters (Négrel and Deschamps, 1996, Négrel et al., 2001, Dotsika et al., 2010), investigating mineral weathering reactions (Brass, 1975; Åberg et al., 1989; Bullen et al., 1996; Clow and Drever, 1996; Bullen and Kendall, 1998), and identifying mixing processes involving groundwaters of different sources (Woods et al., 2000; Frost and Toner, 2004; Singleton et al., 2006) also inside an unstable context (Deiana et al., 2018). Values of groundwater dissolved $\delta^{34}S\text{-}SO_4^{2-}$ have also been used in aquifer studies to identify sulfate sources (Moncaster et al., 2000; Cortecci et al., 2002; Gammons et al., 2013). In particular, the Séchilienne hydrogeological model proposed by Vallet et al. (2015a) use sulfates as a tracer of waters flowing through the instability with the assumption that all SO_4^{2-} measured in groundwaters is sourced from pyrite oxidation. High sulfates concentrations in MSZ waters were indeed inferred by Vallet et al. (2015a) to be derived from a mixture of 30% of waters from the UZ (drained through the micro-fissured matrix) and 70% from the sedimentary cover (drained through both micro-fissured matrix and larger fractures), thereby establishing a hydraulic connection between the UZ and the MSZ waters (Fig. 1c).

Results from the present study partly support the hydrogeological model established by Vallet et al. (2015a) but allow us to refine this model through the identification of the contribution of another, unexpected end member corresponding to the dissolution of gypsum with a remote origin. Based on the local geological map (Barféty et al. 1972) gyspum occurrence has been reported but outside of the study zone, upstream along the Sabot fault which lies at the North-East of the MSZ outflows. As the fault is a major flowpath (Lajaunie et al., 2019), draining aquifers hosted by the sedimentary cover to the MSZ outflows, it contributes to the enrichment in SO_4^{2-} of those waters (Fig. 6). Our study therefore indicates a significant evaporitic origin for the sulfates in the MSZ waters, challenging the interpretation of Vallet et al. (2015a) of a hydrogeological connection between waters of the unstable and stable zones. Sulfate in outflows draining the UZ and BSZ is not strongly sourced from evaporites, but the part of those sulfates with evaporitic origin can be explained by a contribution of water flows through the Sabot fault towards the sedimentary cover and the basement formations (Fig. 6).

In addition, the systematic differences in elemental concentrations observed between the UZ and BSZ outflows (Tab. A2) can be linked to the structure of the slope and water flowpaths in the subsurface. Indeed, the S10 outflow drains a stable area (BSZ) just above the lowly-weathered, only slightly fractured basement. By contrast, the G1 and G2 outflows drain the unstable part of the slope (UZ), where the basement is highly fractured. This leads in turn stronger weathering degree of rocks and minerals there, and in particular of pyrite which is a major contributor to dissolved sulfate in the G1 and G2 outflows - more so than in the S10 outflow (stable and lowly weathered) characterized by lower sulfate contents.

Improving numerical and predictive models requires the incorporation of hydrological processes such as the dynamics of water circulation within a slope (directly dependent on fracturation, volumes of water involved, etc.). This study shows that isotopic proxies such as Sr and S isotopes ($^{87}Sr/^{86}Sr$, $\delta^{34}S$) coupled to water chemistry can be a very powerful tool to constrain groundwater origin and flowpaths in landslides and can substitute to tracer surveys, and constitute an alternative for hydrogeological investigation in logistically-challenging field environments such as unstable slopes.

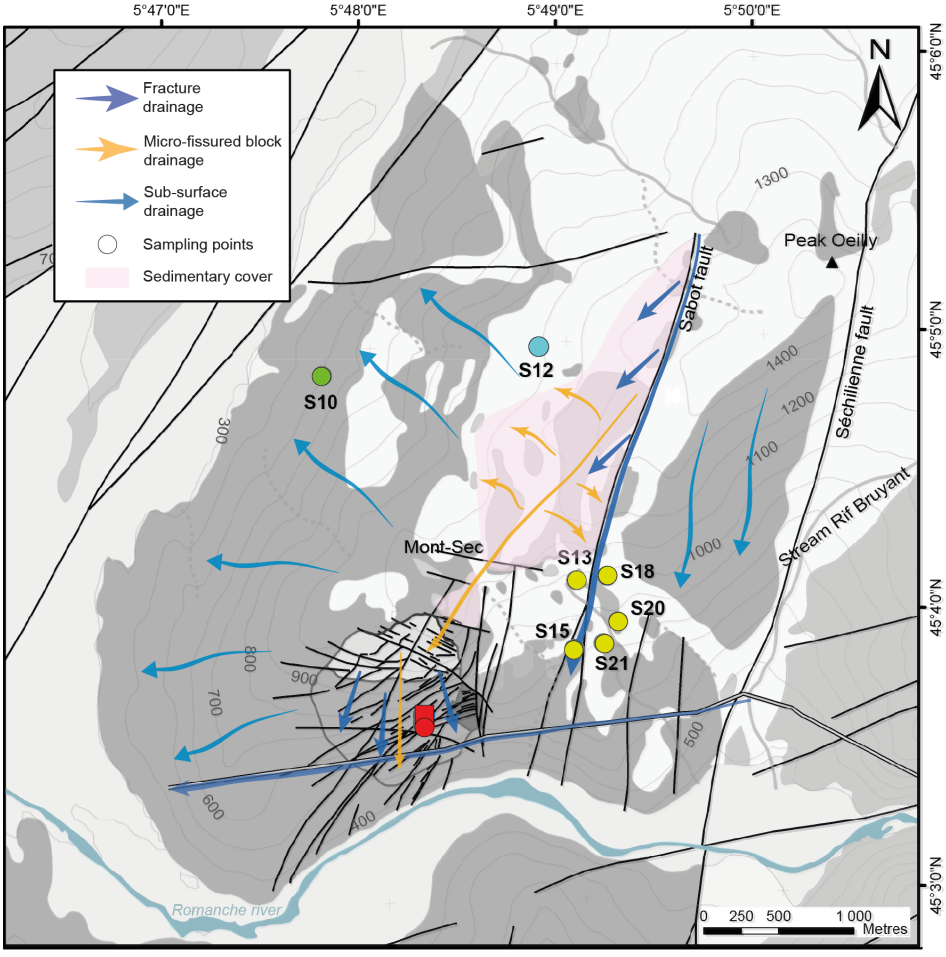

Figure 6: Sketch of the groundwater conceptual model, modified after Vallet et al., (2015).

5.3 Role of landslides on silicate weathering and CO_2 consumption

Recent studies have shown the importance of pyrite oxidation, sulfuric acid production, and associated chemical weathering in active landslides (Emberson et al. 2015, Emberson et al. 2016). In the following paragraph we examine the potential implications of the present study of the Séchilienne landslide for the global carbon cycle.

Rock weathering consumes atmospheric CO_2 and, associated with the precipitation of carbonates in the ocean, is the mechanism that has allowed for the sequestration of atmospheric CO_2 and consequently lower the Earth's surface temperature on geological timescales (Berner and Berner 2012). Rock forming-minerals uplifted to the Earth surface react with oxygen, carbonic acid produced by soil respiration, and sulfuric acid produced by the oxidation of sulfide minerals. The following reactions describe how carbonic (equations 9 and 11) and sulfuric (equations 10 and 12) acids interact with silicate (here wollastonite $CaSiO_3$) and carbonate minerals, and lead to the production of alkalinity (here HCO_3^-):

$$CaSiO_3 + 2CO_2 + H_2O \rightarrow SiO_2 + Ca^{2+} + 2HCO_3^- \quad (9)$$

$$CaSiO_3 + H_2SO_4 \rightarrow SiO_2 + H_2O + Ca^{2+} + SO_4^{2-} \quad (10)$$

$$CaCO_3 + CO_2 + H_2O \rightarrow Ca^{2+} + 2HCO_3^- \quad (11)$$

$$2CaCO_3 + H_2SO_4 \rightarrow 2Ca^{2+} + 2HCO_3^- + SO_4^{2-} \quad (12)$$

It is usually considered that when Ca^{2+} reaches the ocean, over a time period longer than 0.1 to 1 Myr, the precipitation of $CaCO_3$ releases CO_2 into the ocean-atmosphere system according to the reaction:

$$Ca^{2+} + 2HCO_3^- \leftrightarrow CaCO_3 + CO_2 + H_2O \quad (13)$$

The influence of the above reactions (equations 9-13) on atmospheric CO_2 partial pressure depends on the time scale considered (Torres et al., 2016). At short timescales (typically < 10^5 yrs), the chemistry of river discharge is able to influence the carbonate system in the ocean. Indeed, the delivery of alkalinity and Dissolved Inorganic Carbon (DIC) to the ocean to a ratio lower than that of the modern seawater ratio (Alk/DIC ~ 1) leads to increased dissolved CO_2 concentration, and consequently higher CO_2 content in the atmosphere through re-equilibration (Zeebe and Wolf-Gladrow, 2001). If the Alk/DIC ratio is higher than 1 but lower than 2, at time scales longer than that typical of carbonate precipitation in the ocean (10^5 to 10^6 yrs) but shorter than that of marine sulfate reduction to sulfide in sea bottom sediments (several 10^6 yrs), atmospheric CO_2 will increase because the precipitation of carbonates releases CO_2 to the ocean-atmosphere system that was not consumed on land by weathering reactions (combination of equations. 12 and 13). This mechanism should lead to global warming (Calmels et al., 2007) and has been invoked by Torres et al. (2014) for maintaining atmospheric CO_2 levels during the Himalayan orogeny, which otherwise should have led to a rapid atmospheric CO_2 depletion by enhanced silicate weathering. Finally, at timescales longer

than that typical of sedimentary burial of sulfide in the ocean, only silicate weathering by carbonic acid leads to net C sequestration (Berner et Berner, 1996; Calmels et al. 2007).

However, our analysis demonstrates that at Séchilienne reaction (13) also occurs directly on the continent through the formation of secondary carbonates, favored by the addition of calcium and alkalinity derived from silicate weathering, which results in a "short cut" of the carbon cycle. This short-term CO_2 release has to be taken into account when evaluating the overall CO_2 effect of weathering reactions at Séchilienne, and more generally in lithologically complex weathering systems where secondary carbonate formation is likely to involve solutes produced by a variety of processes, and in particular by carbonate weathering by sulfuric acid.

To this aim, we use the stoichiometry of reactions (9) to (13), together with the results of our quantitative source apportionment (section 5.1.4) to calculate the impact of weathering reactions at Séchilienne on atmospheric CO_2 over two scales (convoluted spatially and temporally), referred to in the following as "on site" or "local" (*i.e.*, immediately when weathering processes take place in the unstable zone) and "long term" or "global" (i.e., taking into account marine carbonate precipitation in the ocean ensuing solute delivery to the ocean).

Fig. 7 shows that waters produced in the Unstable Zone of Séchilienne (G1 and G2) act as CO_2 sources on the "long term", whereas waters produced in the bedrock stable zone (S10) or the mixed stable zone (S15, S18) are CO_2 sinks or CO_2-neutral within uncertainty. Our study thus shows that instabilities such as the Séchilienne landslide can act as hotspots of long-term CO_2 release to the atmosphere depending on the types of mineral-fluid interactions and also on the flow paths followed by the water drained in the landslide. We suggest that chemical weathering in similar landslides throughout the Alps (i.e Clapière, Super Sauze, and Valabres in the French Alps, Rosone in Italy; Barla et Chiriotti, 1995 ; Follacci, 1999 ; Binet, 2006) have a similar impact on global biogeochemical cycles and climate. Although it is beyond the scope of the present study to quantify the CO_2 fluxes linked to weathering in the Séchilienne landslide - let alone to attempt an extrapolation of such local results to the scale of the Alpine range - our work clearly shows that silicate and carbonate weathering by sulfuric acid generated in landslide zones of active mountain ranges have a climatic impact though a complex set of entangled short-term and long-term effects. Furthermore, this impact contradicts the textbook view that silicate weathering in mountain ranges consumes CO_2 from the atmosphere and cool the global climate (Raymo, 1991), and motivates more detailed studies associating hydrogeological and mineralogical approaches to build a more realistic understanding of the impact of mountains on climate change.

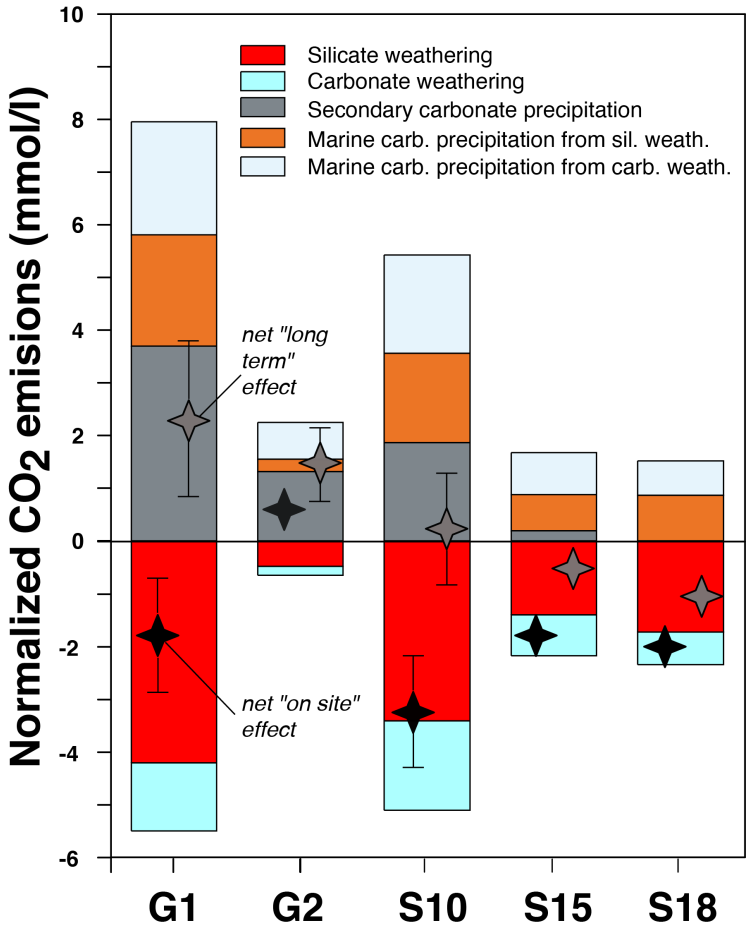

Figure 7: Evaluation of the effect of weathering processes at Séchilienne on atmospheric CO_2. The hydrochemistry of the springs G1 and G2 draining the instability ("Unstable Zone") show that the weathering results in long-term CO_2 production to the atmosphere because the cations are preferentially released in spring waters by the action of sulphuric acid and not carbonic acid from the soils (Table D3). In the Bedrock Stable Zone (spring S10) and in the Mixed Stable Zone (springs S15 and S18), weathering processes act as CO_2 sinks or are CO_2-neutral within uncertainty. Secondary carbonate precipitation returns CO_2 to the atmosphere. In particular, in the spring G2 of the Unstable Zone, this process results in a net "on site" CO_2 release because it involves precipitation of Ca and alkalinity derived from carbonate weathering by sulfuric acid.

6. Conclusion

We use measurements of dissolved major element chemistry coupled to Sr and S isotopic ratios in spring waters of the Séchilienne active landslide site in order to identify the chemical processes at play in the subsurface of the landslide area. Among these tracers, strontium isotopes allow us to allocate cations to different sources, circumventing issues affecting elemental ratios related to the precipitation of secondary. Silicate, carbonate, and evaporite weathering all appear to contribute to the cation load of the Séchilienne waters. Scavenging of dissolved calcium by secondary carbonate formation is identified

as a major process affecting solutes in the subsurface waters of the Séchilienne instability and favored by the mixing of different solution having interacted with a heterogeneous set of minerals. Sulfur isotopes bring a unique qualitative constraint on the origin of the sulfate ion, which is abundant in the Séchilienne groundwaters, showing the contribution of not only pyrite oxidation but also of gypsum dissolution.

The provenance of dissolved species at Séchilienne also reveals the complex water flow paths there. In particular, waters percolating through the landslide have acquired part of their hydrochemical characteristics far away from the unstable zone itself. For example, sulfur isotopes clearly indicate an unexpected contribution from Triassic sedimentary gypsum dissolution, that can only occur in the sedimentary layers capping the upper part of the massif and pointing out the importance of water drainage by a major fault of the massif.

The comparison between the stable and unstable parts of the site suggests that silicate weathering is enhanced in the fractured, unstable zone, where the landslide is active. Sulfur isotopes indicate that the production of acidity by the oxidation of magmatic sulfides enhances rock alteration in the unstable zone, this leads us to suggest the following feedback. By favoring the penetration of oxic waters and allowing contact with silicate minerals, fracturation and grain comminution controls the oxidation of pyrite that in turn rapidly generates sulfuric acid. The weathering of silicate minerals by sulfuric acid weakens the rock structure what in turn favors fracturation in response to the gravitational stress. Fletcher et al. (2006) and recently Behrens et al. (2015) have shown that opening of porosity at the rock-soil interface in soil profiles can be initiated by oxidation of Fe(II) minerals inducing a positive volume budget leading to the production of micro-cracks, inducing further weathering, at the origin of the opening of fractures, provided that enough carbonate and pyrite is present in the bedrock. At a larger scale, the feedback we propose here exemplifies a similar process of coupling between physical and chemical processes sustaining mass wasting in mountain ranges.

Finally, we demonstrate that the Séchilienne landslide is a hotspot of CO_2 release to the atmosphere over the long term. Although it remains difficult to upscale the results of the present study to the entire Alpine range, or to a global scale, landslides developed on sulfide-hosting sedimentary rocks appear to have a climatic impact opposite to the conventional view that rock weathering in mountains ranges consumes CO_2 from the atmosphere, and thus contributes to global cooling. In addition, our study shows a strong control of weathering processes and rates by local hydrogeological features, such as the complexity of flow paths setting the chemistry of the groundwaters within the unstable zone. More work is needed to assess the importance of landslides as hotspots of chemical alteration and geological CO_2 emissions, in particular to investigate their hydrological and hydrochemical response to weather and climate change. More generally, landslides epitomize the coupling between landscape evolution, tectonics and climate-weather. For this reason - as well as that of their societal impact in terms of natural hazard - monitoring landslides over a range of time scales and frequency should become a priority.

Appendices

Appendix A: Bedrock analyses

Table A1: Major, trace elements concentration and strontium isotopic compositions of rock samples of the Séchilienne slope

Concentration in rock samples (in ppm relative to total rock mass)	Li	Be	Na	Mg	Al	K	Ca	Ti	V	Cr	Mn	Fe	Co	Ni	Cu	Zn	As	Rb	Sr
"Lias" limestone																			
H_2O leachate	0,035	0,004	1,86	113	0,77	12,3	61,7	0,000	0,003	0,001	0,071	1,543	0,001		0,002		0,004	0,040	0,140
Ac. Ac. leachate	0,392	0,113	20	14242	10,3	21,1	30498	0,067	0,235	0,070	147	998	0,611	1,002	0,003	33,17	0,019	0,022	21,70
HCl leachate	0,887	0,033	79	45085	7,7	13,5	86109		0,006	0,001	303	5732	0,116	0,575	0,011	6,863	0,016	0,022	60,52
Residue	4,76	0,184	187	51193	1085	427	97029	51	4,420	1,288	187	5785	0,717	2,015	1,64	15,95	1,654	2,059	45,58
Bulk	9,8	0,5	501	127456	1166	1329	220499	55	5	2,4	646,6	16782	1,9	4,8	3,28	76,5	1,92	2,67	152
Sum of leachate / Bulk	0,62	0,73	0,57	0,87	0,95	0,36	0,97	0,93	0,95	0,56	0,99	0,75	0,76	0,74	0,51	0,73	0,88	0,80	0,84
"Laffrey" limestone																			
H_2O leachate	0,066	0,012		13,0	1,85	25,1	297		0,007	0,004	0,109	0,745	0,002		0,009	0,205	0,019	0,081	3,368
Ac. Ac. leachate	0,189	0,242	0,383	1561	38,9	58,9	240693	0,220	1,003	0,172	382	1003	0,053	0,447	0,037	2,835	0,164	0,059	342,59
HCl leachate	0,104	0,148		1041	76,9	40,6	40863	0,119	0,803	0,126	77	891	0,215	1,405	0,938	5,493	0,188	0,134	61,54
Residue	3,11	0,123	150	178	3263	1354	877	127	6,814	2,795	2,88	1710	1,634	8,214	1,895	2,316	0,977	7,240	2,853
Bulk	5,79	0,711	401	3659	4522	2664	344063	180	10,9	5,17	553,4	4771	2,55	13,7	4,91	20,0	2,25	11	532
Sum of leachate / Bulk	0,60	0,74	0,38	0,76	0,75	0,55	0,82	0,71	0,79	0,60	0,84	0,76	0,75	0,74	0,59	0,54	0,60	0,70	0,77
Micaschiste																			
H_2O leachate	0,035	0,002	21	1,71	7,42	64,6	0,71	0,035	0,012	0,007	0,023	4,302	0,005	0,006	0,007	0,006	0,067	0,119	0,013
Ac. Ac. leachate	0,758	0,096	74	273	798	511	474	0,228	0,838	0,795	14,9	689	0,977	1,271	0,826	1,907	1,145	1,074	3,184
HCl leachate	3,36	0,047	24	654	1484	199	1295	3,723	1,402	2,028	12,6	2465	0,720	3,125	0,526	4,220	2,460	0,673	6,315
Residue	17,3	1,366	14459	4926	57017	17831	585	2791	48,62	41,37	57	12151	5,303	16,440	4,636	25,346	1,706	75,619	40,181
Bulk	27,0	2,32	13436	7150	70048	22490	2813	3407	60	64,4	94,5	18792	10,5	28,3	7,7	41,1	5,5	111	59
Sum of leachate / Bulk	0,79	0,65	1,08	0,82	0,85	0,83	0,84	0,82	0,84	0,69	0,90	0,81	0,67	0,74	0,78	0,77	0,97	0,70	0,84
Vein																			
H_2O leachate	0,103	0,001	56	4,20	0,492	13,5	17,8	0,003	0,002	0,001	0,200	1,429	0,009	0,007	0,005	0,015	0,022	0,038	0,273
Ac. Ac. leachate	0,168	0,009	16,3	115	63	26	393	0,057	0,062	0,058	14,9	220	0,898	0,468	0,153	0,690	0,293	0,093	2,681
HCl leachate	0,258	0,004	3,57	73	104	23	154	0,496	0,091	0,153	5,22	339	0,108	0,340	0,077	0,479	0,691	0,126	1,234
Residue	5,50	0,108	1244	371	4156	1223	74	197	3,412	3,097	6,18	966	0,340	1,090	0,387	2,044	0,157	5,520	4,015
Bulk	9,22	0,142	1497	592	4631	2089	648	216	3,75	4,87	26,7	1704	1,66	2,57	1,94	5,51	1,41	6,50	8,93
Sum of leachate / Bulk	0,65	0,85	0,88	0,95	0,93	0,62	0,99	0,91	0,95	0,68	0,99	0,90	0,82	0,74	0,32	0,59	0,83	0,89	0,92

Concentration in rock samples (in ppm relative to total rock mass)	Y	Zr	Nb	Cs	Ba	La	Ce	Pr	Nd	Sm	Eu	Gd	Tb	Dy	Ho	Er	Tm	Yb	Lu
"Lias" limestone																			
H_2O leachate	0,001	0,000	0,004	0,001	0,030	0,000	0,000	0,000	0,000	0,000	0,000	0,000	0,000	0,000	0,000	0,000	0,000	0,000	0,000
Ac. Ac. leachate	1,195	0,007	0,001	0,000	3,582	0,256	0,552	0,074	0,354	0,155	0,143	0,220	0,033	0,172	0,032	0,081	0,010	0,053	0,007
HCl leachate	1,165	0,002	0,002	0,001	1,926	0,284	0,532	0,058	0,249	0,079	0,046	0,138	0,021	0,121	0,026	0,070	0,009	0,042	0,006
Residue	2,329	1,571	0,203	0,145	21,22	0,565	1,324	0,162	0,695	0,237	0,105	0,317	0,053	0,318	0,065	0,191	0,024	0,143	0,020
Bulk	5,55	2,26	0,25	0,215	32,09	1,34	3,03	0,38	1,65	0,63	0,37	0,84	0,14	0,78	0,17	0,45	0,06	0,32	0,05
Sum of leachate / Bulk	0,85	0,70	0,85	0,69	0,83	0,82	0,80	0,77	0,79	0,75	0,80	0,80	0,76	0,78	0,73	0,77	0,70	0,75	0,71
"Laffrey" limestone																			
H_2O leachate	0,002	0,003	0,018	0,004	0,024	0,001	0,002	0,001	0,001	0,001	0,000	0,001	0,000	0,000	0,000	0,000	0,000	0,000	0,000
Ac. Ac. leachate	4,463	0,103	0,004	0,002	3,243	3,435	4,811	0,774	3,329	0,691	0,416	0,711	0,101	0,557	0,117	0,333	0,044	0,280	0,042
HCl leachate	1,108	0,092	0,006	0,030	1,478	0,704	1,084	0,190	0,851	0,184	0,100	0,191	0,027	0,152	0,029	0,085	0,012	0,074	0,010
Residue	0,248	3,223	0,464	0,490	32,50	0,477	0,703	0,074	0,227	0,019	0,016	0,026	0,004	0,030	0,007	0,027	0,004	0,028	0,005
Bulk	7,84	4,35	0,67	0,73	49,05	6,19	8,95	1,42	5,99	1,2	0,70	1,24	0,17	0,96	0,20	0,59	0,08	0,50	0,08
Sum of leachate / Bulk	0,74	0,79	0,73	0,72	0,76	0,75	0,74	0,73	0,74	0,76	0,76	0,75	0,79	0,77	0,75	0,76	0,74	0,77	0,75
Micaschiste																			
H_2O leachate	0,002	0,001	0,003	0,004	0,083	0,008	0,016	0,002	0,007	0,001	0,000	0,001	0,000	0,000	0,000	0,000	0,000	0,000	0,000
Ac. Ac. leachate	0,442	0,002	0,001	0,009	10,288	0,409	0,844	0,103	0,413	0,096	0,024	0,105	0,016	0,086	0,015	0,040	0,005	0,030	0,004
HCl leachate	1,649	0,043	0,003	0,032	6,173	1,204	2,596	0,314	1,325	0,348	0,077	0,402	0,062	0,313	0,055	0,147	0,018	0,107	0,014
Residue	12,881	14,56	11,173	2,476	395,42	22,44	44,752	5,237	19,85	3,43	0,686	2,978	0,402	2,083	0,404	1,156	0,155	0,920	0,120
Bulk	25,7	27,8	12,9	3,5	563	28,9	59,2	7,0	26,0	5,1	1,05	4,85	0,74	4,28	0,87	2,40	0,34	2,07	0,25
Sum of leachate / Bulk	0,58	0,53	0,87	0,72	0,73	0,83	0,81	0,81	0,83	0,77	0,75	0,72	0,65	0,58	0,54	0,56	0,53	0,51	0,54
Vein																			
H_2O leachate	0,001	0,000	0,001	0,007	0,018	0,001	0,001	0,000	0,001	0,000	0,000	0,000	0,000	0,000	0,000	0,000	0,000	0,000	0,000
Ac. Ac. leachate	0,158	0,001	0,000	0,009	1,182	0,038	0,097	0,014	0,070	0,025	0,009	0,034	0,006	0,032	0,006	0,015	0,002	0,011	0,001
HCl leachate	0,220	0,007	0,001	0,032	0,564	0,098	0,246	0,037	0,192	0,071	0,020	0,091	0,014	0,062	0,009	0,019	0,002	0,010	0,001
Residue	1,170	1,319	0,742	0,355	28,165	1,224	2,441	0,280	1,056	0,194	0,042	0,191	0,030	0,174	0,036	0,105	0,014	0,084	0,011
Bulk	1,06	0,66	0,73	0,47	32,2	1,49	3,09	0,386	1,51	0,33	0,08	0,32	0,05	0,22	0,04	0,09	0,01	0,07	0,008
Sum of leachate / Bulk	1,47	2,02	1,02	0,85	0,93	0,91	0,90	0,86	0,87	0,88	0,89	0,98	1,07	1,21	1,32	1,54	1,45	1,53	1,61

Concentration in rock samples (in ppm relative to total rock mass)	Pb	Th	U	Contrib. to total Ca (%)	Sr/Ca mmol/mol	Mg/Ca mol/mol	Na/Ca mol/mol	87Sr/86Sr	s.d.
"Lias" limestone									
H_2O leachate	0,005	0,003	0,003	0,03	1,08	3,16	0,055		
Ac. Ac. leachate	3,469	0,057	0,558	13	0,34	0,80	0,0012	0,710395	0,000005
HCl leachate	0,453	0,002	0,126	37	0,33	0,90	0,0017	0,709767	0,000003
Residue	7,323	0,307	2,448	42	0,22	0,91	0,0035	0,708834	0,000004
Bulk	17,1		4,00		0,31	0,95	0,0039	0,709540	0,000014
Sum of leachate / Bulk	0,66		0,78					0,84	
"Laffrey" limestone									
H_2O leachate	0,006	0,001	0,000	0,08	5,40	0,075		0,710629	0,000007
Ac. Ac. leachate	1,493	0,439	0,012	67	0,68	0,011	0,0000029	0,710539	0,000004
HCl leachate	2,126	0,165	0,006	11	0,72	0,04		0,710409	0,000008
Residue	0,709	0,247	0,084	0,24	1,55	0,35	0,31	0,717934	0,000027
Bulk	6,0	0,48	0,10		0,71	0,018	0,0020	0,710573	0,000003
Sum of leachate / Bulk	0,73		1,02					0,77	
Micaschiste									
H_2O leachate	0,012	0,016	0,002	0,02	8,39	4,12	54,20		
Ac. Ac. leachate	0,967	1,060	0,160	16	3,20	0,99	0,28	0,728147	0,000005
HCl leachate	1,967	7,461	0,698	44	2,32	0,87	0,034	0,720109	0,000013
Residue	4,351	10,770	1,792	20	32,7	14,5	44,9	0,735581	0,000018
Bulk	12,1	10,3	3,4		9,62	4,18	8,31	0,735077	0,000014
Sum of leachate / Bulk	0,60		0,78					0,88	
Vein									
H_2O leachate	0,003	0,001	0,000	2,6	7,31	0,41	5,75		
Ac. Ac. leachate	0,362	0,065	0,010	58	3,25	0,50	0,075	0,724583	0,000004
HCl leachate	0,778	0,343	0,024	23	3,81	0,82	0,042	0,722884	0,000005
Residue	0,347	0,926	0,076	11	25,8	8,58	30,4	0,731125	0,000016
Bulk	1,37	0,583	0,09		6,29	1,50	4,02	0,727672	0,000004
Sum of leachate / Bulk	1,09		1,30					0,84	

Table A2: Sulfate isotopic compositions of bedrock samples of the Séchilienne slope

	Sample	Sampling dep	$\delta^{34}S$ (‰)	Mean $\delta^{34}S$	s.d
Weathered micaschist	SC2 19.71 A _ 1	19.71	-7.94	-0.74	9.36
	SC2 19.71 A _ 2	19.71	-7.76		
	SC2 19.71 B _ 1	17.71	-7.21		
	SC2 19.71 B _ 2	19.71	-7.01		
	SC2 108.50 _ 1	108.5	17.77		
	SC2 108.50 _ 2	108.5	17.56		
	SC2 132.50 _ 1	132.5	1.67		
	SC2 132.50 _ 2	132.5	1.99		
Unweathered micaschist	SC1 84.2 (1) _ 1	84.2	-6.58	-0.31	8.21
	SC1 84.2 (1) _ 2	84.2	-6.56		
	SC2 128 _ 1	128	-4.12		
	SC2 128 _ 2	128	-4.28		
	SC2 106.80 _ 1	106.8	9.87		
	SC2 106.80 _ 2	106.8	10.10		
	SC1 42.3 (5) _ 1	42.3	-3.32		
	SC1 42.3 (5) _ 2	42.3	-3.40		
	SC1 42.3 (5) _ 3	42.3	-3.21		
	SC1 80.3 (4)	80.3	0.88		
	SC1 30.60 (2)	30.6	-13.13		

Appendix B: Chemical and isotopic composition of waters from the Séchilienne slope and rainwaters

Table B1: Chemical and isotopic composition of waters samples of the Séchilienne slope

Outflow	Date	Ca	Mg	Na	Na*	K	F	Cl	NO_3	SO_4	HCO_3	SiO_2	Sr	Li	EC	T	pH	$^{87}Sr/^{86}Sr$	$\delta^{34}S$
		µmol.L^{-1}	µmol.L^{-1}	µmol.L^{-1}	µmol.L^{-1}	µmol.L^{-1}	µmol.L^{-1}	µmol.L^{-1}	µmol.L^{-1}	µmol.L^{-1}	µmol.L^{-1}	µmol.L^{-1}	µmol.L^{-1}	µmol.L^{-1}	µS/cm	°C			‰
G1	18/11/2010	2495	2345	187	140	36	11	55	1.5	2729	3279	114			613	10.6	7.6		
G1	03/02/2011	2208	1954	200	150	30	13	58	0	2527	3091	112			735	10.5	8.6		
G1	28/02/2011	2358	2181	257	210	33	12	55	1.6	2723	2955	115			797	10.06	8.2		
G1	01/04/2011	2408	2057	239	192	30	15	55	0	2617	3271	116			825	11.4	8.2		
G1	01/06/2011	2508	2255	274	227	33	16	55	0	2736	3391	115			846	12.7	8.5		
G1	05/10/2011	2470	2551	265	219	51	11	54	5.3	3302	3359	112			891	11.8	8.1		
G1	11/01/2012	2745	2448	96	50	30	12	53	0	3221	3039	116			892	10.9	8.2		
G1	15/02/2012	2370	2325	244	189	31	13	63	0	2940	2911	111			837	10.6	8.42		
G1	27/03/2012	2445	2530	291	242	35	13	57	5.1	3071	3299	119			906	10.5	8.1		
G1	27/06/2012	2545	2325	246	201	35	15	53	0	2768	3447	119			843	11.2	8.0		
G1	25/09/2012	2645	2325	263	217	36	12	53		2938	3507	116			910	11.3	7.9		
G1	08/01/2013	2196	1958	233	187	30	11	53	6.2	2266	3187	118			750	11.1	8.2		
G1	16/04/2013	2233	2016	224	169	42	11	64	39.8	2315	3583	124			750	11.2	8		
G1	17/07/2013	2174	1966	213	169	32	7	52	7.2	2224	3275	120			719	12.4	8.0		
G1	17/09/2013	2187	2230	218	179	31	9	47	3.4	2570	3123	117			771	11	8.2		
G1	15/12/2013	2237	1862	201	154	32	11	55	67.4	2584	2851	121			806	10.6	8.2		
G1	09/03/2014	1913	1647	190	152	25	11	44	2.6	1964	3471	130			686	11.1	8.1		
G1	14/06/2014	2131	2056	204	201	29	13	4		2414	3655	136	6		762	11.4	8.2	0.7213	
G1	09/10/2014	2570	2313	244	164	85	7	94	23.1	2844	3518	131	6		834	11.2	8.3		
G1	20/04/2015	2283	2093	219	177	33	11	49	7.1	2194	3851	137	5		752	11.5	7.9		
G1	13/07/2015	2157	2031	210	112	96	8	115	8.1	2755	3506	127	5		795	11.9	8.1		
G1	15/10/2015	2076	2139	209	169	31	7	48	8.2	2786	3063	110	5		821	10.7	8		
G1	19/11/2015	2446	2239	229	184	35	11	52	5.6	2986	3623	115	6	4.2	894	11.2	7.9	0.7214	
G1	11/01/2016	2365	2272	228	191	40	12	42	8.3	3907	3107	265	2	2.8	868	10.9	7.6		
G1	19/04/2016	2243	2138	211	176	36	9	41	8.8	2986	3479	121	5	3.7	844	11.2	7.2		
G1	19/05/2016	2210	1787	204	176	29	12	32		2204		125	5	2.2				0.7213	
G1	19/05/2016	2237	1950	213	184	30	11	35		2543		127	5	3.4	823	11	7.87	0.7213	
G1	20/05/2016	2286	1933	219	190	31	11	34	0.4	2610		128	5	3.4	833	11.5	7.98	0.7213	
G1	20/05/2016	2240	1917	216	186	30	11	34	0.3	2620		128	5	3.5				0.7213	
G1	20/05/2016	2260	1974	219	189	34	11	36		2595		128	5	3.3				0.7213	
G1	20/05/2016	2259	1933	219	189	38	11	34	0.4	2600		130	5	3.7				0.7223	
G1	20/05/2016	2253	1936	214	185	30	11	34	0.3	2592		124	5	3.5	858	11.5	7.95	0.7222	
G1	08/09/2016	2408	2371	224	190	35	9	39	3.5	2934	3361	120	6	2.1	838	11.8	8.0		
G1	05/12/2016	2294	2499	224	197	34	9	31	10.6	3381	2703	107	6	3.5	856	10.8	8.3		
G1	09/03/2017	2252	2643	205	150	54	10	64	6.1	3589	2678	95	6	4.6	874	10.9	7.3		
G1	12/06/2017	2364	2455	223	149	90	12	87	1.9	3158		122	6	5.0	900	11.4	8.2		
G1	25/01/2018	2440	2174	224	196	32	11	33	3.8	3127	3442	125	6	5.8	893	10.9	8.4		
G1	19/02/2018	2226	2028	232	200	41	12	37	3.8	2981	3230	121	5	5.7	849	10.6	8.4		
G1	03/04/2018	2317	2054	225	181	48	13	51	4.0	2696	3672	129	5	5.4	837		7.5		
G1	17/09/2018	2278	2216	252	223	41	11	34	5.4	2967	3332	129	6	6.8	1114	11.2	8.3		
G1	09/04/2019	2035	2158	185	159	28	11	40	2.7	2901	4079	97	5	3.7	803		8.1	0.7212	-2.12
G2	17/11/2010	686	667	130	88	34	27	49	3.6	1376	56	364			313		6.6		
G2	03/02/2011	898	802	204	150	36	29	63	0	1541	480	267			361	9.2	8.5		
G2	01/04/2011	886	823	222	173	35	32	57	0	1615	372	305			375	10.3	8.3		
G2	05/10/2011	936	831	191	146	97	21	54	5.6	1468		213			385	12.1	7.4		
G2	11/01/2012	848	798	209	166	32	29	49	3.3	1609	232	314			363	10.3	8.1		
G2	15/02/2012	1073	864	209	158	40	28	59	14.2	1640	552	252			389	8.6	8.1		
G2	28/03/2012	898	996	226	182	39	28	51	10.7	1678	604	260			418	10.6	7.7		
G2	27/06/2012	848	774	178	141	37	28	43	16.7	1356	624	0			338	12.5	8.1		
G2	25/09/2012	1160	1020	226	178	43	27	56	45.4	1855		226							
G2	15/12/2013	791	658	159	119	30	26	47	3.1	1437	404	269			355	10.2	8.0		
G2	09/03/2014	647	630	171	130	30	28	48		1320	196	333			317	10.8	7.9		
G2	19/11/2015	950	875	181	142	40	24	46	19.3	1694	752	0	2	3.1	470	11.2	7.8	0.7207	
G2	11/01/2016	933	857	184	119	72	23	75	11.9	1769	700	116	6	3.9	404	10.8	8.2		
G2	19/04/2016	827	811	172	138	39	21	40	7.7	1676	600	272	2	3.1	385	10.7	6.9		
G2	19/05/2016	782	744	181	145	34	25	41	1.6	1530		287	2	2.8	371	10.6	7.68	0.7205	
G2	19/05/2016	875	910	179	143	39	23	41	4.3	1542		234	2	3.0	485	10.7	7.97	0.7205	
G2	19/05/2016	796	755	184	148	35	25	43		1551		286	2	2.9	427	10.8	7.5	0.7205	
G2	20/05/2016	807	764	182	147	34	25	42		1540		285	2	2.9				0.7205	
G2	20/05/2016	784	765	179	144	33	25	40		1542		283	2	2.8				0.7206	
G2	20/05/2016	769	751	176	142	33	25	40		1543		287	2	2.9				0.7205	
G2	20/05/2016	798	770	179	145	34	24	41	2.7	1540		278	2	2.7	451	11.3	7.62	0.7206	
G2	20/05/2016	825	787	184	148	35	24	42		1525		282	2	2.9				0.7205	
G2	20/05/2016	810	772	181	145	34	2	42	2.9	1525		280	2	2.9	426	11.6	7.85	0.7206	
G2	08/09/2016	1015	1008	186	149	39	27	44	13.8	1763	624	267	2	1.4	427	13			
G2	09/03/2017	885	936	167	125	38	26	49	10.9	1680	584	227	2	2.9	390	9.9	6.6		
G2	12/06/2017	731	751	151	117	46	25	39	10.4	1300		235	2	2.8	372	11.6			
G2	21/08/2017	941	781	171	144	35	25	32	19.6	1638	620	119	2	4.2	372	11.6		0.7206	
G2	25/01/2018	691	691	165	127	45	26	45	2.9	1475	220	318	2	3.4	451	9.9	8.4		
G2	19/02/2018	780	742	178	134	58	23	52	3.7	1583	353	297	2	3.6	447	10	8.4		
G2	03/04/2018	683	681	181	141	39	30	47	1.6	1355	160	351	2	3.8	406		7.2		
G2	17/09/2018	896	846	200	168	71	26	37	52.4	1377	613	278	2	4.4	426	11.9	7.7		
G2	09/04/2019	744	793	159	133	37	28	45	2.7	1582	353	265	2	3.0	360		7.1	0.7203	-5.45
S10	24/09/2010	1285	1103	165	131	23	6	40	17.6	553	3751	167			451	12.7	7.6		
S10	18/11/2010	1297	1086	78	44	17	6	40	19.0	545	3835	151			308		6.7		
S10	18/11/2010	1335	1144	91	49	26	6	49	17.8	565	3887	157			314		6.8		
S10	02/02/2011	1198	1070	126	91	15	6	40	22.3	508	3651	143			422	8.4	7.5		
S10	03/02/2011	1248	1059	135	99	20	7	42	26.5	531	3679	152			435	7	7.8		

675

S10	28/02/2011	1273	1111	148	112	21	7	42	23.6	541	3655	154			447	9.1	7.9			
S10	01/03/2011	1235	1127	135	101	15	7	39	21.1	521	3683	145			445	8.8	7.4			
S10	01/04/2011	1235	1090	135	100	16	8	40	21.0	520	3939	145			437	8.9	7.4			
S10	01/04/2011	1248	1111	144	109	21	8	41	22.7	541	3771	154			441	9.7	7.9			
S10	02/06/2011	1285	1111	144	110	16	8	39	17.5	530	3783	145			440	9.2	7.8			
S10	02/06/2011	1310	1111	157	123	20	8	40	16.0	553	3855	155			448	10	8.0			
S10	04/10/2011	1322	1177	157	122	22	6	40	13.5	578	3999	157			473		8.1			
S10	10/01/2012	1335	1086	113	80	19	6	39	30.6	554	3807	156			462	8.5	8.2			
S10	10/01/2012	1273	1119	139	107	15	6	37	16.7	522	3763	145			446	8.5	7.6			
S10	28/03/2012	1273	1185	148	113	16	7	41	17.8	541	3703	148			459	7.45	9.4			
S10	28/03/2012	1285	1193	152	116	20	7	43	16.6	566	3699	155			462	9.4	7.9			
S10	28/06/2012	1205	1177	137	104	16	6	39	17.2	527	3719	146			441	10.5	7.7			
S10	28/06/2012	1248	1185	146	111	20	10	41	15.5	552	3743	154			451	11.7	8.1			
S10	26/09/2012	1385	1094	152	119	20	6	39	13.4	575	3991	158			466	11.4	8.2			
S10	08/01/2013	1322	1070	126	92	16	5	39	22.5	492	3355	144			404	8.09	7.6			
S10	08/01/2013	1260	1136	135	100	21	6	41	29.2	541	3571	150			425	9.2	8.1			
S10	17/09/2013	1216	1202	125	95	19		35	13.1	544	3619	151			447	10.9	8.1			
S10	16/12/2013	1242	963	118	83	19	5	41	17.2	568	3675	156			452	8.5	8.1			
S10	10/03/2014	1105	1013	118	91	19	5	31	26.3	542	3711	160			416	9.3	8.0			
S10	14/06/2014	1162	1152	120	91	18	5	34	15.8	536	3675	164	3		435	11.4	8.1	0.7150		
S10	14/06/2014	1100	1113	110	82	14	6	32	21.1	508	3499	157	3		419	10.2	8.0	0.7147		
S10	09/10/2014	1291	1062	136	105	21	5	36	12.7	555	3823	172	3		432	10.6	8.1			
S10	09/10/2014	1204	1062	122	93	16	5	34	18.2	534	3711	156	3		440	9.4	7.8			
S10	20/04/2015	1097	1068	117	86	15		36	22.1	481	3419	153	2		400	9.3	7.5			
S10	20/04/2015	1210	1151	129	97	20	4	36	21.6	532	3659	160	3		428	10.2	8.0			
S10	13/07/2015	1184	1053	123	93	18		35	14.3	559	3792	156	3		441	11.8	8.2			
S10	13/07/2015	1114	1034	110	83	14	3	32	18.3	536	3621	145	2		433	10.1	7.8			
S10	15/10/2015	1226	1108	123	92	19		36	13.5	565	4063	158	3		461	9.7	8.2			
S10	19/11/2015	1193	1057	123	92	20	5	36	14.3	577	4043	145	3	1.3	475	10.5	8.2	0.7148		
S10	11/01/2016	1279	1128	131	99	22	5	37	16.1	582	3991	163	3	1.2	464	8.6	8.0			
S10	19/04/2016	1144	1068	115	89	15	5	30	14.8	522	3823	147	3	1.5	440	9.5	7.2			
S10	19/04/2016	1178	1073	123	100	20	5	27	17.1	544	3823	153	3	1.2	448	10.3	8.0			
S10	20/05/2016	1198	1046	132	107	22	4	30	17.5	508		152	3	1.2	478	7.89	10.1	0.7150		
S10	08/09/2016	1267	1172	122	101	12	5	24	13.3	524	3866	149	3		454	10.7	7.5			
S10	08/09/2016	1249	1178	123	100	18	5	26	12.1	545	3981	148	3		464	12.1	8.1			
S10	05/12/2016	1307	1222	130	106	23	7	28	12.1	587	4021	152	3	1.2	483	9	8.2			
S10	09/03/2017	1303	1298	125	101	20	7	28	14.6	586	4085	152	3	2.1	474	9.7	8.2			
S10	12/06/2017	1263	1182	130	111	19	6	23	18.3	551		159	3	2.1	477	10.9	7.3			
S10	12/06/2017	1254	1174	122	105	15	6	19	13.2	539		153	3	2.2	474	11.3	7.4			
S10	21/08/2017	1316	996	120	113	14	4	21	10.4	545	4044	70	3	3.2	474	11.3	7.4	0.7145		
S10	21/08/2017	1277	1031	125	98	19	5	24	9.3	560	4056	72	3	3.1	477	10.9	7.3	0.7150		
S10	20/11/2017	1319	1235	134	228	21	5	25	8.3	581		165	3	2.3	500	9.8	8.1			
S10	25/01/2018	1157	1057	120	83	19	5	27	30.3	550	3751	154	3	2.4	476	8.7	8.3			
S10	19/02/2018	1182	1044	250	144	73	5	26	23.7	547	3771	160	3	2.4	448	9.42	8.1			
S10	07/03/2018	987	910	103	125	16	6	24	21.2	534	3752	134	2	1.8	410	10.8	8.1			
S10	03/04/2018	1532	1533	171	106	26	6	32	21.6	513	3480	220	4	2.8	437		6.5			
S10	17/09/2018	1284	1114	147	103	22	8	25	13.3	554	3974	172	3	3.0	490	12.6	7.7			
S10	09/04/2019	1152	1124	112	86	18	5	32	16.7	543	4513	125	2	1.5	443		8.0	0.7150	2.38	
S12	23/09/2010	412	115	148	124	10	3	27	44.5	89	864	144			125	11.5	7.3			
S12	25/09/2010	474	103	74	51	8		26	41.1	51	960	136			122	10.2	8.1			
S12	18/11/2010	449	91	70	48	9	4	26	41.1	90	940	137			79		6.7			
S12	02/02/2011	387	82	70	47	7	0	27	45.3	79	836	130			104	4.2	7.9			
S12	01/03/2011	424	99	65	42	8	0	27	41.0	82	900	133			114	4.7	7.8			
S12	31/03/2011	399	93	65	43	8	0	26	39.2	80	888	130			108	6.2	7.7			
S12	02/06/2011	437	105	74	50	9	2	28	42.5	85	920	132			117	7.8	7.8			
S12	04/10/2011	462	107	74	50	10	0	27	38.7	89	656	134			120	10.8	7.8			
S12	28/03/2012	424	91	70	47	8	0	26	34.6	84	848	133			117	5.5	8			
S12	28/06/2012	412	99	74	52	9	0	26	39.7	84	904	134			116	10.8	8			
S12	08/01/2013	399	99	67	46	8	3	25	40.2	36	752	133								
S12	17/09/2013	416	113	63	45	8		22	41.1	79	840	134			113	8.4	7.7			
S12	14/06/2014	401	104	58	40	7		20	57.1	80	864	143	1		115	9.3	7.9	0.7095		
S12	09/10/2014	440	100	68	50	9		21	48.2	84	948	149	1		118	10.1	8.3			
S12	20/04/2015	382	96	63	47	9		19	63.7	74	824	139	1		104	6.6	7.9			
S12	13/07/2015	418	102	65	46	8		21	54.5	84	896	141	1		119	11.5	8.9			
S12	15/10/2015	406	101	62	44	8		21	57.8	83	976	132	1		118	6.7	8.4			
S12	19/11/2015	425	100	64	47	8		20	59.6	83	916	127	1	0.6	123	7.8	8.5	0.7095		
S12	11/01/2016	435	100	66	50	9		19	57.4	82	1008	135	1	0.3	122	6.4	8.2			
S12	19/04/2016	416	104	63	48	8	3	19	59.0	81	1000	131	1		120	7.2	7.3			
S12	08/09/2016	436	113	64	48	8		19	55.6	85	1016	129	1		128	11.8	7.8			
S12	05/12/2016	449	120	67	47	12	3	23	63.0	91	1048	130	1	0.3	147	4.6	7.8			
S12	09/03/2017	426	120	60	41	9	3	22	58.8	88	1016	121	1	0.5	124	5.1	6.5			
S12	13/06/2017	423	111	64	53	7	7	14	64.5	81		133	1		124	11.5	7.6			
S12	21/08/2017	419	91	60	47	8	3	15	54.8	82	1008	58	1	0.9	124	11.5	7.5	0.7095		
S12	20/11/2017	436	111	66	49	9		20	63.2	85		136	1	0.6	135	4.3	8.1			
S12	25/01/2018	361	88	60	43	8	6	20	55.4	69	847	132	1	0.7	137	4	7.8			
S12	19/02/2018	382	92	66	50	11	6	19	57.8	72	880	135	1	0.8	119	5	8.2			
S12	07/03/2018	337	82	54	41	7	3	16	62.2	75	929	118	1	0.7	108	5.3	8.1			
S12	03/04/2018	393	94	63	45	9	4	21	59.9	74	909	133	1	0.7	113		7.2			
S12	17/09/2018	424	100	74	57	9	10	21	48.5	76	968	145	1	0.8	115	12.8	8.6			
S12	09/04/2019	382	103	53	36	7	3	20	53.7	78	1229	108	1		118		7.1	0.7094	6.03	
S13	08/09/2010	2096	757	78	52	17	6	31	25.2	1144	3247	112			508	9	7.9			
S13	23/09/2010	2158	815	130	99	16	7	37	23.0	1206	3331	126			542	8.8	7.9			
S13	18/11/2010	2221	831	84	47	20	7	43	27.4	1310	3339	114			534	9	7.5			
S13	03/02/2011	1747	555	83	55	15	7	33	26.4	796	3239	111			438	7.9	8.3			
S13	01/03/2011	1859	658	83	46	15	6	43	27.8	939	3123	112			478	7.3	8.1			

S13	31/03/2011	1884	638	83	52	21	9	35	29.0	925	3319	114			480	8.4	7.8		
S13	02/06/2011	2071	699	87	56	17	7	36	23.9	1117	3287	115			519	8.4	7.9		
S13	04/10/2011	2083	732	91	63	16	8	33	18.6	1268	3299	113			539	8.8	7.7		
S13	09/01/2012	2009	691	87	53	18	6	40	28.4	1015	3383	113			498	7.7	7.9		
S13	15/02/2012	1896	601	87	58	16	5	34	24.2	891	3227	112			462	7.7	8.1		
S13	27/03/2012	1784	642	91	64	16	6	32	21.0	922	3203	116			486	8.4	7.9		
S13	28/06/2012	1921	642	89	58	15	10	36	22.8	874	3199	115			472	8.5	7.8		
S13	26/09/2012	2246	724	85	57	14	6	33	17.8	1273	3351	115			540	8.6	7.8		
S13	09/01/2013	1834	568	87	58	15	6	33	29.5	675	3227	114			442	8.1	7.8		
S13	16/04/2013	1747	527	87	57	14	7	35	34.7	603	3159	114			416	8.9	7.8		
S13	17/07/2013	1851	634	75	44	16		36	32.2	788	2931	112			443	9.1	7.7		
S13	18/09/2013	1851	754	69	43	17		30	23.1	1024	3283	113			499	8.4	7.7		
S13	15/12/2013	1785	539	67	35	16	6	37	30.8	904	3175	111			477	8.1	7.8		
S13	10/03/2014	1617	537	72	46	14	4	30	38.6	680	3243	117			442	8.4	8		
S13	14/06/2014	1647	581	70	46	12	5	29	37.5	652	3251	124	16		431	8.5	8	0.7094	
S13	09/10/2014	1856	623	76	57	14	5	22	29.3	937	3295	0	19		488	8.4	7.9		
S13	20/04/2015	1758	578	81	56	13	5	30	42.4	642	3343	121	15		430	8.3	7.8		
S13	13/07/2015	1763	606	76	47	14	5	33	32.9	911	3256	116	19		471	8.8	7.5		
S13	15/10/2015	1986	765	76	41	19		41	29.1	1235	3535	116	24		547	8.02	8.4		
S13	19/11/2015	1917	708	74	46	18	6	33	31.7	1143	3479	107	24	1.9	539	8.4	7.9	0.7093	
S13	11/01/2016	2002	717	78	75	19	6	3	33.0	1281	3383	118	24	1.7	532	7.8	8.0		
S13	19/04/2016	1690	590	75	56	15	6	22	35.3	821	3359	114	18	1.8	465	8.6	7.7		
S13	08/09/2016	2019	773	75	54	13	6	24	28.0	1077	3383	111	22		519	9.9	7.7		
S13	05/12/2016	2126	878	77	54	19	7	27	27.2	1327	3407	114	26	1.7	565	8.5	7.8		
S13	09/03/2017	2012	915	70	46	16	8	28	30.1	1343	3428	105	27	2.8	567	7.8	8.1		
S13	13/06/2017	1904	722	88	68	16	6	24	30.9	949		121	23	3.1	564	8.8	7.6		
S13	21/08/2017	2048	678	71	53	12	6	21	21.7	1289	3407	50	24	4.2	564	8.8	7.6	0.7093	
S13	20/11/2017	2166	876	82	58	20	3	28	23.3	1425		119	32	3.7	586	8.3	7.8		
S13	25/01/2018	1620	578	78	52	14	6	30	35.6	787	3320	110	18	3.1	453	7.8	8.1		
S13	19/02/2018	1698	553	81	60	17	6	25	35.8	775	3267	117	19	3.3	471	9.1	7.8		
S13	07/03/2018	1545	528	71	47	17	7	29	35.9	777	3326	106	17	2.8	436	9.2	8.1		
S13	03/04/2018	1722	568	87	54	16	7	39	40.9	665	3292	118	18	3.1	437		7.8		
S13	17/09/2018	2034	718	87	67	13	9	24	25.8	1109	3390	124	25	4.4	512	9.9	8.2		
S13	09/04/2019	1652	619	71	46	15	4	32	34.9	805	4043	93	17	2.0	464		7.8	0.7093	5.78
S15	23/09/2010	1734	749	157	80	22	5	90	53.5	759	3223	136			470	12.4	7.2		
S15	18/11/2010	1684	691	100	20	17	6	94	108.8	721	3175	121			454	9.5	7.9		
S15	02/02/2011	1597	638	113	26	18	6	101	9.3	759	3071	113			430	8.3	7.4		
S15	01/03/2011	1697	691	109	36	18	7	85	58.6	780	3099	116			457	8.7	7.8		
S15	31/03/2011	1647	658	109	36	18	7	85	57.3	739	3171	116			439	9.3	7.8		
S15	02/06/2011	1697	667	113	42	18	8	83	54.3	773	3359	118			461	9.9	7.8		
S15	04/10/2011	1747	699	126	52	20	6	86	51.4	833	3251	120			475	11	7.6		
S15	09/01/2012	1597	617	122	30	16	6	107	66.4	684	2943	118			420	9.3	7.9		
S15	27/03/2012	1747	749	122	42	18	7	93	56.6	832	3083	117			470	9.4	7.7		
S15	28/06/2012	1846	732	113	43	19	7	82	49.3	787	3147	118			460	10.8	7.9		
S15	26/09/2012	1772	658	117	44	19	7	85	51.1	802	3259	121			460	12.1	7.5		
S15	09/01/2013	1697	683	115	24	18	5	107	76.1	727	3163	115			445	8.9			
S15	17/07/2013	1676	740	105	33	20		84	55.7	655	3007	117			431	11	7.9		
S15	17/09/2013	1432	768	88	21	16		78	49.3	698	3179	117			450	10.7	7.7		
S15	15/12/2013	1603	598	94	16	17	5	90	66.1	733	3091	116			447	9.4	7.7		
S15	10/03/2014	1509	620	98	16	17	5	95	68.7	669	3131	120			423	9.3	7.8		
S15	14/06/2014	1558	706	97	23	17	6	86	56.9	668	3247	126	11		431	10.8	7.8	0.7096	
S15	09/10/2014	1654	650	106	35	19	4	83	54.9	694	3280	128	11		454	11	7.9		
S15	20/04/2015	1630	708	109	27	18	4	96	63.2	688	3199	124	11		436	9.7	7.8		
S15	13/07/2015	1589	666	101	29	17	4	84	53.3	721	3205	123	11		450	11.4	7.8		
S15	15/10/2015	1533	635	100	20	16		93	132.5	666	3371	123	10		453	11.1	7.8		
S15	19/11/2015	1574	653	103	18	17	5	100	59.0	742	3371	115	11	2.2	474	10.7	7.8	0.7096	
S15	11/01/2016	1593	651	104	23	18	5	95	105.7	765	3331	119	10	2.1	462	9.8	7.7		
S15	19/04/2016	1536	669	101	24	17	5	90	53.8	742	3279	118	10	2.3	453	10.5	7.6		
S15	08/09/2016	1580	705	102	35	19	4	78	53.7	700	3302	112	10	0.6	453	13.1	7.5		
S15	09/03/2017	1479	744	96	0	15	7	111	150.9	684	3134	106	9	2.7	474	9.2	7.1		
S15	13/06/2017	1709	740	114	37	19	6	90	54.5	757		127	12	3.5	470	13.5	7.6		
S15	21/08/2017	1557	589	98	27	15	5	83	51.1	758	3272	53	9	4.1	470	13.5	7.6	0.7096	
S15	25/01/2018	1514	646	110	10	17	5	117	69.0	739	3109	116	10	3.4	457	9.1	8.0		
S15	19/02/2018	1554	643	111	25	19	5	100	70.6	754	3183	119	11	3.6	449	9.7	7.9		
S15	07/03/2018	1256	547	89	6	14	6	96	64.0	697	3167	97	8	2.9	427	10	8.0		
S15	03/04/2018	1545	651	120	10	17	6	128	69.0	638	3070	119	11	3.3	450		7.7		
S15	17/09/2018	1637	678	125	46	20	9	92	55.1	717	3322	129	12	4.3	452	12.3	8.5		
S15	09/04/2019	1490	712	99	73	19	3	132	64.1	742	4216	96	9	2.4	458		7.7	0.7096	6.39
S18	08/09/2010	2046	601	96	74	9	7	25	7.4	635	3895	118			459	9.1	7.8		
S18	23/09/2010	2083	642	104		15	6	508	8.9	636	3795	121			480	9.5	7.4		
S18	18/11/2010	1934	601	86	62	8	7	28	5.9	622	3788	122			462	8.11	8		
S18	02/02/2011	1996	545	87	62	9	7	30	7.4	660	3939	122			470	7.2	7.7		
S18	01/03/2011	1984	592	91	67	9	7	28	6.9	646	3827	124			483	7.9	8.0		
S18	31/03/2011	2009	566	91	68	9	9	27	6.7	644	3871	121			472	8.6	7.7		
S18	02/06/2011	1971	560	96	50	9	7	54	2.0	798	3891	121			481	8.8	7.8		
S18	04/10/2011	1934	560	96	71	10	7	29	7.2	630	3807	121			479	8.8	7.6		
S18	09/01/2012	1959	568	91	68	8	6	26	6.4	637	3759	123			464	8	7.9		
S18	27/03/2012	2071	625	96	49	9	7	54		858	3815	123			495	8.8	7.2		
S18	28/06/2012	2096	658	91	66	10	8	29	5.8	703	3999	123			499	8.6	7.8		
S18	26/09/2012	2046	568	94	71	9	8	26	5.3	642	3859	120			470	8.9	7.7		
S18	09/01/2013	2221	675	83	57	10	6	30	5.9	785	3919	123			522	8.5	7.8		
S18	16/04/2013	2258	708	80	55	10	6	30	7.0	824	4023	122			522	8.9	7.6		
S18	17/07/2013	2101	688	70	46	9		28	10.2	690	3755	115			490	9.6	7.6		
S18	17/09/2013	2052	697	78	56	10	4	25	8.3	634	3727	118			478	8.5	7.6		
S18	15/12/2013	1837	512	68	44	8	6	29	10.1	637	3747	118			466	9.2	7.7		
S18	10/03/2014	1954	618	66	46	8	6	24	9.1	715	4075	125			501	8.5	7.6		
S18	14/06/2014	1951	683	67	45	8	5	26	10.8	691	3983	129	5		497	9	7.9	0.7097	
S18	09/10/2014	1930	564	79	65	9	5	16	12.7	616	3875	130	5		474	8.9	7.9		
S18	20/04/2015	2071	701	73	49	9	6	27	9.8	746	4179	127	5		504	9	7.7		
S18	13/07/2015	1940	593	77	53	10	5	28	12.5	648	3811	126	5		471	10.7	8.0		
S18	15/10/2015	1762	557	72	49	8		26	10.8	594	3975	117	4		462	8.4	8.2		
S18	19/11/2015	1739	531	75	51	9	7	27	12.1	604	3915	107	4	2.1	469	8.6	7.9	0.7095	
S18	11/01/2016	1832	536	80	57	9	5	27	39.8	605	3871	121	5	1.9	465	8.2	7.9		

S18	19/04/2016	1815	577	77		62	9	6	18	11.9	633	3999	119	5	2.1	478	9	7.5		
S18	08/09/2016	1881	637	77		59	11	6	21	15.1	583	3917	112	4		464	10.2	7.6		
S18	05/12/2016	1854	620	81		60	12	8	24	13.2	600	3823	118	4	1.8	463	8.4	8.1		
S18	09/03/2017	1777	634	76		59	9	8	19	12.1	589	3841	109	4	2.9	462	8.7	7.9		
S18	13/06/2017	1897	612	85		74	10	7	13	14.0	610		127	5	3.3	467	11.2	7.8		
S18	21/08/2017	1761	490	75		62	8	6	15	12.2	576	3864	52	4	4.1	467	11.2	7.6	0.7096	
S18	20/11/2017	1785	607	82		66	8	6	18	11.2	571		122	5	3.2	458	8.5	7.9		
S18	25/01/2018	1774	570	75		61	9	6	17	12.5	659	3935	115	5	3.5	506	7.7	8.2		
S18	19/02/2018	1912	578	82		67	11	5	17	12.5	675	3982	125	5	4.1	497	9.2	7.8		
S18	07/03/2018	1626	496	67		55	8	6	14	11.7	657	4010	107	4	3.0	480	9.1	8.6		
S18	03/04/2018	1988	613	79		62	10	7	20	12.4	622	4012	127	5	3.8	509		7.6		
S18	17/09/2018	1899	584	90		60	14	9	36	12.1	620	3942	130	5	4.7	458	12	7.8		
S18	09/04/2019	1804	611	69	49		8	6	23	11.6	663	5187	101	4	2.5	489		7.6		
S20	08/09/2010	2083	708	96		53	17	7	50	27.1	951	3531	114			495	11	7.7		
S20	23/09/2010	2133	749	148		100	17	7	56	32.5	979	3591	123			531	12.9	7.1		
S20	18/11/2010	2196	724	57		12	17	7	52	23.3	1098	3591	116			517	9	7.9		
S20	02/02/2011	1921	617	104		39	17	7	77	45.6	888	3447	108			475	7.3	8.1		
S20	01/03/2011	1959	691	109		51	17	8	67	36.2	910	3355	110			497	7.4	8.1		
S20	31/03/2011	1971	638	104		41	17	8	74	34.8	881	3483	110			489	8.4	7.9		
S20	02/06/2011	2108	642	109		55	16	9	62	27.9	954	3543	0			513	8.8	7.8		
S20	04/10/2011	2096	716	109		59	16	6	58	25.8	1071	3595	118			538	10.1	7.6		
S20	09/01/2012	2046	667	104		30	13	6	87	38.9	955	3439	109			496	8	7.8		
S20	27/03/2012	1896	675	100		56	16	8	51	24.4	950	3175	110			499	8.9	7.7		
S20	28/06/2012	2046	691	111		52	16	13	69	28.8	876	3563	116			505	10.8	7.7		
S20	26/09/2012	2221	691	109		59	15	7	58	22.4	1046	3615	117			519	10.7	7.8		
S20	08/01/2013	1971	642	120		41	16	6	92	56.9	755	3415	110			485	8.2	7.8		
S20	16/04/2013	1846	609	111		42	16	8	81	41.7	673	3371	109			452	8.7	7.8		
S20	17/07/2013	1912	626	86		41	15		53	32.7	731	3184	112			460	10.9	7.6		
S20	17/09/2013	2051	705	91		44	16		55	27.0	876	3431	117			502	10.1	7.6		
S20	15/12/2013	1810	538	77		28	15	7	57	35.1	894	3199	104			483	7.5	7.7		
S20	10/03/2014	1701	561	85		34	13	6	59	42.1	696	3451	112			448	7.5	7.9		
S20	14/06/2014	1841	653	94		32	17	5	73	44.1	684	3875	124	19		478	10.6	7.7	0.7094	
S20	09/10/2014	1993	609	100		49	16	5	59	38.7	766	3763	129	18		498	10.1	7.8		
S20	20/04/2015	1883	647	109		35	16	6	85	56.2	709	3655	119	17		480	8.8	7.8		
S20	13/07/2015	1729	629	85		42	12	6	49	30.6	879	3177	121	18		471	14.1	8.3		
S20	15/10/2015	2012	669	112		42	17		82	34.6	938	3843	123	19		522	9.6	7.9		
S20	19/11/2015	1910	636	97		33	17	6	74	41.7	986	3739	108	19	1.9	531	9.9	7.8	0.7093	
S20	11/01/2016	2031	672	107		48	18	6	69	44.5	1071	3655	119	19	1.7	524	9	7.8		
S20	19/04/2016	1857	644	100		41	19	6	70	42.9	854	3959	111	18	1.8	491	9	7.6		
S20	08/09/2016	1942	667	96		52	14	6	52	35.3	842	3669	113	18		506	10.9	7.6		
S20	05/12/2016	2023	730	102		50	19	8	60	34.8	1019	3580	112	18	1.5	527	9.9	7.9		
S20	09/03/2017	1958	767	93		33	14	8	69	41.4	1081	3529	99	18	2.8	530	834	8.0		
S20	12/06/2017	1915	730	103		48	14	7	64	42.5	944		115	19	2.9	539	11.1	7.5		
S20	21/08/2017	2014	608	95		50	13	6	53	30.1	1038	3651	53	18	4.1	539	11.1	7.5	0.7094	
S20	20/11/2017	2113	769	112		57	16	6	65	32.5	1133		122	22	3.3	560	9.8	7.6		
S20	25/01/2018	1738	619	101		39	15	6	71	43.5	837	3339	109	18	3.4	521	7.1	7.9		
S20	19/02/2018	1711	590	100		44	15	6	65	42.2	816	3328	108	18	3.2	470	7.8	8.1		
S20	07/03/2018	1534	533	88		30	12	7	67	42.9	801	3311	98	15	2.6	444	8.3	8.2		
S20	03/04/2018	1723	582	105		30	16	7	88	44.6	680	3307	111	18	2.9	460		7.7		
S20	17/09/2018	1996	647	121		69	18	9	61	34.6	852	3692	127	21	4.2	496	12.2	8.1		
S20	09/04/2019	1651	626	85		60	12	6	63	34.5	826	4533	86	15	1.9	469		7.7	0.7094	6.38
S21	08/09/2010	1921	667	78		37	13	6	48	36.9	949	3347	114			482	13.4	7.9		
S21	23/09/2010	2021	708	157		110	13	7	54	37.4	987	3323	128			505	12.3	7.4		
S21	18/11/2010	2096	699	92		45	13	7	55	57.2	967	3503	116			515	9.3	8.1		
S21	02/02/2011	1796	576	96		36	12	7	69	43.7	857	3187	109			448	6.6	8.2		
S21	01/03/2011	1834	625	91		41	11	8	59	37.4	902	3107	108			472	7.1	8.1		
S21	31/03/2011	1859	617	83		34	12	9	56	47.1	896	3203	107			467	8.03	8.6		
S21	02/06/2011	1934	650	100		55	12	10	53	30.7	937	3343	112			496	10.9	7.9		
S21	04/10/2011	2271	691	100		49	13	8	59	27.4	1011	2219	117			516	12.2	7.8		
S21	09/01/2012	1996	650	104		40	10	7	75	64.4	945	3319	111			489	7.9	8.0		
S21	27/03/2012	1896	683	104		52	12	9	61	30.9	941	3131	108			484	9.1	7.9		
S21	28/06/2012	1971	658	104		57	12	7	56	24.0	856		115			483	12.3	7.7		
S21	26/09/2012	2009	617	102		52	11	6	59	25.3	963	3527	118			498	12.8	7.9		
S21	09/01/2013	1896	411	102		46	10	7	66	41.9	772	3203	105			463	7.6	7.8		
S21	16/04/2013	1784	560	115		55	12	7	70	38.9	695	3123	104			357	11.6	7.9		
S21	17/07/2013	1898	647	89		43	11	5	53	30.9	717	3183	112			448	14.5	8.2		
S21	17/09/2013	1928	701	88		45	10		50	26.3	830	3351	116			485	11.9	7.9		
S21	15/12/2013	1807	538	81		31	11	6	58	39.4	847	3255	109			476	8.3	7.9		
S21	10/03/2014	1730	571	85		36	10	7	57	58.6	714	3371	112			445	7.7	8.1		
S21	14/06/2014	1710	613	81		44	9	6	43	36.2	675	3375	122	18		441	12.4	7.9	0.7094	
S21	09/10/2014	1890	591	90		48	11	5	49	30.4	787	3439	127	18		477	11.9	8.1		
S21	20/04/2015	1782	613	95		44	12	4	60	42.7	688	3359	116	17		438	9.6	7.9		
S21	13/07/2015	1845	606	101		40	13	4	71	34.9	811	3459	122	18		508	12.5	7.8		
S21	15/10/2015	1863	625	123		39	11	5	98	37.5	893	3727	118	18		508	11.3	8.1		
S21	19/11/2015	1818	601	90		33	11	6	67	36.1	937	3603	107	18	1.7	509	10.5	8.0	0.7093	
S21	11/01/2016	1919	643	97		43	12	6	63	46.2	992	3507	117	19	1.6	500	8.8	7.9		
S21	19/04/2016	1729	603	92		42	11	6	59	38.8	836	3439	107	17	1.6	472	9.9	7.9		
S21	08/09/2016	1962	666	96		52	12	6	51	33.0	819	3634	119	19		493	14.1	7.8		
S21	05/12/2016	1923	690	101		46	13	8	63	32.4	918	3492	112	18	1.4	502	9.3	7.9		
S21	09/03/2017	1847	743	93		26	8	8	78	45.9	965	3321	98	17	2.5	494	8	8.1		
S21	13/06/2017	1896	703	113		54	12	8	68	35.4	901		117	19	2.8	520	14.5	4.7		
S21	21/08/2017	1917	589	96		46	10	6	58	28.8	961	3524	52	17	4.2	520	14.5	4.7	0.7094	
S21	20/11/2017	1961	702	103		50	10	6	62	28.2	1008		119	20	3.2	544	9.7	7.6		
S21	25/01/2018	1797	617	119		30	10	6	104	51.9	855	3350	108	18	3.3	471	7.4	8.1		
S21	19/02/2018	1734	579	113		49	12	6	74	42.1	829	3288	109	17	3.0	468	8	8.2		
S21	07/03/2018	1525	519	95		15	8	7	94	44.0	814	3303	95	15	2.6	446	9.5	8.3		
S21	03/04/2018	1764	582	110		28	10	8	96	60.3	708	3282	109	17	3.1	466		7.9		
S21	17/09/2018	1912	615	114		67	11	10	55	22.9	838	3559	132	20	4.1	494	16.3	7.7		
S21	09/04/2019	1650	643	92		66	10	7	93	30.3	851	4503	88	15	1.9	484		7.9	0.7094	6.54
Rain	19/05/2016	25	6	26			24		28	24.6	20		1	0	0	22	11.4	7.1		
Rain	28/05/2016	8	0	5			4		5	8.1	6	72	0	0	0	23		5.5		
Rain	31/05/2016	12	2	8			5		8	9.6	6	72	0	0	0	25		6		
Rain	28/05/2016	9	2	21			14		20	8.2	9	72	0	0	0	29		5.8		
Rain	31/05/2016	15	2	5			5		5	11.9	6	72	0	0	0	25		5.9		
Rain	19/05/2016	2219	1953	212			28		11	26.9	26		126	5	3.5	45	10.4	7.4		
Rain	28/05/2016	7	3	3			9		4	7.2	4	72	0	0	0	29		5.8		
Rain	31/05/2016	12	2	4			4		3	9.3	4	72	0	0	0	25		5.9		

Appendix C: Identifying chloride inputs (atmospheric, anthropogenic, salts): X *vs.* Cl graphs

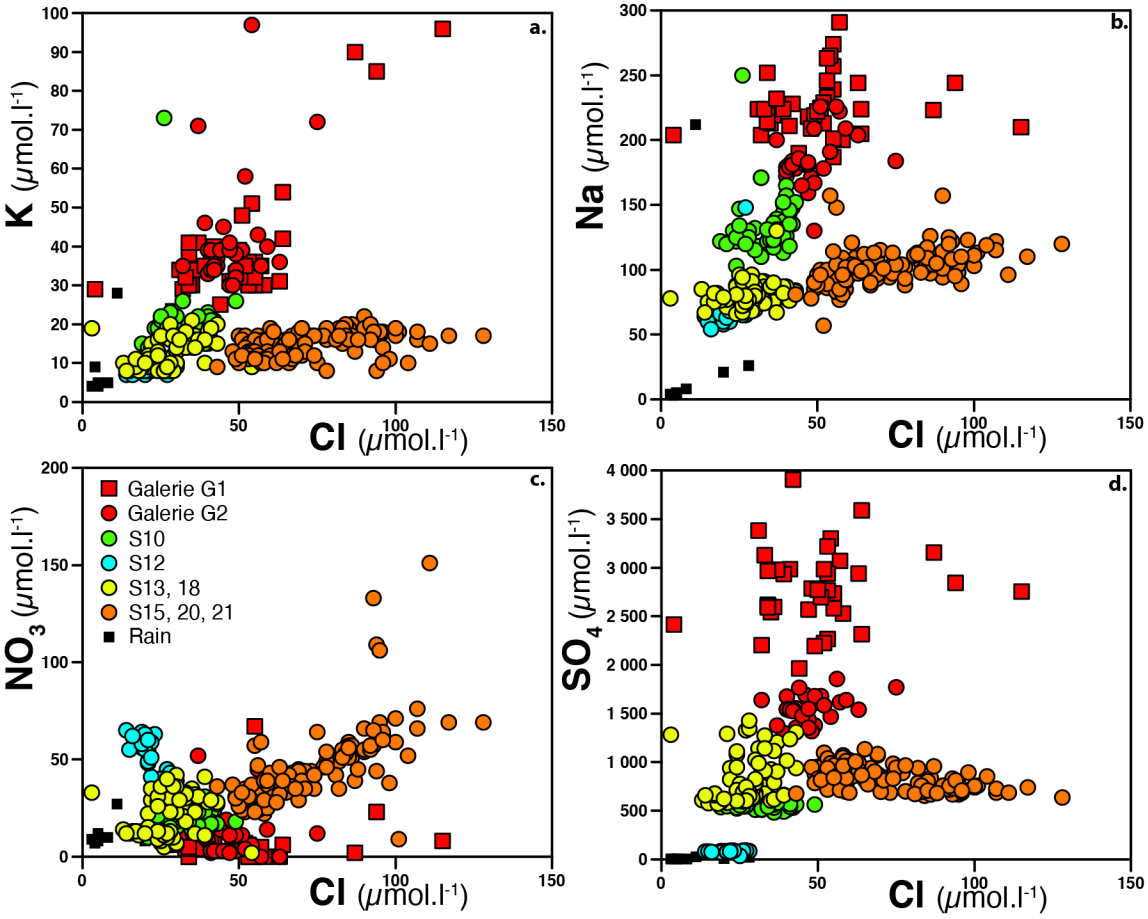

Figure C1: Elemental concentrations (X) of the different groups of water outflow from the Séchilienne massif as a function of Cl concentrations; a. K *vs*. Cl, b. Na *vs*. Cl, c. NO_3 *vs*. Cl, d. SO_4 *vs*. Cl.

Appendix D: Solving the mixing equations

Model set-up and Sr fractions

Given the discussion of section 5.1 and the geochemical mixing diagrams presented in Fig. 4, three end members can be identified to release solutes to the springs of the Séchilienne area: silicate weathering (*sil*), carbonate weathering (*carb*; including both calcite and dolomite), and gypsum dissolution (*gyps*). The contribution of each of these processes to the solute load of the springs can be estimated using a combination of mixing equations, provided that geochemical tracers that are conservative during mixing of compositionally different waters can be identified, and that the composition of the end members can be assessed. He we use two such tracers: $^{87}Sr/^{86}Sr$ and Na/Sr ratios (all corrected from rain and anthropogenic inputs, as explained in the main text). Indeed, the $^{87}Sr/^{86}Sr$ ratio is not affected by isotope fractionation due to the way data are reduced after measurements by mass spectrometry; and both Na and Sr are soluble elements unlikely to be scavenged into secondary solids such as clays in most contexts. Two mixing equations, each based on one of the two tracers, can be combined with a third summation equation to solve for X_{sil}^{Sr}, X_{carb}^{Sr}, and X_{gyps}^{Sr}, the relative contribution of the three identified end member to dissolved Sr:

$$\left(\frac{^{87}Sr}{^{86}Sr}\right)_{spring} = X_{sil}^{Sr}\left(\frac{^{87}Sr}{^{86}Sr}\right)_{sil} + X_{carb}^{Sr}\left(\frac{^{87}Sr}{^{86}Sr}\right)_{carb} + X_{gyps}^{Sr}\left(\frac{^{87}Sr}{^{86}Sr}\right)_{gyps} \quad \text{(D1)}$$

$$\left(\frac{Na}{Sr}\right)_{spring} = X_{sil}^{Sr}\left(\frac{Na}{Sr}\right)_{sil} + X_{carb}^{Sr}\left(\frac{Na}{Sr}\right)_{carb} + X_{gyps}^{Sr}\left(\frac{Na}{Sr}\right)_{gyps} = X_{sil}^{Sr}\left(\frac{Na}{Sr}\right)_{sil} \quad \text{(D2)}$$

$$X_{sil}^{Sr} + X_{carb}^{Sr} + X_{gyps}^{Sr} = 1 \quad \text{(D3)}$$

The simplification of eq. (D2) is made possible by the fact that the gypsum and carbonate end members can be assumed to be devoid of Na. This assumption is supported by the positions of the different springs in a Na/Sr *vs*. $^{87}Sr/^{86}Sr$, which indicates that the low-$^{87}Sr/^{86}Sr$ component, encompassing both carbonate and gypsum weathering of the springs has a negligible Na content, with the exception of spring S12 which we do not treat quantitatively here (Fig. D1).

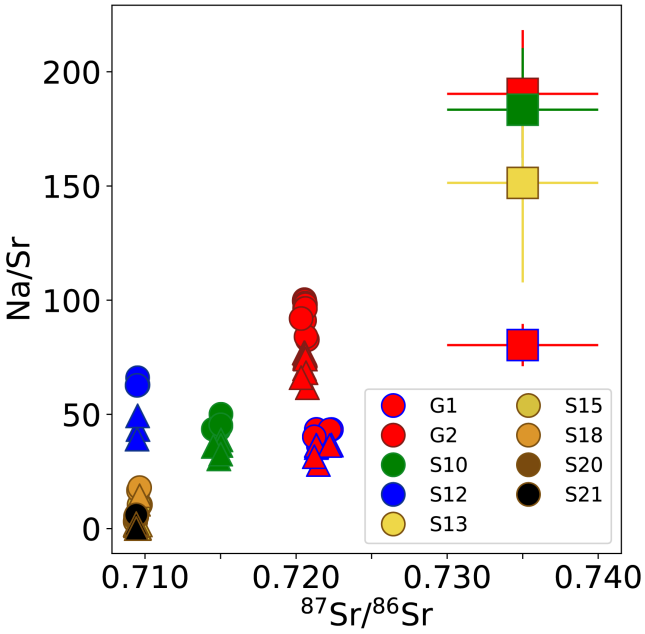

Figure D1: Na/Sr vs $^{87}Sr/^{86}Sr$ for the different groups of water outflows (circles represent spring water composition corrected for rain and anthropogenic inputs (eq. 1); triangles represent spring water composition corrected for gypsum dissolution (eq. D5)) sampled in the Séchilienne massif. The inferred composition of the silicate end member for each group is shown as squares

The composition of the end members was constrained as follows (values also provided in Table D1):

- for each spring, $\left(\frac{^{87}Sr}{^{86}Sr}\right)_{spring}$ and $\left(\frac{Na}{Sr}\right)_{spring}$ were taken to be equal to the average ratios (corrected from rain inputs for Na/Sr) over all measurements available for the spring (note that one outlier were dismissed for each of the two springs G1 and G2);
- $\left(\frac{^{87}Sr}{^{86}Sr}\right)_{carb}$ was taken between 0.7090 and 0.7095 or 0.7095 and 0.7105, depending on whether the carbonate end member was assumed to be of calcitic or dolomitic nature. These ranges were constrained based on our own geochemical analyses of rock samples (Tab. A1). Note that the first range is consistent with what is known of early Jurassic seawater Sr isotope composition (MacArthur and Howarth, 2004). $\left(\frac{^{87}Sr}{^{86}Sr}\right)_{gyp}$ was taken between 0.7075 and 0.7080, which is typical of Triassic seawater, and in agreement with values reported for Alpine gyspum by previous studies (Kloppmann et al., 2017).
- $\left(\frac{^{87}Sr}{^{86}Sr}\right)_{sil}$ was assumed to be equal to the highest measured Sr isotope ratio throughout the local bedrock samples ("micaschist", 0.735 ± 0.005; Tab. A1).

- The $\left(\frac{Na}{Sr}\right)_{sil}$ ratio was determined for the springs the most affected by silicate weathering (G1, G2, and S10) by extrapolating Na/Sr *vs.* $^{87}Sr/^{86}Sr$ relationships (Fig. D1) to a $^{87}Sr/^{86}Sr$ equal to that of the silicate end member (0.735, see above). Linear extrapolation in this diagram is made possible by the fact that Sr concentration is present on the denominator of both ratios plotted. For each spring, a set of lines was determined, each passing through (1) the carbonate end member ($^{87}Sr/^{86}Sr$ = 0.7090-0.7105 and Na/Sr = 0); (2) one of the samples collected for this spring. After extrapolation of these lines to $^{87}Sr/^{86}Sr$ = 0.735 (our central estimate of $\left(\frac{^{87}Sr}{^{86}Sr}\right)_{sil}$, see above), a collection of estimated $\left(\frac{Na}{Sr}\right)_{sil}$ ratios was therefore obtained for each spring, and the average and standard deviation of these ratios was used as spring-specific central estimate and associated uncertainty of the $\left(\frac{Na}{Sr}\right)_{sil}$ ratio, respectively. Note that following the discussion on Cl sources in section 5.1.1 of the main text, for each of the springs G1, G2, and S10 two estimations of $\left(\frac{Na}{Sr}\right)_{sil}$ were performed: one based on Na concentrations corrected from rain inputs only following eq. (1) ($[Na^*]$), and the other based on Na concentrations from which an amount equivalent to total Cl concentration was subtracted (hence assuming that the entirety of Cl^- release to the springs was associated with Na^+ release). The average between these two estimates was then used for further calculations. The obtained $\left(\frac{Na}{Sr}\right)_{sil}$ values range from 80 ± 9 to 205 ± 30 mol/mol, lower than those classically estimated for silicates (e.g. Négrel et al., 1993) but consistently with the fact that the parent rock at Séchilienne is a micaschist, that is a sedimentary rock that has lost soluble elements such as Na in previous weathering episodes compared to igneous silicates. For the springs the least affected by silicate weathering (S12, S13, S15, S18, S20, and S21), as such extrapolation would lack precision, we simply took the average and standard deviation of the $\left(\frac{Na}{Sr}\right)_{sil}$ ratios estimated for springs G1, G2, and S10 (yielding 162 ± 40). This strong assumption does not bear consequence on our overall evaluation as these former springs are not significantly affected by silicate weathering anyway.

The uncertainty on the different input parameters was propagated to the output variables (X^{Sr}_{sil}, X^{Sr}_{carb}, and X^{Sr}_{gyp}) using a Monte Carlo method based on 10,000 iterations. For this, at each of the 10,000 iterations a value for each input parameter (end member composition) was randomly picked following either (a) a normal distribution with mean equal and standard deviations to the estimate and uncertainty provided above, respectively, for parameters $\left(\frac{^{87}Sr}{^{86}Sr}\right)_{sil}$ and $\left(\frac{Na}{Sr}\right)_{sil}$; and (b) a uniform distribution bounded by the lowest and highest estimates provided above for parameters $\left(\frac{^{87}Sr}{^{86}Sr}\right)_{carb}$ and $\left(\frac{^{87}Sr}{^{86}Sr}\right)_{gyp}$. The choice of a uniform distribution to reflect uncertainty on the latter parameters is justified by the fact that it is highly unlikely that Sr isotope ratios

of marine carbonates lie outside of the prescribed range, which is unavoidable to occur for a significant number of random draws if one were to be used a normal distribution with a reasonable standard deviation instead. Note that, generally speaking, the composition of the springs was not considered as a random variable here and was simply fixed for all iterations. However, in order to account for uncertainty on the Cl^- source to the spring waters (main text section 5.1.1), for each spring and for each simulation we randomly drew values of $\left(\frac{Na}{Sr}\right)_{spring}$ following a uniform distribution bounded by Na concentrations given by eq. (1) ([Na^*]) on the one hand, and by Na concentrations from which an amount equivalent to total Cl^- concentration was subtracted (hence assuming that the entirety of Cl^- release to the springs was associated with Na^+ release) on the other hand. Finally, Monte Carlo runs yielding X_{sil}^{Sr}, X_{carb}^{Sr}, and X_{gyp}^{Sr} values outside of the range [0,1] were dismissed (the number of "valid" iterations is reported in Table D2).

The resulting distributions of output X_{sil}^{i} values are reported in Table D2 as their 16th, 50th (median), and 84th percentile. Median estimates of X_{sil}^{Sr} range from 0.06 and 0,08 (springs S15 and S18) to 0.42 and 0.47 (springs G2 and G1, respectively); median estimates of X_{carb}^{Sr} range from 0.04 and 0.07 (springs S15 and S18) to 0.36 (spring S10); and median estimates of X_{gyp}^{Sr} range from 0.25 and 0.29 for G1 and G2 to 0,85-0,90 for S18-S15. S10 median estimate is 0.42. Obtained values differed weakly depending on whether a calcitic or a dolomitic composition was used for $\left(\frac{^{87}Sr}{^{86}Sr}\right)_{carb}$ (Tab. D2).

Gypsum contribution

The contribution of each of these end members to the load of the dissolved major species SO_4, Ca, and Mg is necessary to evaluate the impact of the different weathering processes to the CO_2 budget of the Séchilienne area (Torres et al., 2016). In principle, these end member contributions to major dissolved species can be calculated from the corresponding contributions to dissolved Sr following:

$$X_i^E = X_i^{Sr} \left(\frac{E}{Sr}\right)_i / \left(\frac{E}{Sr}\right)_{spring} \quad \text{(D4)}$$

with i = *sil, carb,* or *gyp*, and E = SO_4 and Mg (corrected for rain and anthropogenic inputs). As explained below, because secondary carbonate formation might occur at Séchilienne and thus lead to the preferential scavenging of Ca from waters, eq. (D4) cannot be used indifferently for E = Ca or for i = *carb*. We return to the estimation of X_i^{Ca} values later. Regardless of this issue, eq. (D4) can first be used to calculate X_{gyp}^{Mg} and X_{gyp}^{SO4} provided that the $\left(\frac{E}{Sr}\right)_{gyp}$ ratios are known. The E/Sr ratios of the gypsum end member were determined using the E/SO_4 *vs.* (Ca+Mg)/SO_4 relationships described by the springs the least affected by silicate weathering (as identified by their low $^{87}Sr/^{86}Sr$ ratios, *i.e.* springs S13, S15, S18, S20, and S21; Fig. D2).

Indeed, for these springs where sulfate can be assumed to be entirely derived from gypsum and not from sulfide dissolution, at (Ca+Mg)/SO_4 of 1 mol/mol, the entirety of the dissolved load can be assumed to be derived from gypsum dissolution alone (Ca and Mg being the two major cations likely to be released by gypsum dissolution).

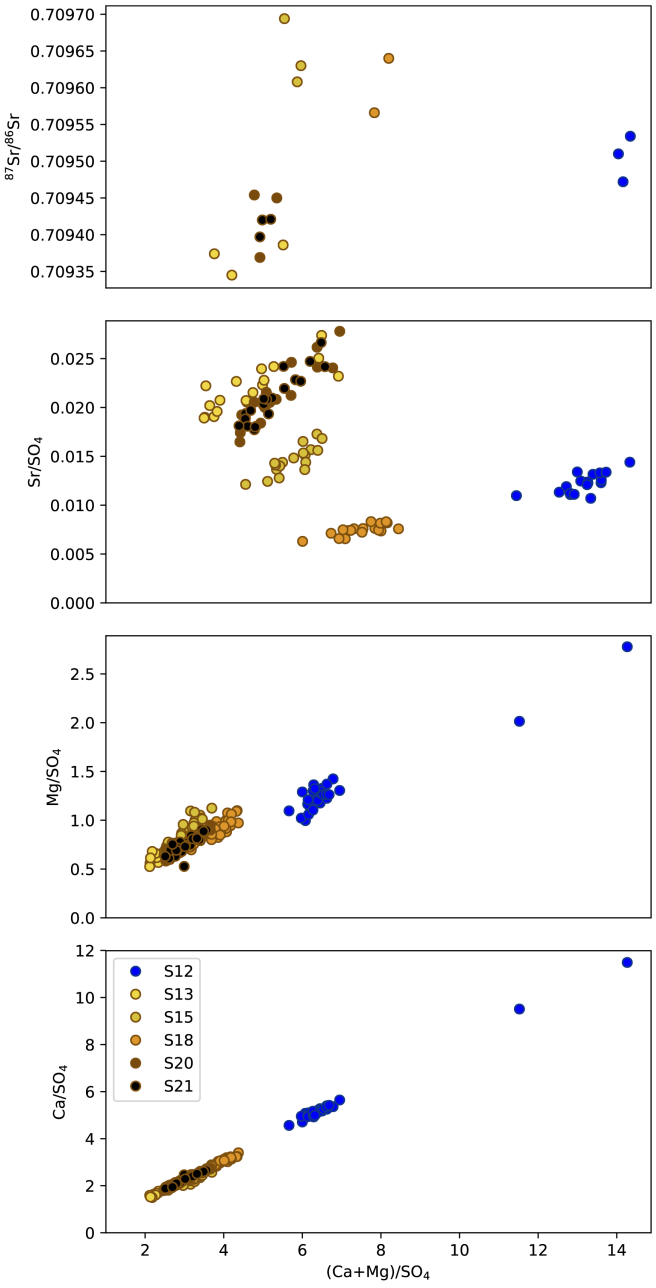

800

Figure D2: Mixing diagrams of the $^{87}Sr/^{86}Sr$ ratio and the E/SO_4 (with E = Sr, Mg, Ca, and Na) molar ratio *vs*. the (Ca+Mg)/SO_4 molar ratios, used to determine the E/Sr molar ratios of the gypsum end member.

Linear extrapolation in Fig. D2 is made possible by the fact that SO_4 concentration is present on the denominator of both ratios plotted. Taking the average values obtained through extrapolation of the observed trends to (Ca+Mg)/SO_4 = 1 mol/mol suggests 0.31 ± 0.04 and 9.2 10^{-3} ± 4.4 10^{-3} mol/mol for the Mg/SO_4 and Sr/SO_4 ratios of the gypsum end members. From these two SO_4-normalized ratios, Sr-normalized ratios can be obtained to calculate X_{gyp}^{Mg} and X_{gyp}^{SO4} using eq. (D4). Obtained modal values of X_{gyp}^{Mg} are lower than 0.03 for springs G1-G2-S10, and around 0.20-0.40 for the other springs. Modal values of X_{gyp}^{SO4} are lower than 0.05 for springs G1-G2-S10, and range between 0.5 and 0.75 for the other springs

As the SO_4/Sr ratio of the carbonate end member was assumed to be equal to 0, consistently with the mixing diagrams of Fig. 4, X_{sil}^{SO4} could be calculated as 1 - X_{gyp}^{SO4} (eq. D3). Consequently, a value for the SO4/Sr ratio of the silicate end member could be estimated using the SO4/Sr mixing equation (similar to eqs. (D1-D2)):

$$\left(\frac{SO_4}{Sr}\right)_{spring} = X_{sil}^{Sr}\left(\frac{SO_4}{Sr}\right)_{sil} + X_{gyp}^{Sr}\left(\frac{SO_4}{Sr}\right)_{gyp} \quad \text{(D5)}$$

To solve eq. (D5), the average and standard deviation of all measurements of $\left(\frac{SO_4}{Sr}\right)_{spring}$ were used, thereby yielding a spring-specific value for $\left(\frac{SO_4}{Sr}\right)_{sil}$. This estimate was performed during the Monte Carlo iterations described above, yielding modal values ranging from 666 (spring S20) to 1845 mol/mol (spring G2).

Secondary carbonate formation and carbonate contribution

The precipitation of secondary carbonates is known to preferentially scavenge dissolved Ca^{2+} at the expense of other alkali-earth ions Mg^{2+} and Sr^{2+} (Bickle et al., 2015). As a consequence, Ca does not necessarily behave conservatively in carbonate-rich settings such as Séchilienne, where secondary carbonate precipitation is likely to occur. We quantify the role of secondary carbonate formation using the method proposed by Bickle et al. (2015), which is based on the comparison between the chemical composition of springs and that predicted from conservative mixing between the rock dissolution end members. In a first set of attempts we assumed that secondary carbonate precipitation at Séchilienne was affecting only waters and solutes derived from two of the three rock dissolution end members (*i.e.* silicate and carbonate rocks, silicate rocks and gypsum, or carbonate rocks and gypsum). The Rayleigh-type equation proposed by Bickle et al. (2015) links dissolved E/Ca ratios to the extent of Ca scavenging by the formation of secondary carbonates:

$$\left(\frac{E}{Ca}\right)_p = \left(\frac{E}{Ca}\right)_0 \gamma^{K_d^E - 1} \quad \text{(D6)}$$

where $\left(\frac{E}{Ca}\right)_0$ is the "initial" E/Ca ratios of waters (*i.e.*, before secondary carbonate precipitation has taken place) with E = Sr, Mg, or Na, $\left(\frac{E}{Ca}\right)_p$ is the E/Ca ratios of waters after secondary carbonate precipitation has taken place, γ is the amount of "initial" Ca left in solution after secondary carbonate precipitation has taken place, and K_d^E is the partition coefficient of element E into calcite, defined as the ratio between the E/Ca ratio into the precipitating calcite and that in water. During our Monte Carlo simulations, we randomly drew values for K_d^{Sr} and K_d^{Mg} following a uniform distribution between 0.02 and 0.10, and considered that K_d^{Na} = 0. As explained by Bickle et al. (2015), results in terms of source apportionment do not depend strongly on the exact values chosen for the K_d^E parameters. In a scenario where only two rock dissolution end members contribute Ca involved into secondary carbonate precipitation, γ is the solution of (Bickle et al., 2015):

$$\left(\frac{E}{Ca}\right)_p \gamma^{1-K_d^E} = A + B\gamma\left(\frac{Na}{Ca}\right)_p \quad \text{(D7)}$$

where A and B are the intercept and slope, respectively, of the binary mixing line between the two rock dissolution end members in the E/Ca-Na/Ca space, with E = Mg or Sr. Note that eq. (D7) is valid because Na is not significantly incorporated into secondary carbonates (in other words, K_d^{Na} is assumed to be equal to 0). In Fig. D3, we show the results of such a scenario where gypsum-derived solutes are thought to be added to waters derived from combined silicate and carbonate weathering only after these two combined end members have been affected by secondary carbonate precipitation Such a scenario is compatible with the formation of waters dominated by silicate and carbonate weathering "locally" at the Séchilienne site, to which solutes derived from gypsum dissolution are admixed after their transport from a distal recharge location, for example through fluid circulation along the Sabot fault. In this scenario the $\left(\frac{E}{Ca}\right)_p$ and $\left(\frac{Na}{Ca}\right)_p$ ratios in eq. (D7) are those of the spring waters once corrected from gypsum inputs. However, this approach fails to account for the observed spring data as the γ values retrieved from the Sr/Ca-Na/Ca and Mg/Ca-Na/Ca differ greatly (Fig. 3D), regardless of whether the carbonate end member is assumed to be of calcitic or dolomitic nature, or any combination thereof. Similar unsatisfactory results were obtained from different assumptions regarding the two rock dissolution end members contributing Ca involved in secondary carbonate precipitation.

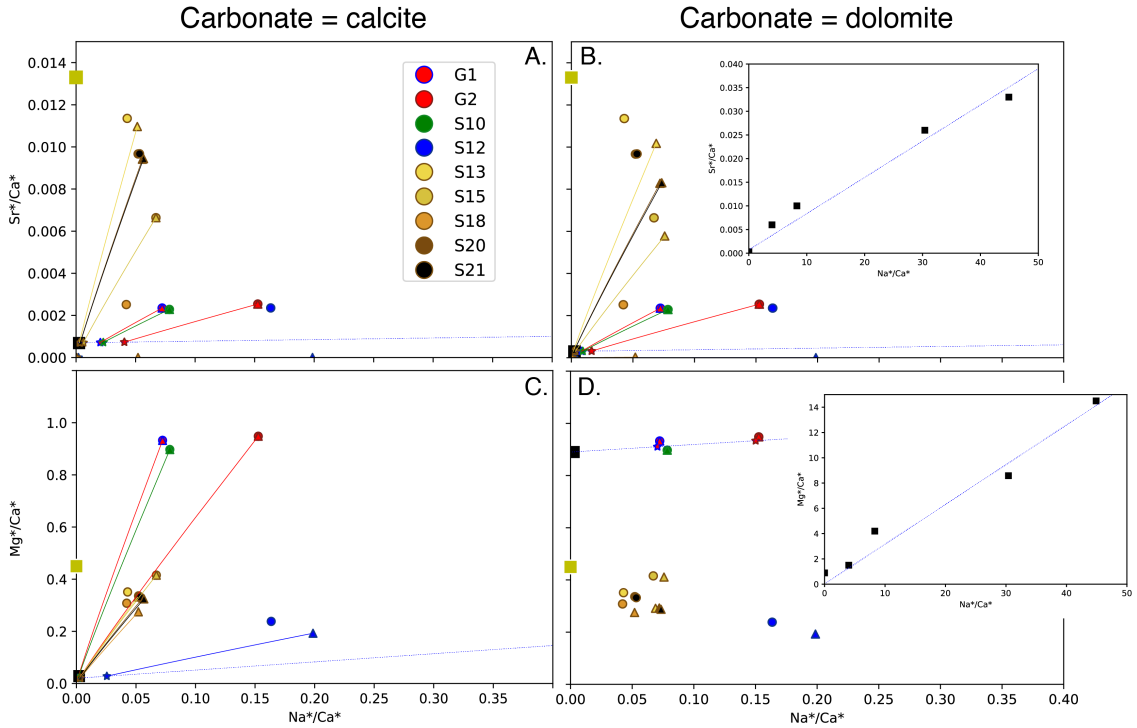

Figure D3: Quantification of the extent of secondary carbonate precipitation on dissolved Ca scavenging, assuming that secondary carbonate precipitation affects only waters derived from the combined weathering of silicate and carbonate rocks, and that gypsum-derived waters are added once secondary carbonate precipitation has occurred. Circles represent spring water composition corrected for rain and anthropogenic inputs (eq. 1); triangles represent spring water composition corrected for gypsum dissolution (eq. D5, which under this assumption can be used with X = Ca and $i = gyps$, since gypsum-derived solutes are assumed here to be simply added in a conservative mixing process); and stars represent spring water composition corrected for secondary carbonate precipitation (hence resulting from conservative mixing between the two rock dissolution end members) using the method of Bickle et al. (2015) (eq. D7). The colored lines link the two latter spring compositions and thus correspond to the path followed by the water composition upon dissolved Ca scavenging, such that the length of the line reflects the extent of Ca scavenging as quantified by γ (eqs. D6 and D7). The large squares correspond to the composition of the gypsum (yellow) and carbonate (black) dissolution end members. The blue dotted line reflects the binary mixing between waters derived from carbonate dissolution and waters derived from silicate dissolution, as constrained by our geochemical analyses of rocks samples (Tab. A1), on which spring composition must lie after correction from the effect of secondary carbonate precipitation. Panels A-B and C-D display the Sr/Ca-Na/Ca and Mg/Ca-Na/Ca sub-compositional spaces, respectively. Panels A-C and B-D show the results obtained if the carbonate end member is assumed to be of calcitic and dolomitic composition, respectively (note in particular the higher Mg/Ca ratio of the carbonate end member in panels D, and the corresponding absence of lines linking triangles and stars, meaning that no Ca scavenging needs to take place through secondary carbonate precipitation to explain the data of springs G1, G2, and S10; and that the data of other springs cannot be explained by this scenario (2) if the composition of the carbonate end member is dolomitic). Inset in panels C and D show the same sub-compositional spaces but with a larger range of ratios, allowing for displaying the composition of rock samples Tab. A1 as black squares. In these insets, the high-Na/Ca data points correspond to silicate samples. To obtain these results, all spring Cl- was assumed to be associated to Na+ (main text section 5.1.1), and K_d^{Sr} was assumed to be equal to K_d^{Mg} with a value of 0.06 was used. Modification of these assumptions

would not change the general principles that are exemplified by this figure; and uncertainty on these aspects is taken into account in our Monte Carlo simulations.

As a consequence, we assume that secondary carbonate precipitation affects solutes derived from the three weathering sources (carbonate, silicate, and gypsum dissolution) after they are mixed. Such scenario probably does not reflect perfectly the reality of the interplay between water mixing and chemical reactions in the subsurface at Séchilienne, but account for the fact that solutes from the three rock dissolution end members are mixed in a complex porous media, while keeping this problem mathematically tractable.

In such scenario, the contribution of neither rock end member can be corrected before secondary carbonate formation is taken into account. To that effect, the method of Bickle et al. (2015) can be extended to its use in the higher-dimensional Sr/Ca-Mg/Ca-Na/Ca space. In such space, the mixing array between carbonate, silicate, and gypsum dissolution is a plane, to which the composition of the springs can be "brought back" as in eq. (D7):

$$\alpha\gamma^{1-K_d^{Mg}}\left(\frac{Mg}{Ca}\right)_p + \beta\gamma^{1-K_d^{Sr}}\left(\frac{Sr}{Ca}\right)_p + \varepsilon\gamma\left(\frac{Na}{Ca}\right)_p = \delta \qquad \text{(D8)}$$

where α, β, ε, and δ are the parameters of the Cartesian equation of the mixing plane in the Sr/Ca-Mg/Ca-Na/Ca space. The ternary mixing relationships in the Sr/Ca-Mg/Na-Na/Ca space were constrained for Séchilienne using our own geochemical analyses of rock samples (Tab. A1) and are shown in Fig. D4. These relationships thus allow us to solve numerically eq. (D8) for γ for each spring. We performed this calculation for various values of the relative contribution of dolomite dissolution to the overall Ca released to solution by carbonate weathering (from 0% to 100% dolomite, the rest being delivered by calcite dissolution; the two extreme cases are illustrated in Fig. D4), and constrained the chemical ratios of each of the carbonate components by our own geochemical analyses of rock samples (Tab. A1). We observed as a general trend that increasing the relative contribution of the dolomite end member beyond 20% resulted in an extent of alkalinity consumption through carbonate precipitation that was too large compared to alkalinity production to be sustainable. As a consequence, we fixed the relative contribution of dolomite to the overall Ca release by carbonate dissolution to 10% in the following calculations.

With these constraints, across the Monte Carlo simulations median estimates of γ are 0.38 for G1, 0,39 for G2, 0,40 for S10 and 0,90 for S15. For the other springs, γ was set to 1 as no Ca scavenging was required to explain the data - in other words, for these springs the hydrochemical data approximately lie on the mixing plane between the three rock dissolution end members in the Sr/Ca-Mg/Ca-Na/Ca compositional space.

The γ value found for each spring can then be used to provide a value for the dissolved Sr/Ca, Mg/Ca, and Na/Ca ratios before the carbonate precipitation has taken place $\left(\frac{E}{Ca}\right)_0$ using eq. (D6) with the measured spring ratios as values for $\left(\frac{E}{Ca}\right)_p$. Then, X_{carb}^{Ca} and X_{carb}^{Mg} can be estimated from eq. (D4) for $i = carb$, but using the above-inferred Ca/Sr and Mg/Sr ratios (calculated from Sr/Ca and Mg/Ca ratios) before secondary carbonate precipitation as values of $\left(\frac{E}{Sr}\right)_{spring}$. X_{sil}^{Ca} and X_{sil}^{Mg} are then

determined by difference using eq. (D3) with Ca or Mg instead of Na, Finally, knowing the composition of the carbonate end member (as constrained by our geochemical analyses on rock samples; Tab. A1), values for $\left(\frac{Ca}{Sr}\right)_{sil}$ and $\left(\frac{Mg}{Sr}\right)_{sil}$ can be determined using eq. (D2) with Ca and Mg instead of Na, respectively, as in scenario (2).

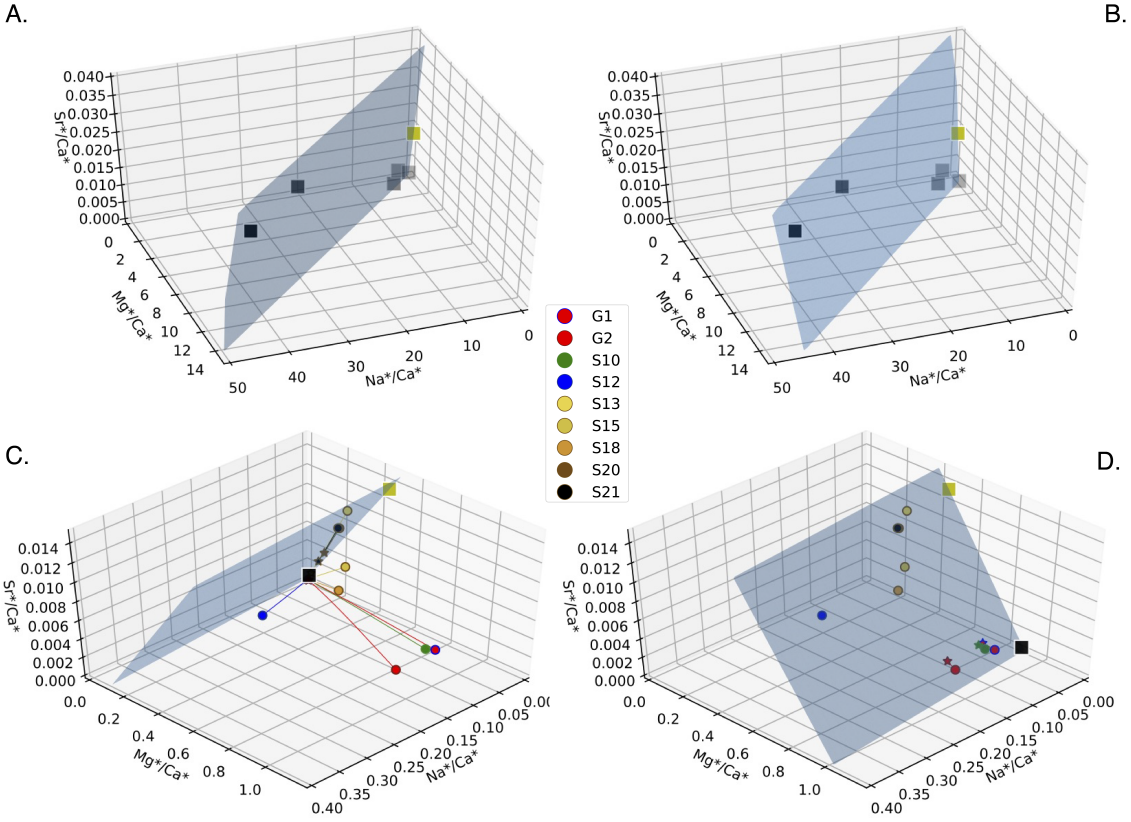

Figure D4: Quantification of the extent of secondary carbonate precipitation on dissolved Ca scavenging, assuming that secondary carbonate precipitation affects waters once they have been mixed from the three rock dissolution end members (silicate, carbonate, and evaporites). Circles represent spring water composition corrected for rain and anthropogenic inputs (eq. 1) and stars represent spring water composition corrected for secondary carbonate precipitation (hence resulting from conservative mixing only) using the method of Bickle et al. (2015), but here extended to the three dimensional Sr/Ca-Mg/Ca-Na/Ca space (eq. D8). The blue plane reflects the ternary mixing between waters derived from carbonate, silicate and evaporite dissolution, as constrained by our geochemical analyses of rocks samples (Tab. A1), on which spring composition must lie after correction from the effect of secondary carbonate precipitation. The colored lines link the two water compositions (before and after secondary carbonate precipitation) and thus correspond to the path followed by the water composition upon dissolved Ca scavenging, such that the length of the line reflects the extent of Ca scavenging as quantified by γ (eqs. D6 and D8). The large squares correspond to the composition of the gypsum (yellow) and carbonate (black) dissolution end members. Panels A-B and C-D show the same results but with different scales. In particular, water compositions are made visible only in panels C and D which are "zoom-in" on the low-Sr/Ca, low-Mg/Ca, and low-Na/Ca part of the domains represented in panels A and B. Panels A-C and B-D correspond to results obtained if the carbonate end member is assumed to be calcitic and dolomitic, respectively. Note in particular the higher Mg/Ca ratio of the

carbonate end member in panels B and D, and the resulting "tilting" of the mixing plane (and the corresponding absence of lines linking triangles and stars, meaning that no Ca scavenging needs to take place through secondary carbonate precipitation to explain the data of springs G1, G2, and S10; and that the data of other springs cannot be explained by this scenario if the composition of the carbonate end member is dolomitic). To obtain these results, all spring Cl^- was assumed to be associated to Na^+ (main text section 5.1.1), and K_d^{Sr} was assumed to be equal to K_d^{Mg} with a value of 0.06 was used. Modification of these assumptions would not change the general principles that are exemplified by this figure; and uncertainty on these aspects is taken into account in our Monte Carlo simulations.

To assess the validity of our findings from the mixing model using independent measurements, our $\delta^{34}S$ measurements can be used. A significant linear negative relationship ($R^2 = 0.8$) exists between the $\delta^{34}S$ measured in springs across the Séchilienne massif and the modal estimates of their X_{sil}^{SO4}, consistent with the isotope composition of sulfur being driven by a binary mixture (Fig. D5). The intercept of this relationship ($X_{sil}^{SO4} = 0$, equivalent to $X_{gyp}^{SO4} = 1$) yields an estimate for $\delta^{34}S_{gyp} = 8.4‰$, while extrapolation to $X_{sil}^{SO4} = 1$ indicates $\delta^{34}S_{sulfur} = -3.1‰$. Such estimates are fully consistent with our own measurements of solid sulfur at Séchilienne, as well as with reported measurements for Triassic seawater where local gypsum might have formed.

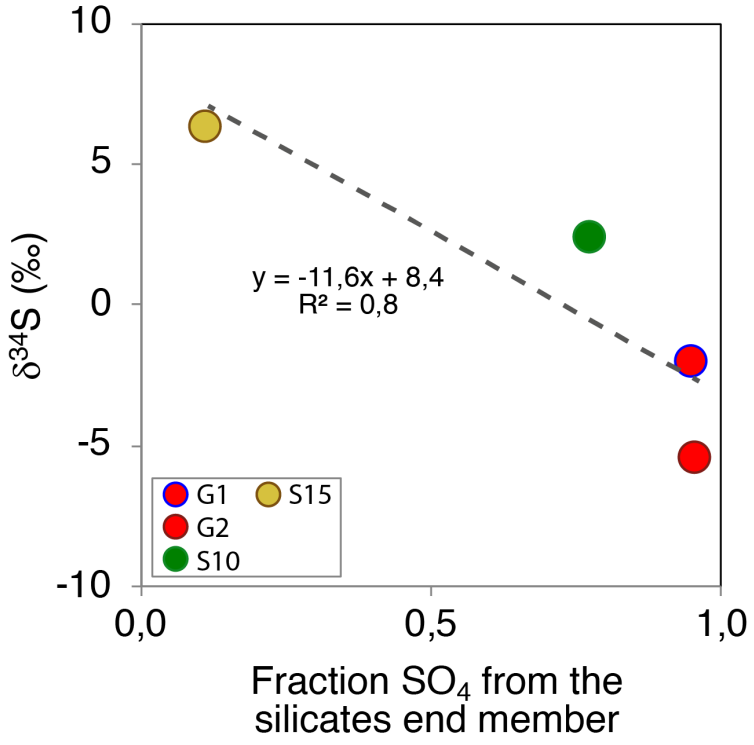

Figure D5: $\delta^{34}S$ measured in springs across the Séchilienne massif vs modal estimates of their fraction of SO_4 from silicate endmember: X_{sil}^{SO4}.

CO_2 consumption budget

The mixing analysis presented above shows that at Séchilienne solutes are released to springs through the partial dissolution of silicate minerals, carbonate minerals, and gypsum, while dissolved Ca is scavenged by secondary carbonate precipitation. Fundamentally, these weathering reactions modify the carbon content in the atmosphere-hydrosphere continuum, which impacts the CO_2 concentration in the atmosphere. An approach to evaluate this impact has been recently proposed by Torres et al. (2016), based on the relative change in alkalinity (Alk) and Dissolved Inorganic Carbon (DIC) in ambient waters resulting from the combination of weathering reactions. Torres et al. (2016) contend that the relevant Alk/DIC ratio against which the shifts in Alk and DIC ensuing weathering reactions have to be evaluated is that of the ocean. However, in the case of Séchilienne, and in particular because secondary carbonate precipitation is a significant process there, this approach cannot be used. Indeed, secondary carbonate precipitation removes Alk and DIC from ambient waters following the reaction:

$$Ca^{2+} + 2HCO_3^- \rightarrow CaCO_3 + H_2CO_3 \qquad \text{(D9)}$$

And the ensuing change in Alk and DIC occurs at the loci of secondary carbonate precipitation (i.e. at Séchilienne, in the subsurface of the instability), the Alk/DIC of which is not known. However, we still believe that it is essential to assess the long-term (that is, once weathering-derived solutes are delivered to the oceans) effects of these weathering reactions on atmospheric CO_2, especially in contexts where sulfide oxidation is a significant process, such as at Séchilienne.

As a consequence, we assess the CO_2 impact of the various weathering reactions at Séchilienne in the following way:

- For silicate weathering by carbonic acid (eq. 9 of main text), each meq of cation released leads to the consumption of 1 mole of CO_2 "on site", meaning immediately when the reaction takes place; and we assume that all meq of cation released are precipitated in the ocean on the "long term" through equation (D9), leading in total to the net consumption of 0.5 mole of CO_2 per meq initially released;
- Silicate weathering by sulfuric acid (eq. 10), has no "on site" net effect on atmospheric CO_2; and we assume that it has no net effect on the "long term" either once solutes are delivered to the ocean, based on the fact that this reaction does not produce any alkalinity that is required for carbonate precipitation to occur (eq. D9);
- Carbonate weathering by carbonic acid (eq. 11 of main text) consumes 0.5 mol of CO_2 per meq of cation (Ca^{2+} or Mg^{2+}) released "on site", but this effect is negated on the "long term" by carbonate precipitation in the ocean (eq. D9; note that here "long term" refers to a time scale longer than the characteristic time scale for carbonate precipitation in the ocean (around 10^5 yrs), but shorter that the characteristic time scale for sulfate reduction in the ocean (around 10^7 yrs; Torres et al., 2016));
- Carbonate weathering by sulfuric acid (eq. 12 of main text) has no "on site" net effect on atmospheric CO_2; but is likely to lead on the long term to the release of 0.25 mol of CO_2 (eq. D9) for each meq of cation (Ca^{2+} or Mg^{2+}) released initially.

- Secondary carbonate formation happens only "on site" by definition, and leads to the release of 0.5 mol of CO_2 for each meq of cation (Ca^{2+}) precipitated (eq. D9).

Given that we do not have access to water discharge at Séchilienne, this analysis cannot be performed on a flux basis. Therefore, we use a concentration-based analysis, where the CO_2 effect of each process is compared within each spring in a consistent manner and expressed as the consumption or release of CO_2 in mol per liter of water (Fig. 7).

We performed this analysis on all springs but spring S12, for which the significant influence of anthropogenic activities precludes quantitative apportionment by the methods outlined above. In addition, in the cases of springs S20 and S21 none of the 10,000 Monte Carlo runs were able to yield X_i^E values in the interval [0,1] for all i and E. This is probably because their hydrochemistry can be readily explained by a simple binary mixture between gypsum and carbonate-derived solutes, such that any small variation in the composition of these end members result in negative X_{sil}^E values for one or more instances of the element E. However, because the hydrochemistry of springs S20 and S21 is similar to those of S13 and S15, we expect that their role on atmospheric CO_2 is similar to that played by springs S13 and S15 (Fig. 7).

Table D1: Inputs of the mixing model with silicate, carbonate and gypsum endmembers

Outflow	Spring average composition									Silicate end member			
	$^{87}Sr/^{86}Sr$	SO4/Sr	Mg/Sr	Ca/Sr	Na/Sr	Na/Sr corrected	Sr/Ca	Mg/Ca	Na/Ca	$^{87}Sr/^{86}Sr$		Na/Sr	
										Mean	s.d.	Mean	s.d.
G1	0,72155	571	418	445	43	32	0,0024	0,93	0,077	0,735	0,005	81	9
G2	0,72058	786	397	411	90	62	0,0025	0,95	0,171	0,735	0,005	192	28
S10	0,71489	196	400	438	46	36	0,0023	0,90	0,082	0,735	0,005	187	28
S15	0,70964	69	64	150	10	1	0,0066	0,42	0,019	0,735	0,005	153	40
S18	0,70960	135	126	398	17	12	0,0025	0,31	0,031	0,735	0,005	153	36

Outflow	Carbonate end member						Gypsum end member							
	$^{87}Sr/^{86}Sr$		Sr/Ca		Mg/Ca		$^{87}Sr/^{86}Sr$		Sr/SO4		Mg/SO4		Ca/SO4	
	Low	High	Mean	s.d.	Mean	s.d.	Low	High	Mean	s.d.	Mean	s.d.	Mean	s.d.
G1	0,7091	0,7097	0,00062	0,00002	0,19	0,02	0,7075	0,708	0,0092	0,004	0,31	0,04	0,69	0,04
G2	0,7091	0,7097	0,00062	0,00002	0,19	0,02	0,7075	0,708	0,0092	0,004	0,31	0,04	0,69	0,04
S10	0,7091	0,7097	0,00062	0,00002	0,19	0,02	0,7075	0,708	0,0092	0,004	0,31	0,04	0,69	0,04
S15	0,7091	0,7097	0,00062	0,00002	0,19	0,02	0,7075	0,708	0,0092	0,004	0,31	0,04	0,69	0,04
S18	0,7091	0,7097	0,00062	0,00002	0,19	0,02	0,7075	0,708	0,0092	0,004	0,31	0,04	0,69	0,04

Table D2: Results of mixing calculations

Outflow	Fractions Sr (X^{Sr}_i)									Fractions Mg (X^{Mg}_i)									percentage of valid iterations
	Silicate			Carbonate			Gypsum			Silicate			Carbonate			Gypsum			
	D_{50}	D_{16}	D_{84}	D_{50}	D_{16}	D_{84}	D_{50}	D_{16}	D_{84}	D_{50}	D_{16}	D_{84}	D_{50}	D_{16}	D_{84}	D_{50}	D_{16}	D_{84}	
G1	0,47	0,42	0,52	0,28	0,09	0,46	0,25	0,08	0,43	0,75	0,63	0,88	0,22	0,07	0,36	0,02	0,01	0,05	10,2
G2	0,42	0,37	0,47	0,29	0,11	0,48	0,29	0,10	0,47	0,73	0,58	0,86	0,24	0,09	0,40	0,02	0,01	0,05	8,9
S10	0,23	0,20	0,26	0,36	0,13	0,55	0,42	0,23	0,64	0,67	0,53	0,83	0,28	0,10	0,43	0,03	0,02	0,07	20,9
S15	0,06	0,05	0,07	0,04	0,02	0,07	0,90	0,87	0,92	0,43	0,15	0,56	0,19	0,08	0,33	0,41	0,28	0,55	0,4
S18	0,08	0,06	0,09	0,07	0,02	0,13	0,85	0,79	0,90	0,56	0,37	0,73	0,19	0,05	0,34	0,22	0,15	0,38	6,2

Outflow	Fractions Ca (X^{Ca}_i)									Fractions SO_4 (X^{SO4}_i)						Fraction of Ca left in solution after secondary carbonate precipitation (γ)			percentage of valid iterations
	Silicate			Carbonate			Gypsum			Silicate (sulfur)			Gypsum						
	D_{50}	D_{16}	D_{84}	D_{50}	D_{16}	D_{84}	D_{50}	D_{16}	D_{84}	D_{50}	D_{16}	D_{84}	D_{50}	D_{16}	D_{84}	D_{50}	D_{16}	D_{84}	
G1	0,55	0,28	0,82	0,42	0,13	0,71	0,02	0,01	0,04	0,95	0,9	0,99	0,05	0,01	0,1	0,38	0,37	0,39	10,2
G2	0,48	0,17	0,78	0,48	0,18	0,81	0,02	0,01	0,05	0,96	0,92	0,99	0,04	0,01	0,08	0,39	0,38	0,40	8,9
S10	0,40	0,12	0,74	0,56	0,20	0,85	0,03	0,01	0,06	0,78	0,59	0,88	0,22	0,12	0,41	0,40	0,39	0,41	20,9
S15	0,19	0,05	0,42	0,37	0,15	0,66	0,35	0,24	0,50	0,12	0,03	0,2	0,88	0,8	0,97	0,90	0,89	0,90	0,4
S18	0,40	0,12	0,67	0,37	0,10	0,67	0,18	0,13	0,29	0,43	0,21	0,57	0,57	0,43	0,79	1,00	1,00	1,00	6,2

Outflow	Fractions total cationic charge ($X^{\Sigma r}_i$)									percentage of valid iterations
	Silicate			Carbonate			Gypsum			
	D_{50}	D_{16}	D_{84}	D_{50}	D_{16}	D_{84}	D_{50}	D_{16}	D_{84}	
G1	0,61	0,38	0,84	0,37	0,11	0,61	0,02	0,01	0,04	10,2
G2	0,56	0,31	0,81	0,40	0,15	0,68	0,02	0,01	0,05	8,9
S10	0,48	0,24	0,76	0,48	0,17	0,73	0,03	0,02	0,07	20,9
S15	0,29	0,10	0,45	0,33	0,13	0,56	0,36	0,29	0,48	0,4
S18	0,45	0,21	0,68	0,32	0,09	0,58	0,20	0,15	0,30	6,2

footnotes:

- ***All elemental ratios in mol/mol***
- ***When only one value is provided (spring composition), the value of the parameter was not varied between different Monte Carlo runs. When two values are provided, in the case of a variable whose value is assumed to follow a uniform distribution "low" and "high" provide the lower and upper bounds of the interval over which the parameter was drawn randomly following a uniform distribution; and in the case of a variable that is assumed to follow a normal distribution "Mean" and "s.d." provide the mean and the standard deviation of the normal distribution from which the parameter was drawn.***
- ***The spring elemental ratios reported here have been corrected from rain inputs***
- ***"corrected" for spring Na/Sr ratios refers to values once an amount of Na equal to the amount of non-atmospheric Cl has been removed. The actual Na/Sr ratio used in each Monte Carlo run was randomly drawn between "Na/Sr" and "Na/Sr corrected"***

Table D3: Evaluation of the effect of weathering processes at Séchilienne on atmospheric CO_2 and $\delta^{34}S$ estimates of the pyrite endmember

Outflow	"On-site" CO_2 consumption (mmol L-1)			"Long-term" CO_2 consumption (mmol L-1)			percentage of valid iterations	$\delta^{34}S$		
	D_{50}	D_{16}	D_{84}	D_{50}	D_{16}	D_{84}		Sample	Gypsum	Silicate *(sulfur)*
G1	-1,76	-2,89	-0,76	2,43	0,85	4,02	10,2	-2,12	8,4	-3,1
G2	0,69	0,45	0,89	1,61	1,09	2,13	8,9	-5,45	8,4	-3,1
S10	-3,22	-4,40	-2,33	0,33	-0,90	1,33	20,9	2,38	8,4	-3,1
S15	-1,95	-2,34	-1,56	-0,49	-0,91	-0,03	0,4	6,40	8,4	-3,1
S18	-2,73	-3,27	-2,30	-1,22	-1,70	-0,75	6,2			

Team list

Pierre Nevers

Julien Bouchez

Jérome Gaillardet

Thomazo Christophe

Charpentier Delphine

Laëticia Faure

Catherine Bertrand

Author contribution

Pierre Nevers measured the Sr isotopic ratios, worked on the interpretation and wrote text. Julien Bouchez and Jérôme Gaillardet helped with the isotopic measurements, in the inversion calculations and in writing text. Christophe Thomazo measured the sulfur isotopic ratios. Delphine Charpentier worked on XRD and mineralogic analyses presented in supplementary materials. Laëticia Faure helped with the rock sample leaching procedure and Sr isotope measurements. Catherine Bertrand organized the sampling strategy and is in charge of the Séchilienne Observatory (SNO OMIV) and helped in writing text.

Competing interests

The authors declare that they have no conflict of interest.

Acknowledgments

Part of this work was supported by IPGP multidisciplinary program PARI and by Region île-de-France SESAME Grant no. 12015908. Caroline Gorge, Christophe Loup and Caroline Amiot are acknowledged for analytical support, and Vanessa Stefani is acknowledged for support on the field. The authors warmly thank: the PEA²t platform (Chrono environment, University of Bourgogne Franche-Comté, UMR CNRS 6249, France), which manages and maintains the analytical equipment used in this study; and OMIV and OSU Theta for supporting the project through financial contributions (SRO_2015).

References

Barféty, J., Bordet, P., Carme, F., Debelmas, J., Meloux, M., Montjuvent, G., Sarrot Reynauld, J.: Carte géologique détaillée de la France (1/50000) n°797 Vizille. Editions du BRGM, p. 38, 1972

Barla, G. et Chiriotti, E., 1995. Insights into the behaviours of the large deep seat gravitational slope deformation of Rosone, in the Piemont region (Italy). Felsbau, 13: 425-432

Baudement, C., Bertrand, C., Guglielmi, Y., Viseur, S., Vallet, A., & Cappa, F.: Quantification de la dégradation mécanique et chimique d'un versant instable : approche géologique, hydromécanique et hydrochimique Etude du versant instable de Séchilienne, Isère (38). 1–6, 2013

Behrens R., Bouchez J., Schuessler J. A., Dultz S., Hewawasam T. and von Blanckenburg F. (2015) Mineralogical transformations set slow weathering rates in low-porosity metamorphic bedrock on mountain slopes in a tropical climate. Chem. Geol. 411, 283–298, https://doi.org/ 10.1016/j.chemgeo.2015.07.008, 2015

Berner,K.E. and Berner,R.A.: Global Environment: Water, Air and Geochemical Cycles,Princeton Univ. Press, 369–382, 2012

Bertrand, C., Vallet, A., Mudry, J.,: Hydrochemical Approach of Mechanical Degradation of the Séchilienne Unstable Slope, in Engineering Geology for Society and Territory – Volume 2, edited by: Lollino, G., Giordan, Crosta, G. B., Corominas, J.,

Azzam, R., Wasowski, J., Sciarra, N., Springer International Publishing Switzerland, chapter: 383, https://doi.org/10.1007/978-3-319-09057-3_383, 2015

Bickle, M. J., Tipper, E. T., Galy, A., Chapman, H., and Harris, N.: On Discrimination Between Carbonate and Silicate Inputs to Himalayan Rivers, Am. J. Sci., 315, 120–166, https://doi.org/10.2475/02.2015.02, 2015

Binet, S., Spadini, L., Bertrand, C., Guglielmi, Y., Mudry, J., and Scavia, C.: Variability of the groundwater sulfate concentration in fractured rock slopes: a tool to identify active unstable areas, Hydrol. Earth Syst. Sci., 13, 2315–2327, https://doi.org/10.5194/hess-13-2315-2009, 2009

Blattmann T. M., Wang, S. L., Lupker, M., Märki, L., Haghipour, N., Wacker, L., Chung, L. H., Bernasconi, S. M, Plötze, M., Eglinton, T. I.: Sulphuric acid-mediated weathering on Taiwan buffers geological atmospheric carbon sinks, Sci Rep, 2945, https://doi.org/10.1038/s41598-019-39272-5, 2019

Brass, G. W.: The effect of weathering on the distribution of strontium isotopes in weathering profiles. Geochimica et Cosmochimica Acta, 39, 1647–1653, https://doi.org/10.1016/0016-7037(75)90086-1, 1975

Bullen, T. D., Krabbenhoft, D. P., Kendall, C.: Kinetic and mineralogic controls on the evolution of groundwater chemistry and 87Sr/86Sr in a sandy silicate aquifer, northern Wisconsin, USA. Geochimica et Cosmochimica Acta, 60(10), 1807–1821, https://doi.org/10.1016/0016-7037(96)00052-X, 1996

Bullen, T. D. and Kendall, C.: Tracing of Weathering Reactions and Water Flowpaths: A Multi-isotope Approach, in: Isotope Tracers in Catchment Hydrology, edited by Kendall, C., McDonnell, J. J, Elsevier Science B.V., Amsterdam, pp. 611-646, https://doi.org/10.1016/B978-0-444-81546-0.50025-2, 1998

Burke, W.H., Denison, R.E., Hetherington, E.A., Koepnick, R.B., Nelson, H.F. and Otto, J.B.: Variation of seawater 87Sr/86Sr throughout Phanerozoic time. Geology 10: 516-519., https://doi.org/10.1130/0091-7613(1982)10<516:VOSSTP>2.0.CO;2, 1982

Calmels, D., Gaillardet, J., Brenot, A., & France-Lanord, C.: Sustained sulfide oxidation by physical erosion processes in the Mackenzie River basin: Climatic perspectives, Geology, 35(11), 1003–1006, https://doi.org/10.1130/G24132A.1, 2007

Canfield, D. E., Raiswell, R., Westrich, J. T., Reaves, C. M., Berner, R. A.: the use of chromium reduction in the analysis of reduced inorganic sulfur in sediments and shales, Chemical Geology, 54(1-2), 149–155, https://doi.org/10.1016/0009-2541(86)90078-1, 1986

Cappa, F., Guglielmi, Y., Soukatchoff, V., Mudry, J., Bertrand, C., Charmoille, A.: Hydromechanical modeling of a large moving rock slope inferred from slope levelling coupled to spring long-term hydrochemical monitoring: example of the La Clapière landslide (Southern Alps, France), Journal of Hydrology, 291(1–2), 67–90, https://doi.org/10.1016/J.JHYDROL.2003.12.013, 2004

Cervi, F., Ronchetti, F., Martinelli, G., Bogaard, T. A., and Corsini, A.: Origin and assessment of deep groundwater inflow in the Ca' Lita landslide using hydrochemistry and in situ monitoring, Hydrol. Earth Syst. Sci., 16, 4205–4221, https://doi.org/10.5194/hess-16-4205-2012, 2012

Clow, D. W and Drever, J. I.: Weathering rates as a function of flow through an alpine soil, Chemical Geology, 132(1–4), 131–141, https://doi.org/10.1016/S0009-2541(96)00048-4, 1996

Cortecci, G., Dinelli, E., Bencini, A., Adorni-Braccesi, A., La Ruffa, G.: Natural and anthropogenic SO4 sources in the Arno river catchment, northern Tuscany, Italy: a chemical and isotopic reconnaissance, Applied Geochemistry, 17(2), 79–92, https://doi.org/10.1016/S0883-2927(01)00100-7, 2002

Deiana, M., Cervi, F., Pennisi, M., Mussi, M., Bertrand, C., Tazioli, A., Ronchetti, F.: Chemical and isotopic investigations (δ18O, δ2H, 3H, 87Sr/86Sr) to define groundwater processes occurring in a deep-seated landslide in flysch. Hydrogeology Journal, 26(8), 2669–2691, https://doi.org/10.1007/s10040-018-1807-1, 2018

Dotsika, E., Poutoukis, D., Kloppmann, W., Guerrot, C., Voutsa, D., Kouimtzis, T. H.: The use of O, H, B, Sr and S isotopes for tracing the origin of dissolved boron in groundwater in Central Macedonia, Greece. Applied Geochemistry, 25(11), 1783–1796. https://doi.org/10.1016/J.APGEOCHEM.2010.09.006, 2010

Dubois, L., Chanut, M.-A., Duranthon, J. P.: Amélioration continue des dispositifs d'auscultation et de surveillance integrés dans le suivi du versant instable des Ruines de Séchilienne in : Géologues, 182, edited by : Editions du BRGM, 50–55, 2014

Emberson, R., Hovius, N., Galy, A. Marc, O.: Chemical weathering in active mountain belts controlled by stochastic bedrock landsliding, Nature Geoscience, 9, 42–45, https://doi.org/10.1038/ngeo2600, 2015

Emberson, R., Hovius, N., Galy, A., Marc, O.: Oxidation of sulfides and rapid weathering in recent landslides, Earth Surface Dynamics, 4(3), 727–742, https://doi.org/10.5194/esurf-4-727-2016, 2016b

Emberson, R., Galy, A., Hovius, N.: Weathering of Reactive Mineral Phases in Landslides Acts as a Source of Carbon Dioxide in Mountain Belts, Journal of Geophysical Research: Earth Surface, 123(10), 2695–2713. https://doi.org/10.1029/2018JF004672, 2018

Fanlo, I. and Ayora, C.: The evolution of the Lorraine evaporitic basin: implications for the chemical and isotope composition of the Triassic ocean, Chemical Geology, vol. 146 n° 3-4, p. 135–154, https://doi.org/10.1016/S0009-25419800007-2, 1998

Fletcher, R. C., Buss, H. L., and Brantley, S. L.: A spheroidal weathering model coupling porewater chemistry to soil thicknesses during steady-state denudation, Earth Planet. Sci Lett., 244, 444-457, https://doi.org/10.1016/j.epsl.2006.01.055, 2006

Follacci, J.: Seize ans de surveillance du glissement de la Clapière (Alpes maritimes). 220, Rapport, Bulletin du Laboratoire des Ponts et Chaussés. 35-51, 1999

Frost, C. D., Toner, R. N.: Strontium isotopic identification of water-rock interaction and ground water mixing, Ground Water, 42(3), 418–432, https://doi.org/10.1111/j.1745-6584.2004.tb02689.x, 2004

Gaillardet, J., Dupre, B., Allegre C. J., Négrel, P.: Chemical and physical denudation in the Amazon River Basin, Chemical Geology, vol. 142 n° 3–4, p. 141-173, https://doi.org/10.1016/S0009-2541(97)00074-0, 1997

Gaillardet, J., Dupre, B., Louvat, P., Allegre, C. J.: Global silicate weathering and CO2 consumption rates deduced from the chemistry of large rivers, Chemical Geology, 159, 3–30, https://doi.org/10.1016/S0009-2541(99)00031-5, 1999

Gammons, C. H., Brown, A., Poulson, S. R., Henderson, T. H.: Using stable isotopes (S, O) of sulfate to track local contamination of the Madison karst aquifer, Montana, from abandoned coal mine drainage, Applied Geochemistry, 31, 228–238, https://doi.org/10.1016/J.APGEOCHEM.2013.01.008, 2013

Guglielmi, Y., Vengeon, J., Bertrand, C., Mudry, J., Follacci, J., Giraud, A.: Hydrogeochemistry: an investigation tool to evaluate infiltration into large moving rock masses (case study of La Clapière and Séchilienne alpine landslides), Bulletin of Engineering Geology and the Environment, 61(4), 311–324. https://doi.org/10.1007/s10064-001-0144-z, 2002

Hajj, F., Poszwa, A., Bouchez, J., Guérold, F.: Radiogenic and “stable” strontium isotopes in provenance studies: A review and first results on archaeological wood from shipwrecks, Journal of Archaeological Science, 86, 24–49, https://doi.org/10.1016/j.jas.2017.09.005, 2017

Kampschulte, A., Strauss, H.: The sulfur isotopic evolution of Phanerozoic seawater based on the analysis of structurally substituted sulfate in carbonates, Chemical Geology, 204(3–4), 255–286, https://doi.org/10.1016/j.chemgeo.2003.11.013, 2004

Koepnick, R. B., Denison, R. E., Burke, W. H., Hetherington, E. A., Dahl, D. A.: Construction of the Triassic and Jurassic portion of the Phanerozoic curve of seawater 87Sr/86Sr, Chemical Geology: Isotope Geoscience Section, 80(4), 327–349, https://doi.org/10.1016/0168-9622(90)90014-4, 1990

Lajaunie, M., Gance, J., Nevers, P., Malet, J.-P., Bertrand, C., Garin, T., and Ferhat, G.: Structure of the Séchilienne unstable slope from large-scale 3d electrical tomography using a resistivity distributed automated system (r-das). Geophysical Journal International, https://doi.org/10.1093/gji/ggz259, 2019

Lasaga, A. C.: Chemical kinetics of water-rock interactions, Journal of Geophysical Research: Solid Earth, 89(B6), 4009–4025, https://doi.org/10.1029/jb089ib06p04009, 1984

Lerman, A., Wu, L., Mackenzie, F. T.: CO2 and H2SO4 consumption in weathering and material transport to the ocean, and their role in the global carbon balance, Marine Chemistry, 106(1-2 SPEC. ISS.), 326–350, https://doi.org/10.1016/j.marchem.2006.04.004, 2007

Le Roux, O., Jongmans, D., Kasperski, J., Schwartz, S., Potherat, P., Lebrouc, V., Meric, O.: Deep geophysical investigation of the large Séchilienne landslide (Western Alps, France) and calibration with geological data, Engineering Geology, 120(1–4), 18–3, https://doi.org/10.1016/J.ENGGEO.2011.03.004, 2011

Li, S. L., Calmels, D., Hana, G., Gaillardet, J., Liu, C. Q.: Sulfuric acid as an agent of carbonate weathering constrained by δ13CDIC: Examples from Southwest China, Earth and Planetary Science Letters, 270, 3–4, 30, 189-199, https://doi.org/10.1016/j.epsl.2008.02.039, 2008

Maréchal, J.-C., 1998. Les circulations d'eau dans les massifs cristallins alpins et leurs relations avec les ouvrages souterrains, Ecole Polytechnique Fédérale de Lausanne (EPFL), 1998

Meric, O., Garambois, S., Jongmans, D., Wathelet, M., Chatelain, J. L., Vengeon, J. M.: Application of geophysical methods for the investigation of the large gravitational mass movement of Séchilienne, France, Canadian Geotechnical Journal, 42(4), 1105–1115, https://doi.org/10.1139/t05-034, 2005

Meybeck Michel. Composition chimique des ruisseaux non pollués en France. Chemical composition of headwater streams in France. In: Sciences Géologiques, tome 39, n°1, pp. 3-77, https://doi.org/10.3406/sgeol.1986.1719, 1986

Meynadier, L., Gorge, C., Birck, J., Allègre, C.: Automated separation of Sr from natural water samples or carbonate rocks by high performance ion chromatography, Chemical Geology, 227(1–2), https://doi.org/10.1016/j.chemgeo.2005.05.012, 2006

Moncaster, S. J., Bottrell, S. H., Tellam, J. H., Lloyd, J. W., Konhauser, K. O.: Migration and attenuation of agrochemical pollutants: Insights from isotopic analysis of groundwater sulphate, Journal of Contaminant Hydrology, 43(2), 147–163, https://doi.org/10.1016/S0169-7722(99)00104-7, 2000

Montety, V. de, Marc, V., Emblanch, C., Malet, J.-P., Bertrand, C., Maquaire, O., Bogaard, T. A.: Identifying the origin of groundwater and flow processes in complex landslides affecting black marls: insights from a hydrochemical survey, Earth Surface Processes and Landforms, 32(1), 32–48, https://doi.org/10.1002/esp.1370, 2007

Montjuvent, G. and Winistorfer, J.: Glaciations quaternaires dans les Alpes franco-suisses et leur piedmont, in Géologie Alpine, 56, 251–282, 1980

Mudry, J., & Etievant, K., 2007. Synthese hydrogéologique du versant instable des Ruines de Séchilienne (Unpublished report), UMR Chrono-Environnement, University of Franche-Comté, Besançon, 2007

Négrel, P., Allègre, C. J., Dupré, B., Lewin, E.: Erosion sources determined by inversion of major and trace element ratios and strontium isotopic ratios in river: The Congo Basin case, Earth and Planetary Science Letters, 120(1–2), 59–76, https://doi.org/10.1016/0012-821X(93)90023-3, 1993

Négrel, P. and Deschamps, P.: Natural and anthropogenic budgets of a small watershed in the massif central (France): Chemical and strontium isotopic characterization of water and sediments, Aquatic Geochemistry, 2(1), 1–27, https://doi.org/10.1007/BF00240851, 1996

Négrel, P., Casanova, J., Aranyossy, J.-F.: Strontium isotope systematics used to decipher the origin of groundwaters sampled from granitoids: the Vienne Case (France), Chemical Geology, 177(3–4), 287–308, https://doi.org/10.1016/S0009-2541(00)00414-9, 2001

Oudin, L., Hervieu, F., Michel, C., Perrin, C., Andréassian, V., Anctil, F., and Loumagne, C.: Which potential evapotranspiration input for a lumped rainfall–runoff model?: Part 2—towards a simple and efficient potential evapotranspiration model for rainfall–runoff modelling, Journal of hydrology, 303(1-4):290–306, 2005

Raymo, M. E.: Geochemical evidence supporting T. C. Chamberlin's theory of glaciation, Geology, 19, 344–347, https://doi.org/10.1130/0091-7613(1991)019<0344:GESTCC>2.3.CO;2, 1991

Raymo, M., Ruddiman, W.: Tectonic forcing of late Cenozoic climate, Nature, 359, 117–122, https://doi.org/10.1038/359117a0, 1992

Russell, W. A. and Papanastassiou, D. A.: Calcium isotope fractionation in ion-exchange chromatography, Analytical Chemistry, 50(8), 1151–1154, https://doi.org/10.1021/ac50030a036, 1978

Singleton, M. J., Maher, K., DePaolo, D. J., Conrad, M. E., Evan Dresel, P.: Dissolution rates and vadose zone drainage from strontium isotope measurements of groundwater in the Pasco Basin, WA unconfined aquifer, Journal of Hydrology, 321(1–4), 39–58, https://doi.org/10.1016/J.JHYDROL.2005.07.044, 2006

Spence, J., Telmer, K.: The role of sulfur in chemical weathering and atmospheric CO2 fluxes: evidence from major ions, δ13CDIC, and δ34S SO4 in rivers of the Canadian Cordillera, Geochimica Cosmochemica, 69, 5441–5458, https://doi.org/10.1016/j.gca.2005.07.011,2005

Stallard, R. F. and Edmond, J. M.: Geochemistry of the Amazon: 2. The influence of geology and weathering environment on the dissolved load, Journal of Geophysical Research: Oceans, 88, 9671–9688, https://doi.org/10.1029/jc088ic14p09671, 1983

Torres, M. A., West, A. J., Li, G.: Sulphide oxidation and carbonate dissolution as a source of CO2 over geological timescales, Nature, 507(7492), 346–349, https://doi.org/10.1038/nature13030, 2014

Torres, M. A., West, A. J., Clark, K. E., Paris, G., Bouchez, J., Ponton, C., Adkins, J. F.: The acid and alkalinity budgets of weathering in the Andes–Amazon system: Insights into the erosional control of global biogeochemical cycles. Earth and Planetary Science Letters, 450, 381–391, https://doi.org/10.1016/j.epsl.2016.06.012, 2016

Vallet, A. Mouvements de fluides et processus de déstabilisation des versants alpins : Apport de l'étude de l'instabilité de Séchilienne, Université de Franche-Comté, 2014

Vallet, A., Bertrand, C., Mudry, J., Bogaard, T., Fabbri, O., Baudement, C., Régent, B.: Contribution of time-related environmental tracing combined with tracer tests for characterization of a groundwater conceptual model: a case study at the Séchilienne landslide, western Alps (France), Hydrogeology Journal, 23(8), 1761–1779, https://doi.org/10.1007/s10040-015-1298-2, 2015a

Vallet, A., Charlier, J. B., Fabbri, O., Bertrand, C., Carry, N., Mudry, J.: Functioning and precipitation-displacement modelling of rainfall-induced deep-seated landslides subject to creep deformation, Landslides, 13, 653–670, https://doi.org/10.1007/s10346-015-0592-3, 2015b

Vengeon, J. M.: Déformation et rupture des versants en terrain métamorphique anisotrope : Apport de l' étude des Ruines de Séchilienne, Université Joseph-Fourier - Grenoble I, 1998

Vengeon, J.-M., Couturier, B., Antoine, P.: Déformations gravitaires post glaciaires en terrains métamorphiques. Comparaison des indices de déformation du versant sud de la Toura (Saint-Christophe-en-Oisans, France) avec le phénomène de rupture interne du versant sud du Mont Sec (Séchilienne, France), Bulletin of Engineering Geology and the Environment, 57(4), 387–395, https://doi.org/10.1007/s100640050062, 1999

Woods, T. L., Fullagar, P. D., Spruill, R. K., Sutton, L. C.: Strontium isotopes and major elements as tracers of ground water evolution: example from the Upper Castle Hayne Aquifer of North Carolina, Ground Water, 38(5), 762–771, https://doi.org/10.1111/j.1745-6584.2000.tb02712.x, 2000

Zeebe, R. E. and Wolf-Gladrow, D. A.: CO2 in Seawater: Equilibrium, Kinetics, Isotopes, edited by Elsevier Oceanography Series, Amsterdam, 65, 2001.